# Numerička karakterizacija brodskog propelera

**Šeb, Borna**

**Master's thesis / Diplomski rad**

**2017**

*Degree Grantor / Ustanova koja je dodijelila akademski / stručni stupanj:* **University of Zagreb, Faculty of Mechanical Engineering and Naval Architecture / Sveučilište u Zagrebu, Fakultet strojarstva i brodogradnje**

*Permanent link / Trajna poveznica:* https://urn.nsk.hr/urn:nbn:hr:235:498992

*Rights / Prava:* In copyright/Zaštićeno autorskim pravom.

*Download date / Datum preuzimanja:* **2024-10-20**

UNIVERSITY OF ZAGREB

Faculty of Mechanical Engineering and Naval Architecture

# MASTER'S THESIS

**Borna Šeb**

Zagreb, 2017

# UNIVERSITY OF ZAGREB

## Faculty of Mechanical Engineering and Naval Architecture

# NUMERICAL CHARACTERISATION OF A SHIP PROPELLER

Supervisor:                                                                                  Student:

Prof. dr. sc. Hrvoje Jasak                                                          Borna Šeb

Zagreb, 2017

I herebly declare that this thesis is entirely the result of my own work except where otherwise indicated. I have fully cited all used sources and have only used the ones given in the list of references.

I would like to express my sincere gratitude to Professor Hrvoje Jasak for giving me the opportunity to work under the guidance of such a fascinating and inspiring teacher. His valuable comments and encouragement motivated me to be diligent while working on this thesis.

I am truly thankful to Inno Gatin, who was always willing to help me with constructive suggestions and comments whenever I ran into a trouble spot. His support greatly contributed to the quality of this thesis. Working with and learning from such a professional was an invaluable experiance.

I would like to thank my colleagues and friends for giving me an unforgettable time during the entire study period.

Finally, I am indescribably thankful to my family and my girlfriend for all the support and understanding during the preparation of this thesis.

SVEUČILIŠTE U ZAGREBU
**FAKULTET STROJARSTVA I BRODOGRADNJE**
Središnje povjerenstvo za završne i diplomske ispite
Povjerenstvo za diplomske ispite studija strojarstva za smjerove:
procesno-energetski, konstrukcijski, brodostrojarski i inženjersko modeliranje i računalne simulacije

| Sveučilište u Zagrebu | |
|---|---|
| Fakultet strojarstva i brodogradnje | |
| Datum | Prilog |
| Klasa: | |
| Ur.broj: | |

# DIPLOMSKI ZADATAK

Student: **Borna Šeb**  Mat. br.: 0035182331

Naslov rada na
hrvatskom jeziku:  **Numerička karakterizacija brodskog propelera**

Naslov rada na
engleskom jeziku:  **Numerical Characterisation of a Ship Propeller**

Opis zadatka:

Accurate characterisation of a ship propeller performance is essential in free sailing simulations in naval hydrodynamics using Computational Fluid Dynamics (CFD). A prediction of propeller performance using CFD requires a detailed computational mesh of the propeller and accurate modelling of propeller rotation using e.g. multiple rotating frames of reference. The use of such models in long transient runs for a manoeuvring ship or self-propulsed sea-keeping for a ship hull makes the simulations impractical due to a significantly increased computational cost related to the detailed propeller mesh. Instead, it is proposed to use a simplified actuator disk propeller model, tuned to match the results of a detailed propeller simulation.

In this study, evaluation of propeller performance shall be done in isolation via a numerical "open water" test; this will be followed by development of an appropriate actuator disk model tuned to produce an equivalent propeller flow to be used in free sailing simulations.

The candidate shall perform the following tasks within this project:

- describe a CFD model for an open water propeller capable of predicting the K-Q and K-T curves (thrust and torque curves with respect to the advance ratio), indicating achievable accuracy,
- perform simulations of a steady turbulent incompressible flow around the Japan Bulk Carrier (JBC) propeller geometry using Multiple Rotating Frames of Reference (MRF) approach and compare the results against available experimental and reference numerical data. Describe the results in terms of K-T and K-Q diagrams,
- propose an appropriate formulation of the actuator disk model for the JBC propeller, based on the analysis of the radial characteristics of the pressure and vorticity jumps across the propeller plane,
- perform the simulations of the open water propeller test using the proposed actuator disk model and evaluate the performance of the actuator disk against the CFD results for the actual propeller geometry.

The Thesis shall list the bibliography and any assistance received during this study.

Zadatak zadan:  Rok predaje rada:  Predviđeni datumi obrane:

19. siječnja 2017.  23. ožujka 2017.  29., 30. i 31. ožujka 2017.

Zadatak zadao:  Predsjednica Povjerenstva:

Prof. dr. sc. Hrvoje Jasak  Prof. dr. sc. Tanja Jurčević Lulić

# Table of Contents

# Nomenclature

**Greek letters**

| | | |
|---|---|---|
| $\varepsilon$ | Dissipation of turbulence kinetic energy | $m^2 / s^3$ |
| $\eta_0$ | Open water efficiency | - |
| $\gamma$ | Diffusion coefficient | $m^2 / s^2$ |
| $\nu$ | Kinematic viscosity | $m^2 / s^2$ |
| $\nu_t$ | Kinematic eddy viscosity | $m^2 / s^2$ |
| $\omega$ | Eddy turn-over time | $1/s$ |
| $\phi$ | Transported scalar variable | - |
| $\rho$ | Density | $kg/ m^3$ |

**Latin letters**

| | | |
|---|---|---|
| **g** | Gravitational acceleration | $m / s^2$ |
| **u** | Velocity | $m / s$ |
| $Co$ | Courant number | - |
| $J$ | Advance coefficient | - |
| $k$ | Turbulent kinetic energy | $m^2 / s^2$ |
| $K_Q$ | Torque coefficient | - |
| $K_T$ | Thrust coefficient | - |
| $n$ | Rotational speed | $1/s$ |
| $p$ | Kinematic pressure | $m^2 / s^2$ |
| $Q$ | Torque | $N \cdot m$ |
| $T$ | Thrust | $N$ |
| $t$ | Time | $s$ |
| $V_a$ | Speed of advance | $m/s$ |

# List of Figures

# List of Tables

# Abstract

Due to the rapid development of computer technology Computational Fluid Dynamics (CFD) have become a viable tool for hydrodinamic analysis of ship propellers. The open water test for the propeller, traditionally performed to obtain the characteristics used in design, is often simulated with the CFD methods. In this thesis three different CFD methods for simulating the open water test are evaluated based on their accuracy and computational time. They are respectively:

- multiple frames of reference (MRF) for a single blade passage with periodic boundary conditions,

- MRF for complete propeller geometry,

- transient simulation with a rotating mesh and complete propeller geometry.

For some naval applications the interaction between the propeller and ship flows has to be resolved correctly. Solving the flow around the exact propeller geometry in such simulations can be extremely demanding in terms of CPU requirements, which sometimes makes them unfeasible. As an alternative, it is preferred to define an actuator disc region at the location of the propeller at which the momentum transferred from the propeller to the fluid is modelled. In this thesis the open water characteristics from the resolved propeller geometry are used for modelling the propeller influence on the flow with the actuator disc approach. The performance of the actuator disc is afterwards evaluated against the CFD results for the actual propeller geometry.

Keywords: *CFD, OpenFOAM, JBC Propeller, Open water test, MRF, Actuator Disc*

## Sažetak

Napretkom računalne tehnologije računalne metode u dinamici fluida (RDF) postale su dostupne za korištenje u inženjerskoj praksi pa tako i za određivanje hidrodinamičkih značajki brodskog vijka. U ovom radu ispitivane su tri metode simulacije eksperimenta slobodne vožnje brodskog vijka:

- simulacija jedne lopatice brodskog vijka metodom višestrukih referentnih koordinatnih sustava (eng. "Multiple Frames of Reference", skraćeno MRF),

- simulacija cijelog brodskog vijka u MRF pristupu,

- tranzijentna simulacija brodskog vijka.

U svrhu evaluacije pojedine metode, rezultati svake od simulacija su uspoređeni s eksperimentalnim podacima kako bi im se odredila točnost te su međusobno uspoređene obzirom na potrebne računalne resurse. Pokus slobodne vožnje služi kako bi se izračunale radne karakteristike potrebne prilikom projektiranja brodskog vijka. Međutim, izvedba pokusa ne uzima u obzir interakciju između strujanja brodskog vijka i krme broda koja je bitna za određivanje propulzijskih značajki broda. U tu svrhu izvodi se eksperiment vlastitog pogona kod kojeg je model brodskog vijka ugrađen na model krme. RDF simulacija pokusa vlastitog pogona iznimno je skupa jer zahtijeva visoku prostornu i vremensku rezoluciju. Korištenje grublje prostorne i vremenske rezolucije moguće je ako se brodski vijak u takvim simulacijama modelira teorijom idealnog propelera. Takvo pojednostavljenje može u velikoj mjeri smanjiti računalne troškove. U ovom radu provedena je evaluacija modela idealnog vijka koja je izvedena usporedbom rezultirajućeg polja strujanja s poljem strujanja dobivenim iz simulacije oko geometrije brodskog vijka.

## Prošireni sažetak
## (EXTENDED ABSTRACT IN CROATIAN)

## Uvod

Optimizacija brodskog vijka jedan je od najučinkovitijih načina ostvarivanja boljih propulzijskih performansi broda. Tradicionalno su se brodoski vijci projektirali na temelju podataka dobivenih eksperimentalnim putem, provođenjem pokusa otpora modela broda, pokusa slobodne vožnje vijka te pokusa vlastitog pogona. Pokus otpora modela broda provodi se u mirnoj vodi bez priključenog brodskog vijka kako bi se odredio otpor trupa pri određenoj brzini. Test slobodne vožnje vijka također se izvodi u homogenom polju brzine. Rezultati takvih eksperimenata nisu dovoljni za pravilno projektiranje brodskog vijka jer su uvjeti u kojima se izvode idealizirani. U svrhu određivanja propulzijskih značajki broda izvodi se i eksperiment vlastitog pogona. Eksperiment se izvodi sa brodskim vijkom priključenim na trup broda tako da je prilikom takvog testiranja uzeta u obzir interakcija strujanja oko trupa broda i brodskog vijka. Navedena testiranja osim što su dugotrajna, predstavljaju i značajan financijski trošak.

Računalna dinamika fluida (RDF) omogućava simuliranje polja strujanja oko različitih geometrija korištenjem numeričkih metoda prema definiranim algoritmima. Napredak u računalnoj tehnologiji omogućio je širu primjenu RDF metoda u inženjerskoj praksi pa tako i u svrhu projektiranja brodskih vijaka. Numeričkim simulacijama prethodno navedenih eksperimenata moguće je izračunati potrebne radne karakteristike uz relativno niske troškove i u kraćem roku u odnosu na fizički eksperiment. U ovom radu predstavljene su tri metode za simuliranje eksperimenta slobodne vožnje vijka:

- simulacija jedne lopatice brodskog vijka metodom višestrukih referentnih koordinatnih sustava (eng. "Multiple Frames of Reference", skraćeno MRF),

- simulacija cijelog brodskog vijka u MRF pristupu,

- tranzijentna simulacija brodskog vijka.

Radne karakteristike dobivene navedenim metodama uspoređene su s eksperimentalnim podacima kako bi im se odredila točnost. Osim toga, pristupi su međusobno uspoređeni i obzirom na potrebno proračunsko vrijeme. Simulacije u MRF pristupu izvodile su se za svaku točku za koju su poznati eksperimentalni podaci te su na temelju izračunatih radnih karakteristika izrađeni dijagrami slobodne vožnje vijka. Tranzijenta simulacija relativno je zahtjevna po pitanju računalnih resursa pa je stoga izvedena samo za radnu točku u kojoj je iskoristivost vijka najviša. Simulacije su izvedene koristeći CFD software `foam-extend` [2].

Kako bi se iz eksperimenta vlastitog pogona odredile propulzijske značajke broda potrebne su dugotrajne tranzijente simulacije koje su često neisplative. Razlog je velika razlika između vremenskih skala strujanja oko trupa broda i samog brodskog vijka. Iz tog razloga ovakva simulacija zahtijeva visoku prostornu rezoluciju uz vrlo mali vremenski korak. Ukoliko su radne karakteristike brodskog vijka unaprijed poznate, moguće je njegov utjecaj na strujanje modelirati pojednostavljenim modelom propelera te na taj način simulaciju eksperimenta vlastitog pogona učiniti pristupačnijom. U ovom radu model idealnog propelera je primijenjen na potpuno strukturiranoj numeričkoj mreži, a rezultirajuće polje strujanja uspoređeno je s rezultatima strujanja iza brodskog vijka iz prethodno navedene simulacije cijele geometrije u MRF pristupu.

## Matematički model

Nestlačivo, izotermno strujanje opisano je jednadžbom očuvanja mase te Navier-Stokesovim jednadžbama, koje predstavljaju zakon očuavanja količine gibanja:

$$\nabla \cdot \mathbf{u} = 0, \tag{1}$$

$$\frac{\partial \mathbf{u}}{\partial t} + \nabla \cdot (\rho \mathbf{u} \otimes \mathbf{u}) - \nabla \cdot (\nu \nabla \mathbf{u}) = \mathbf{g} - \nabla p, \tag{2}$$

gdje $\mathbf{u}$ predstavlja brzinu, $p$ je tlak, $\rho$ je gustoća fluida, $\nu$ je koeficijent kinematičke viskoznosti, dok je $\mathbf{g}$ gravitacijsko ubrzanje. Jednadžba 2. sastoji se od:

- vremenskog člana $\frac{\partial \mathbf{u}}{\partial t}$,

- konvektivnog člana $\nabla \cdot (\rho \mathbf{u} \otimes \mathbf{u})$,

- difuzijskog člana $\nabla \cdot (\nu \nabla \mathbf{u})$,

- izvorskih članova $-\nabla p$ i $\mathbf{g}$.

Simulacije u MRF pristupu rješavaju se prema jednadžbama izvedenim za rotacijski koordinatni sustav u odnosu prema inercijskom koordinatnom sustavu. MRF je aproksimativna metoda koja rješava stacionarno strujanje oko rotirajućih geometrija. Strujanje u rotacijskom koordinatnom sustavu opisano je pomoću jednadžbi [10]:

$$\nabla \cdot \mathbf{u}_\mathrm{I} = 0, \tag{3}$$

$$\nabla \cdot (\mathbf{u}_\mathrm{R} \otimes \mathbf{u}_\mathrm{I}) + \omega \times \mathbf{u}_\mathrm{I} = -\nabla p + \nu \nabla \cdot \nabla (\mathbf{u}_\mathrm{I}), \tag{4}$$

gdje se veličine indeksirane sa R odnose na rotacijski koordinatni sustav, a one indeksirane sa I na inercijski. Često se simulacije u MRF pristupu rješavaju tako da se numerička domena podijeli više zona od kojih su neke definirane kao rotirajuće, a ostale kao stacionarne. Kako u MRF metodi ne postoji relativno gibanje između domena, rotacija je u uzeta u obzir preko centrifugalnog i Coriolisovog ubrzanja.

Zbog toga što se granice između dviju zona u domeni često ne poklapaju u potpunosti, za provođenje takve simulacije potrebno je definirati te granice na poseban način. Isto se odnosi i na simulacije jedne lopatice u domenama čije su granice periodične. GGI (eng. *Generalized Grid Interface*) sučelje [3] omogućava interpolaciju varijabli strujanja između dvije granice

domene čak i kada se one ne poklapaju u potpunosti. U ovom radu korišten je `cyclicGGi`, inačica GGI sučelja posebno modelirana za rješavanje simulacija u kojima su korištene domene s periodičnim granicama.

## Pokus slobodne vožnje vijka

Pokus slobodne vožnje vijka provodi se u bazenu tako da se lađica na koju je spojen vijak vuče kroz bazen konstantnom brzinom, koja je definirana radnom točkom koja se ispituje. Obzirom da je pokus predviđen za provođenje u jednolikom polju brzine, vijak se vuče u uzvodnom smjeru kako vratilo ili mjerni instrumenti ne bi narušavali strujanje. Na slici 1 nalazi se pojednostavljeni prikaz pokusa slobodne vožnje.
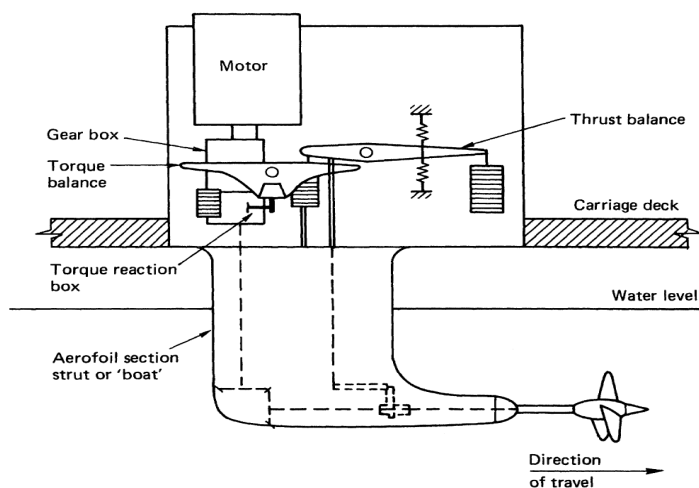


Slika 1: Pokus slobodne vožnje vijka [11].

Pošto vijak tokom cijelog eksperimenta ima konstantnu brzinu rotacije, različita opterećenja se dobivaju na način da se mijenja brzina napredovanja vijka. Za svaku radnu točku definiranu brzinom napredovanja mjere se sila poriva te moment na vijku. Sila poriva i moment mogu se bezdimenzijski izraziti preko radnih karakteristika vijka:

- Koeficijent poriva:

$$K_{\mathrm{T}} = \frac{T}{\rho n^2 D^4}, \tag{5}$$

- Koeficijent momenta:

$$K_{\mathrm{Q}} = \frac{Q}{\rho n^2 D^5}, \tag{6}$$

- Koeficijent napredovanja vijka:

$$J = \frac{V_{\mathrm{a}}}{nD}. \tag{7}$$

Efikasnost se, osim preko odnosa porivne snage vijka i snage elektromotora, može izraziti i preko radnih karakteristika u obliku:

$$\eta_0 = \frac{K_T}{K_Q} \frac{J}{2\pi}. \tag{8}$$

Ako se $K_T$, $K_Q$ i $\eta_0$ za cijelo područje ispitnih stanja izraze u funkciji $J$ dobije se dijagram slobodne vožnje vijka kako je prikazano Slikom 2.
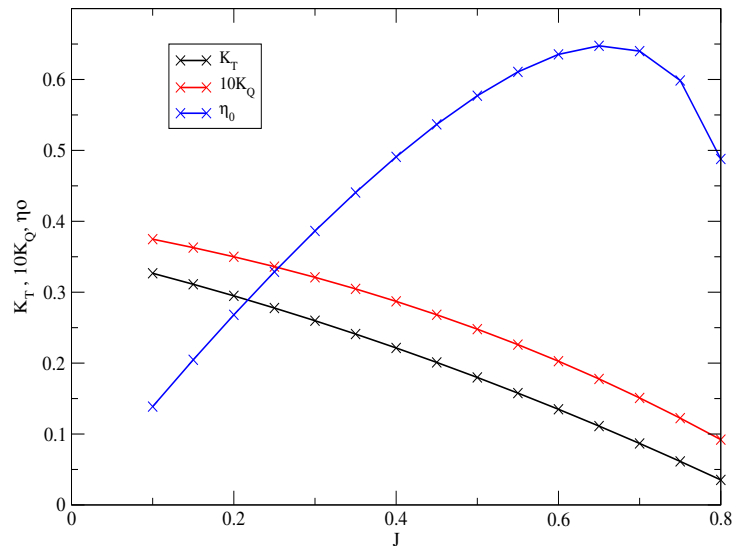


Slika 2: Dijagram slobodne vožnje za model brodskog vijka JBC.

## Rezultati simulacija

Simulacije su provedene na dvije numeričke mreže, generirane softverskim paketom *Pointwise* [12]. Jedna mreža generirana je za simulaciju jedne lopatice, dok je druga napravljena oko kompletne geometrije brodskog vijka. Površinske mreže su u oba slučaja napravljene ručno, a volumenske pomoću *T-Rex* alata za automatsku generaciju hibridne mreže. Hibridna mreža sastoji se od strukturiranog i nestrukturiranog dijela, gdje se strukturirani koristi za prostornu diskretizaciju graničnog sloja oko geometrije, a nestrukturirani za udaljenije dijelove domene. *T-Rex* alat omogućava definiranje različitih ograničenja rješavača, čime se osigurava kontrola nad kvalitetom mreže. Slika 3 prikazuje detalje površinske mreže geometrije brodskog vijka. Generiranje volumenske mreže oko jedne lopatice brodskog vijka pokazalo se zahtjevnije po pitanju zadovoljavanja kriterija kvalitete mreže u odnosu na generiranje mreže oko cijele geometrije. Slike 4 i 5 odnose se na numeričku mrežu oko jedne lopatice brodskog vijka.
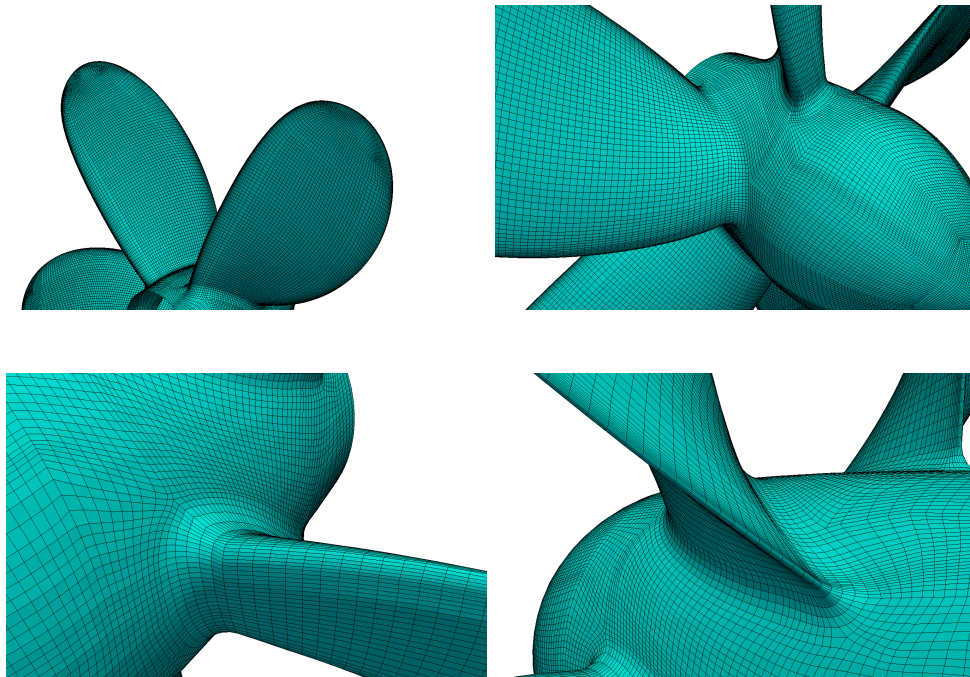
Slika 3: Površinska mreža na geometriji brodskog vijka.
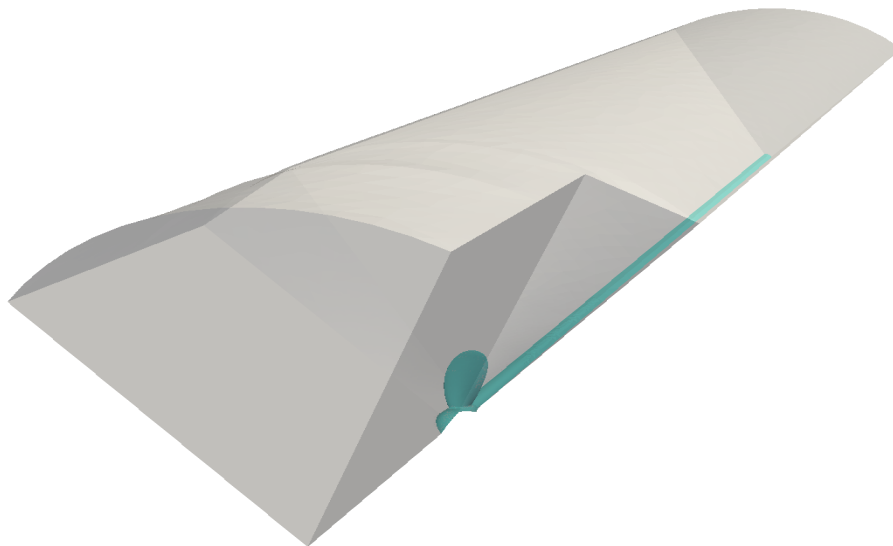


Slika 4: Domena oko jedne lopatice.
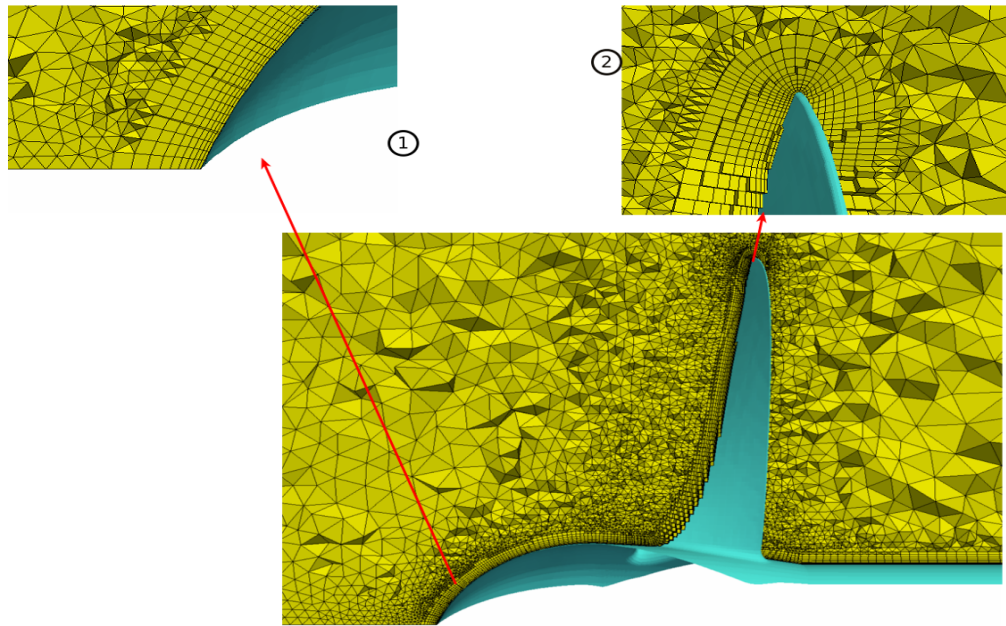
Slika 5: Prijelaz sa strukturirane mreže graničnog sloja na nestrukturiranu mrežu.

Na slici 5 može se vidjeti prijelaz sa strukturiranog na nestrukturirani dio mreže, karakterističan za hibridnu mrežu. Slika 6 prikazuje prostornu domenu oko cijele geometrije brodskog vijka.
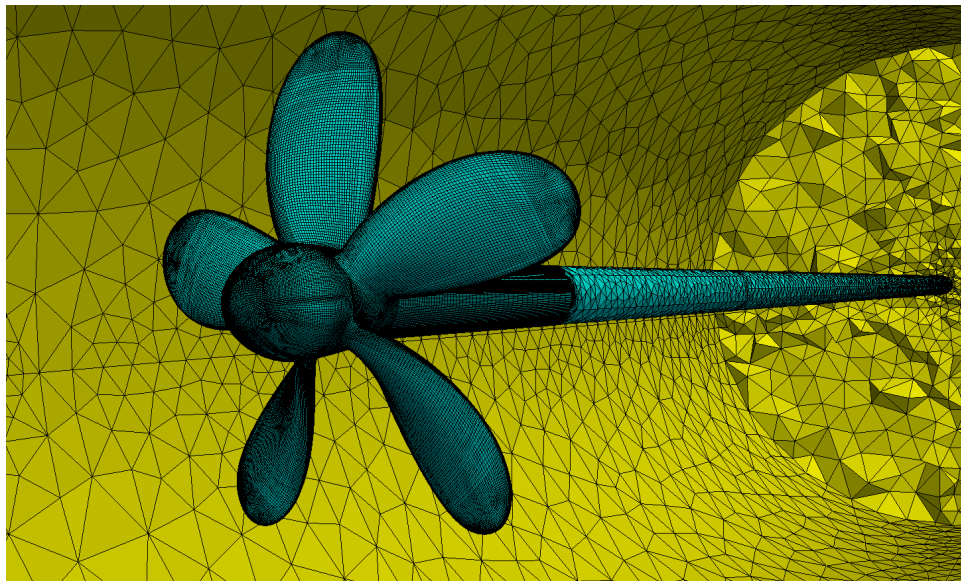


Slika 6: Nestrukturirane vanjske granice domene.

Simulacije u MRF pristupu su izvedene na obje numeričke mreže, dok je tranzijenta simlacija izvedena samo na mreži oko cijelog brodskog vijka. Simulacije izvedene pomoću MRF metode izvodile su se za svaku radnu točku za koju su poznati eksperimentalni podaci te su na temelju rezultata izrađeni dijagrami slobodne vožnje vijka. Tranzijenta simulacija je relativno zahtjevna po pitanju računalnih resursa te je zbog toga izvedena samo za radnu točku u kojoj je iskoristivost najviša ($J = 0.65$). Dijagrami slobodne vožnje vijka dobiveni

simulacijama u MRF pristupu i radne karakteristike dobivene tranzijentom simulacijom dani su Slikom 7a. Slovom C indeksirane su radne karakteristike dobivene simulacijom cijelog brodskog vijka MRF metodom, dok su sa S i T označeni rezultati simulacije jedne lopatice, odnosno tranzijente simulacije. Slika 7b prikazuje relativnu grešku za svaku ispitivanu radnu točku.
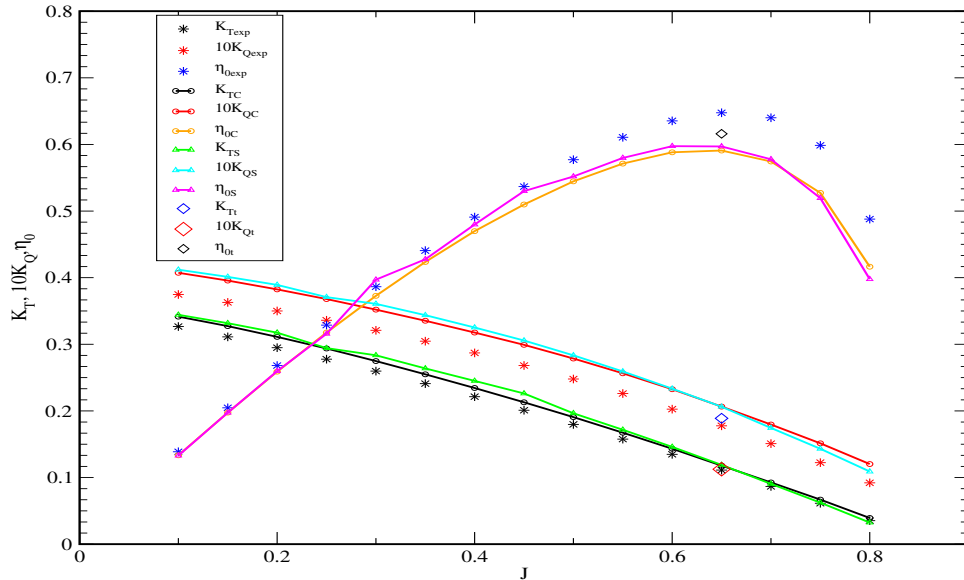


(a) Dijagrami slobodne vožnje brodskog vijka,
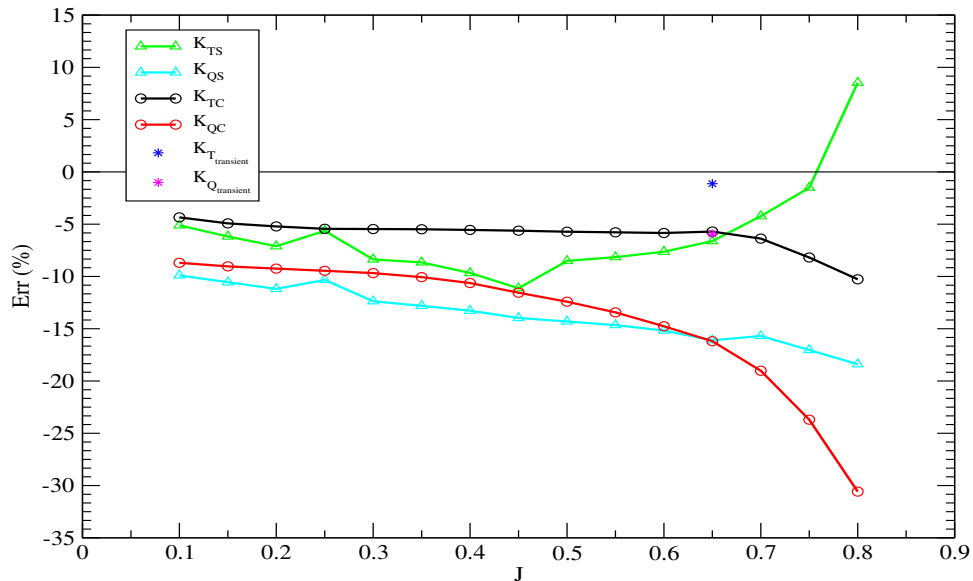


(b) Usporedba relativne greške simulacija,

Slika 7: Usporedba točnosti metoda.

Iako su rezultati zadovoljavajući za svaki pristup jer je greška za većinu ispitivanih radnih stanja konzistentna, vidljivo je da su oni ipak najmanje točni u slučaju simulacije jedne lopatice. To je i očekivano jer osim što je u jednadžbama modela zanemaren vremenski član, u ovom slučaju je i utjecaj ostalih lopatica uzet u obzir interpolacijom varijabli strujanja između periodičnih

granica pomoću GGI sučelja. Tranzijenta simulacija je za radnu točku $J = 0.65$ dala najtočniji rezultat. Tablicom 1 dana je usporedba računalnog vremena pojedinih simulacija. Slovo $t$ je oznaka za vrijeme, dok je s $i$ označen broj iteracija u simulaciji.

Table 1: Usporedba vremena simulacije.

| Approach | CPU | i | t, min | t/i, s |
|---|---|---|---|---|
| **Jedna lopatica primjenom MRF metode** | i5, 3.20GHz, 4 jezgre | 2500 | 201 | 4.82 |
| **Cijela geometrija primjenom MRF metode** | i5, 3.20GHz, 4 jezgre | 2000 | 513 | 15.415 |
| **Tranzijentna simulacija cijele geometrije** | i5, 3.20GHz, 4 jezgre | 3200 | 2498 | 46.85 |

Radne karakteristike dobivene MRF simulacijom cijele geometrije brodskog vijka iskorištene su za simulaciju s modelom idealnog propelera te su u svrhu usporedbe u sljedećem poglavlju dani neki od grafičkih prikaza polja dobiveni tim dvjema simulacijama.

## Modeliranje brodskog vijka

Modeliranje brodskog vijka pojednostavljenim modelom vijka može smanjiti potrebne računalne resurse tranzijentih simulacija kojima je cilj dobro riješiti interakciju između brodskog vijka i krme broda. U prostornoj domeni definirana je površina kružnog oblika, polumjera jednakog polumjeru brodskog vijka ($R_P$). Na njoj su definirani rubni uvijeti kojima su propisane teorijske distribucije skoka tlaka i skoka tangencijalne brzine u svrhu ostvarivanja ubrzanja fluida u aksijalnom smjeru uz vrtložno gibanje. Distribucije su funkcija normaliziranog radijusa, a definirane su prema Goldsteinovom optimumu [19] na sljedeći način:

$$\Delta p = A_x r^* \sqrt{1 - r^*}, \tag{9}$$

$$\Delta u_t = A_\theta \frac{r^* \sqrt{1 - r^*}}{r^*(1 - r^*) + r'_h}, \tag{10}$$

gdje su $\Delta p$ i $\Delta u_t$ skokovi tlaka i tangencijalne brzine, $r^*$ predstavlja normalizirani radijus, $r'_h$ je radijus osovine podijeljen s radijusom propelera, a $A_x$ i $A_\theta$ su konstante izračunate pod pretpostavkom da skok tlaka i tangencijalne brzine ostvaruju silu poriva i moment definiran

radnim karakteristikama $K_T$ i $K_Q$.

Simulacija s modelom idealnog propelera izvedena je na potpuno strukturiranoj numeričkoj mreži, koja je izrađena u višestruko manjoj rezoluciji nego mreža oko geometrije brodskog vijka. Na taj način omogućeno je korištenje većeg vremenskog koraka bez povećanja Courantovog broja. Raspodjele aksijalne i tangencijalne komponente brzine na površini idealnog propelera dane su slikom 8. Može se vidjeti kako su komponente brzine raspoređene shodno izrazima 9. i 10.



(a) Aksijalna,               (b) Tangencijalna, m/s,
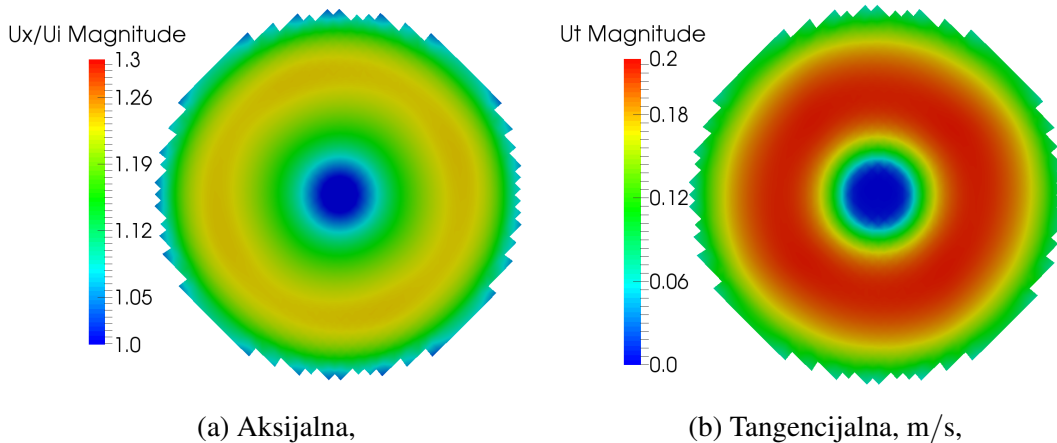
Slika 8: Komponente brzine na površini idealnog propelera.

Sljedećim slikama dana je usporedba polja strujanja dobivenih MRF simulacijom cijele geometrije brodskog vijka i onih dobivenih simulacijom s modelom idealnog propelera. Slika 9 daje usporedbu polja brzine u presjeku y=const., a Slikama 10 i 11 dan je prikaz aksijalnih i tangencijalnih komponenti brzine za obje simulacije na presjeku koji je od površine idealnog propelera, odnosno lopatica brodskog vijka udaljen za x $= 0.2R_P$.
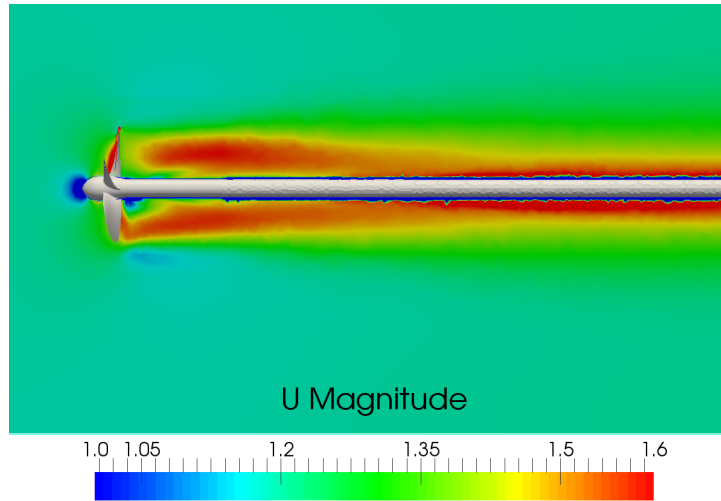
(a) Polje brzine iza brodskog vijka,
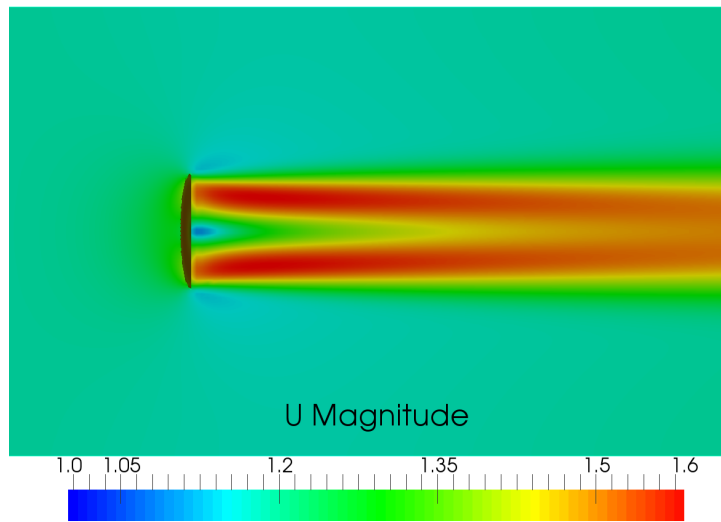


(b) Polje brzine iza modela vijka,

Slika 9: Usporedba polja brzine.
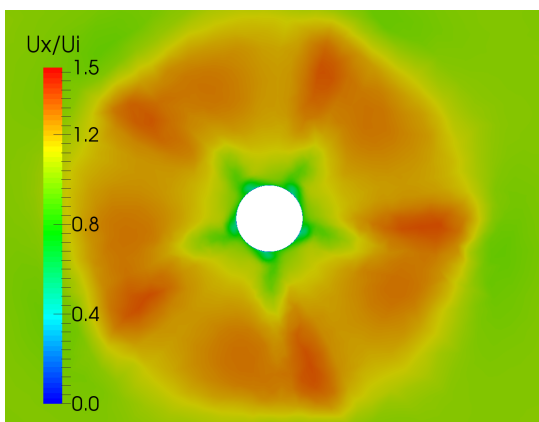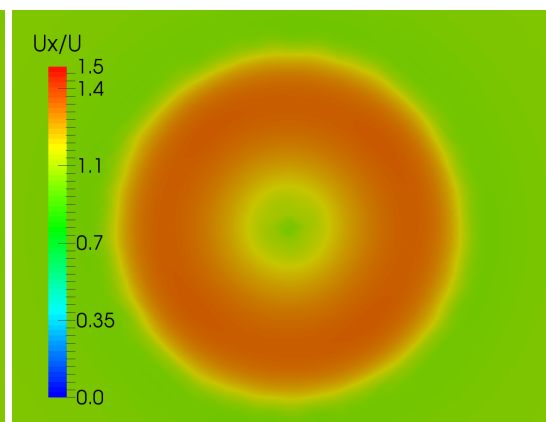


(a) Model idealnog propelera,                    (b) MRF,

Slika 10: Aksijalne komponente brzine u ravnini x $= 0.2R_P$.

Zbog vijka modeliranog prema pretpostavci tankog diska sa beskonačno mnogo lopatica, brzine u presjeku x = 0.2 $R_P$ imaju konstantnu vrijednost ako se promatraju na određenom radijusu. U strujanju iza geometrije vidi se utjecaj konačnog broja lopatica pa se područja s višim i nižim vrijednostima brzine periodički ponavljaju.
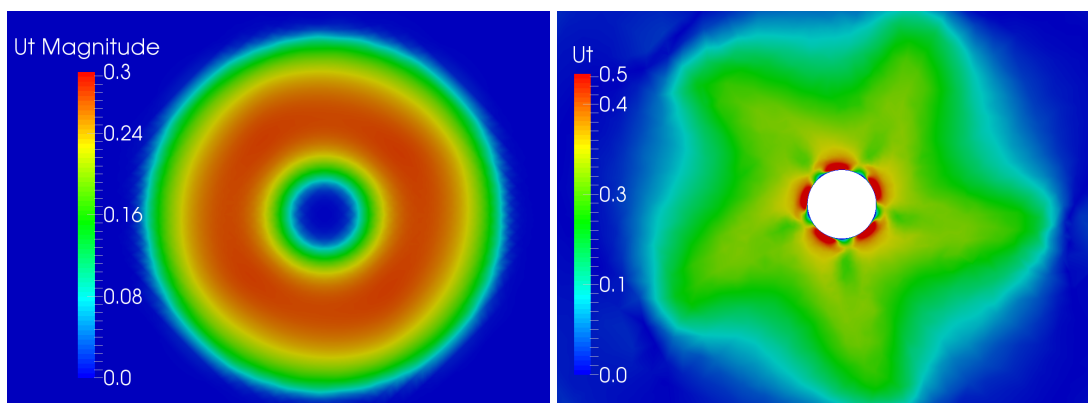


(a) Model idealnog propelera,

(b) MRF,

Slika 11: Tangencijalne komponente brzine u ravnini x = 0.2$R_P$.

Usporedbom srednjih vrijednosti komponenata brzine dobivenih na različitim radijusima može se vidjeti da se aksijalna brzina dobro podudara na svim radijusima u ravnini x = 0.2$R_P$. Što se tiče srednjih vrijednosti tangencijalne brzine, odstupanje je vidljivo za najveći i najmanji radijus. U području između ta dva radijusa tangencijalna brzina se dobro opisuje modelom. Komponente brzine uspoređene su i u ravnini x = 2$R_P$ kako bi se analizirao polje brzine na većoj udaljenosti, gdje se više ne osjeća direktan utjecaj lopatica. Rezultati dviju simulacija su u tom slučaju gotovo podudarni na svim analiziranim radijusima. Dijagrami sa iznosima komponenata brzina na određenom radijusu prikazani su u zadnjem poglavlju diplomskog rada. Prilikom ocjenjvanja kvalitete rezultata modela mora se uzeti u obzir da su oni dobiveni primjenom teorijske distribucije skoka tlaka i tangencijalne brzine na idealnom propeleru. Ako bi se realne distribucije za određeni brodski vijak mogle primijeniti na idealnom propeleru, za očekivati je da bi se polje brzine iza njega još bolje poklapalo sa rezultatima simulacije oko geometrije.

# 1 Introduction

Optimisation of propeller design is one of the most efficient ways to achieve better propulsion performance of ships. For a long time the majority of the knowledge about ships and propeller performance has been collected from model scale bare hull resistance, open water and self propulsion tests. Bare hull resistance tests are performed in a calm water, with no propeller attached, to determine the resistance of the hull model at any given speed. As opposed to that, the open water propeller test is performed only for a propeller in open water. Results of testing in a calm water cannot be the only parameters to be taken into account when designing the propeller, because the conditions in which the hull and propeller operate in such tests are idealized. To be able to design a propeller appropriately, the hull-propeller interaction has to be considered, since it appears in real operating conditions. In self-propulsion tests the propeller is attached to the hull so the hull-propeller interaction can be determined. When the model scale tests are performed, information obtained from them are later used for the determination of the performance of a full scale propeller. Conducting such experiments presents significant cost in time and money.

Computational fluid dynamics (CFD) provides ways of simulating flow fields around different geometries using numerical methods and established algorithms. During recent years, considerable progress in the field of computer science has contributed to the decrease of computational costs of CFD simulations, making it more accessible for practical applications.

Nowadays, the role of CFD methods is increasing in most fluid dynamics applications including the process of ship propeller design. Simulating the aforementioned experiments provides the opportunity to obtain desired results by analyzing calculated flow characteristics. It can be a practical way of obtaining valid results at relatively low costs and in reasonable time in relation to the real experiments. Since the self-propulsion test simulation is still quite expensive and time demanding, the common practice is to simulate only the open water test and to use its results for the determination of self-propulsion characteristics. It can be done by taking into account established interaction factors, which account for the interaction between the hull resistance and open water characteristics of the propeller.

In this thesis the main goal is to compare computational costs and accuracy of different approaches used for numerical modelling of ship propellers. There are several different approaches for simulating ship propellers in CFD. The difference between approaches lies in the level of simplification of the actual phenomenon as a trade-off between accuracy and CPU efficiency. The following approaches for simulating flow around a propeller are tested and compared:

- multiple frames of reference (MRF) for a single blade passage with periodic boundary conditions,

- MRF for a complete propeller geometry,

- transient simulation with rotating mesh and complete propeller geometry.

The MRF model is a steady-state approximation in which individual domain zones can be assigned different rotational and translational speeds. Unlike the transient simulations with a dynamic mesh, the MRF approach does not account for the relative motion of different domain zones. Rotation of rotating parts (in this case the propeller) is included in the mathematical model by the addition of the centrifugal and Coriolis force.

For the purpose of this thesis steady state simulations with MRF model for a single blade and complete propeller geometry were performed for different operating points of the Japan Bulk Carrier (JBC) propeller model [1]. $K_T$ and $K_Q$ curves (thrust and torque) with respect to the advance ratio are obtained. Since the transient simulation of the complete propeller mesh is quite time consuming, it was performed only for the operating point corresponding to the maximum efficiency of the propeller. All simulations are performed using an open source CFD software called `foam-extend` [2].

As stated earlier, self-propulsion test simulation is quite expensive and time demanding. When modelling full interaction between the ship and the propeller, the main problem is the large difference between the time scales of the propeller and hull flow. If the exact prediction of propeller hydrodynamics is not of interest, and its performance characteristics are known in advance, the propeller influence on the flow in such simulations can be modelled with a simplified actuator disc in order to save computer resources. In this thesis the actuator disc model is applied on a simplified, fully structured mesh, and simulation is run for the operating point corresponding to maximum efficiency. The performance is afterwards evaluated against the CFD results for the actual propeller geometry.

The thesis is organized as follows: Section 2. gives an overview of mathematical relations used in thesis. Section 3. describes an open water test of a propeller. Section 4. provides results of different approaches used in the CFD simulation of an open water test. Section 5. presents the theory behind an actuator disc model and gives the comparison between an actuator disc and propeller simulation. Conclusion of the thesis is provided in section 6.

# 2 Mathematical Model

## 2.1 Introduction

The purpose of this section is to introduce the mathematics applied in this thesis. The first subsection gives an insight into the governing equations of the fluid flow. CFD software uses a finite volume method to transform partial differential equations into discrete algebraic equations over finite volumes. The second subsection refers to turbulence models used in simulations. As an efficient way of simulating the flow around rotating geometries, the MRF approach will be introduced in the third subsection. The final subsection explains the Generalized Grid Interface (GGI) [3] model used to connect the non overlapping mesh regions which in this case occur in the one blade passage simulation.

## 2.2 Governing Equations of Fluid Flow

Large number of flow-related problems can be described using transport equations. Transport equations are modelled in different ways, depending on the phenomenon that is considered and so their form may differ. However, the behaviour of dependant variables in all such equations is described with the same set of operators, which allows the formulation of the generic scalar transport equation. The standard form of scalar transport equation is expressed as [4]:

$$\frac{\partial \phi}{\partial t} + \nabla \cdot (\mathbf{u}\phi) - \nabla \cdot (\gamma \nabla \phi) = q_v, \tag{1}$$

where $\phi$ represents the transported scalar variable, $\mathbf{u}$ is the convective velocity and $\gamma$ stands for the diffusion coefficient. $q_v$ on the right hand side of Eq. (1) represents sources or sinks of the transported scalar $\phi$.

The standard transport equation consists of four characteristic terms:

- $\frac{\partial \phi}{\partial t}$ is the temporal derivative of transported scalar which represents the inertia of the system,

- $\nabla \cdot (\mathbf{u}\phi)$ is the convection term. It represents the convective transport of the scalar by the prescribed velocity field $\mathbf{u}$. The term has a hyperbolic nature because it denotes that information comes from the vicinity, defined by the direction of the convection velocity $\mathbf{u}$,

- $\nabla \cdot (\gamma \nabla \phi)$ is the diffusion term which represents the gradient transport. It is an elliptic term, which means: every point in the domain is influenced by every other point in the domain,

- $q_v$ represents sources and sinks that either create or diminish the transported scalar.

The subject of this thesis refers to the motion of incompressible viscous fluids, which is described by momentum conservation or Navier-Stokes equations. To completely describe incompressible fluid flow, the momentum equation is accompanied by the mass conservation and energy conservation equations. As heat transfer is not considered in this thesis, the energy conservation equation is neglected. The governing equations for incompressible, isothermal flow are expressed as follows:

$$\nabla \cdot \mathbf{u} = 0, \tag{2}$$

$$\frac{\partial \mathbf{u}}{\partial t} + \nabla \cdot (\rho \mathbf{u} \otimes \mathbf{u}) - \nabla \cdot (\nu \nabla \mathbf{u}) = \mathbf{g} - \nabla p, \tag{3}$$

where $\mathbf{u}$ is the instantaneous velocity field, $\rho$ is the density of fluid, $p$ is the kinematic pressure, $\nu$ is the kinematic molecular viscosity and $\mathbf{g}$ represents the body forces.

## 2.3  Turbulence Modelling

Although turbulent flow is fully described by Navier-Stokes equations, it is characterized by a wide range of time and length scales, while interactions between vortices are extremely non-linear. Such properties make turbulence hard to describe statistically, which certainly contributes to the complexity of predicting turbulent flow. When predicting turbulent flow there are three approaches in CFD:

- Direct Numerical Simulation (DNS),

- Large Eddy Simulation (LES),

- Reynolds-Averaged Navier Stokes Equations (RANS).

When performing DNS, Navier-Stokes equations are solved for all time and length scales in transient flow without turbulence modelling. Cells in the numerical domain should not be bigger than the size of the smallest turbulence scale in order to resolve the flow properly. Knowing that the large scale structures in the flow have a much larger time scale than the smallest, it is clear that simulating turbulence directly sets high demands on temporal and spatial resolution. Although too expensive for typical engineering practice, DNS are usually used to solve simple flows aiming to improve knowledge about turbulence.

Turbulence models are used to account for the turbulence effects without a need for an extremely fine numerical grid. LES reduces the computational cost by modelling small scale

eddies, while large scale turbulence and coherent structures are simulated. RANS solves the time-averaged Navier-Stokes equations, where turbulent fluctuations are modelled. In this thesis, only the RANS model is used in simulations so it will be explained further.

### 2.3.1 Reynolds Averaged Navier-Stokes Equations

In a large number of problems the mean properties of the flow are of interest, and not the fluctuations due to turbulence. For example, in the case of the open water propeller test, it is important to find the averaged velocity field so integral values (thrust, torque) in steady state can be obtained. When equations are derived so that they depend only on the mean flow characteristics, the transient flow does not have to be solved and a coarser numerical grid can be used.

Velocity and pressure fields can be expressed as a sum of the mean and fluctuating values [5]:

$$\mathbf{u} = \overline{\mathbf{u}} + \mathbf{u}', \tag{4}$$

$$p = \overline{p} + p', \tag{5}$$

where $\overline{\mathbf{u}}$ and $\overline{p}$ are mean values, while $\mathbf{u}'$ and $p'$ are fluctuating parts of velocity and pressure. When the above is substituted into Eq. (1) and Eq. (2), the Reynolds-Averaged Navier-Stokes equations, as well as the time-averaged continuity equation are derived:

$$\frac{\partial \overline{\mathbf{u}}}{\partial t} + \nabla \cdot (\overline{\mathbf{u}}\,\overline{\mathbf{u}}) - \nabla \cdot (\nu \nabla \overline{\mathbf{u}}) = -\nabla \overline{p} + \nabla \cdot (\overline{\mathbf{u}'\mathbf{u}'}), \tag{6}$$

$$\nabla \cdot \overline{\mathbf{u}} = 0. \tag{7}$$

With the mean velocity taking place of the instantaneous velocity, the form of the equations obtained is almost the same compared to Eq. (1) and Eq. (2), except the new term $\overline{\mathbf{u}'\mathbf{u}'}$ appears on the right hand side of the averaged momentum equation. This term is known as the Reynolds-stress tensor. It is a symmetrical second order tensor, which brings six additional unknowns in the system of equations, thus the number of unknowns exceeds the number of equations. In order to close the system, new relations have to be defined.

With reference to the Boussinesq approximation [6], the Reynolds-stress tensor can be modelled as a linear function of an averaged strain rate tensor (which represents the gradient of the flow velocity) and expressed as follows:

$$\overline{\mathbf{u}'\mathbf{u}'} = \nu_t \frac{1}{2}[\nabla\overline{\mathbf{u}} + (\nabla\overline{\mathbf{u}})^T], \tag{8}$$

where $\nu_t$ stands for the turbulent viscosity which is defined as:

$$\nu_t = Au\nabla, \tag{9}$$

where $A$ is a constant which allows adjustment of the model to the physical behaviour, $u$ is the velocity scale and $\nabla$ stands for the length scale. Turbulent kinetic energy $k$, used for approximating the velocity scale, is defined as:

$$k = \frac{3}{2}\mathbf{u}'\mathbf{u}'. \tag{10}$$

The transport equation for turbulent kinetic energy is shown in the next subsection. In order to approximate turbulent viscosity, in addition to modelling the velocity scale, length or time scale needs to be modelled. It is done by formulating the transport equation for turbulent dissipation $\varepsilon$ or specific dissipation $\omega$. Deriving these sets of equations forms two of the established two-equation turbulence models: $k - \varepsilon$ and $k - \omega$. A combination of the aforementioned models is the $k - \omega SST$ model [7] used in this thesis and it will be described further in the following subsection.

### 2.3.2 $k - \omega$ SST **Turbulence Model**

The advantage of the $k - \varepsilon$ over the $k - \omega$ model is low sensitivity to the boundary conditions far from the wall, but at the same time it is unreliable when modelling flows with high and adverse pressure gradients. Flows with such characteristics are better modelled with the $k - \omega$ model. Thus, it follows that the $k - \varepsilon$ is good for predicting flow behaviour away from the wall, while $k - \omega$ is better suited for simulations of complex flow close to the geometry (in a boundary layer).

The $k - \omega SST$ model combines the $k - \varepsilon$ and $k - \omega$ models mentioned above, combining their advantages. Using the $k - \omega$ formulation in the inner parts of the boundary layer allows the application of this model without the use of damping functions, which is not the case for most turbulence models. In the free stream region the model is switched to $k - \varepsilon$ formulation, and thus the sensitivity to free stream conditions is avoided [8].

The transport of the turbulent kinetic energy $k$ and the specific dissipation $\omega$ in the model is expressed as:

$$\frac{\partial k}{\partial t} + \nabla \cdot (\mathbf{u}k) - \nabla[(\nu + \sigma_k \nu_t)\nabla k] = P_k - \beta^* k\omega, \tag{11}$$

$$\frac{\partial \omega}{\partial t} + \nabla \cdot (\mathbf{u}\omega) - \nabla[(\nu + \sigma_\omega \nu_t)\nabla \omega] = \alpha S^2 - \beta \omega^2 + 2\sigma_{\omega 2}(1 - F_1)\frac{1}{\omega}\nabla k \cdot \nabla \omega. \tag{12}$$

The turbulent viscosity is:

$$\nu_t = \frac{a_1 k}{\max(a_1 \omega, SF_2)}. \tag{13}$$

The complementary relations are:

$$F_2 = \tanh\left(\max\left(\frac{2\sqrt{k}}{\beta^* \omega y}, \frac{500\nu}{y^2 \omega}\right)^2\right), \tag{14}$$

$$P_k = \min\left(\tau : \nabla \mathbf{u}, 10\beta^* k\omega\right), \tag{15}$$

$$F_1 = \tanh\left(\min\left(\left(\max\left(\frac{\sqrt{k}}{\beta^* \omega y}, \frac{500\nu}{y^2 \omega}\right), \frac{4\sigma_{\omega 2}k}{CD_{k\omega}y^2}\right)\right)^4\right), \tag{16}$$

$$CD_{k\omega} = \max\left(2\rho\sigma_{\omega 2}\frac{1}{\omega}\nabla k : \nabla \omega, 10^{-10}\right), \tag{17}$$

while closure coefficients have values presented in Table 1.

Table 1: Closure coefficients.

| $\alpha_1$ | $\alpha_2$ | $\beta_1$ | $\beta_2$ | $\alpha_{k1}$ | $\alpha_{k2}$ | $\sigma_{\omega 1}$ | $\sigma_{\omega 2}$ | $\beta^*$ |
|---|---|---|---|---|---|---|---|---|
| $\frac{5}{9}$ | 0.44 | $\frac{3}{40}$ | 0.0828 | 0.85 | 1 | 0.5 | 0.856 | $\frac{9}{100}$ |

Unlike the coefficients used in model equations ($\alpha$, $\beta$, $\alpha_k$, $\alpha_\omega$), closure coefficients subscripted with 1 or 2, have a defined value. Values of the coefficients used in the equations are calculated using a blending function $F_1$:

$$\phi = \phi_1 F_1 + \phi_2(1 - F_1), \tag{18}$$

where $\phi$ represents the coefficient that is used in model equations, while $\phi_1$ and $\phi_2$ stand for closure coefficients and $y$ appearing in Eq. (14) and Eq. (16) is the distance from the wall [7].

## 2.4   Multiple Reference Frame Method

The MRF model is a steady-state approximation in which individual domain zones move at different rotational and translational speeds. The flow in each moving domain zone is solved using the moving reference frame equations. If the zone is stationary ($\omega$=0), the stationary equations are used. At the interfaces between zones, a local reference frame transformation is performed to enable flow variables in one zone to be used to calculate fluxes at the boundary of the adjacent zone. The key is that the MRF approach does not account for the relative motion of moving zone with respect to adjacent zones (which may be moving or stationary), which means that the grid remains fixed during the computation. Hence, the MRF is often referred to as the "frozen rotor approach" [9].

Although the MRF approach is an approximation, it can provide satisfactory results for many applications in turbomachinery (and also for simulation of propeller rotation), where the flow is relatively simple at the interface between zones.

### 2.4.1   Incompressible Navier-Stokes Equations in the Rotating Frame

To describe the incompressible fluid flow in the rotating frame, Navier-Stokes equations need to be rearranged so that the rotational velocity of cells is included. Let's assume an arbitrary vector $\mathbf{A}$ in an inertial reference frame which rotates with constant angular velocity $\omega$. The general relation of the rate of change of vector is:

$$\left[\frac{d\mathbf{A}}{dt}\right]_I = \left[\frac{d\mathbf{A}}{dt}\right]_R + \omega \times \mathbf{A}, \tag{19}$$

where subscript I means inertial, and R rotational. If $\mathbf{r}$ is considered the position vector of the fluid particle, the Eq. (19) can be written as:

$$\left[\frac{d\mathbf{r}}{dt}\right]_I = \left[\frac{d\mathbf{r}}{dt}\right]_R + \omega \times \mathbf{r}, \tag{20}$$

and the expression for velocity is then:

$$\mathbf{u}_I = \mathbf{u}_R + \omega \times \mathbf{r}. \tag{21}$$

Acceleration is expressed as a second time derivative of position vector:

$$\left[\frac{d\mathbf{u}_I}{dt}\right]_I = \left[\frac{d\mathbf{u}_R}{dt}\right]_R + \frac{d\omega}{dt} \times \mathbf{r} + 2\omega \times \mathbf{u}_R + \omega \times \omega \times \mathbf{r}. \tag{22}$$

Term $\frac{d\omega}{dt} \times \mathbf{r}$ accounts for the tangential acceleration, $2\omega \times \mathbf{u}_R$ is the Coriolis acceleration and $\omega \times \omega \times \mathbf{r}$ is the centrifugal acceleration.

Navier-Stokes equations can be recreated by taking into account the above derived acceleration term. The incompressible Navier-Stokes equations and continuity equation for the inertial frame in terms of the absolute velocity take the form as follows:

$$\frac{\mathrm{d}\mathbf{u}_I}{\mathrm{d}t} + \nabla \cdot (\mathbf{u}_I \otimes \mathbf{u}_I) = -\nabla p + \nabla \cdot (\nu \nabla \mathbf{u}_I), \tag{23}$$

$$\nabla \cdot \mathbf{u}_I = 0. \tag{24}$$

By ignoring the temporal derivative and adjusting the equations for the relative reference frame the system of equations used in the MRF model is obtained [10]:

$$\nabla \cdot (\mathbf{u}_R \otimes \mathbf{u}_I) + \omega \times \mathbf{u}_I = -\nabla p + \nu \nabla \cdot \nabla (\mathbf{u}_I), \tag{25}$$

$$\nabla \cdot \mathbf{u}_I = 0. \tag{26}$$

If only the rotating frame is considered, the following formulation is derived:

$$\nabla \cdot (\mathbf{u}_R \otimes \mathbf{u}_R) + 2\,\omega \times \mathbf{u}_R + \omega \times \omega \times \mathbf{r} = -\nabla p + \nu \nabla \cdot \nabla (\mathbf{u}_R), \tag{27}$$

$$\nabla \cdot \mathbf{u}_R = 0. \tag{28}$$

Such a formulation is used for solving the flow in a single rotating frame of reference (SRF), where the entire domain is rotating.

## 2.5   Generalized Grid Interface

Complicated geometries, such as turbomachinery and propellers often require numerical domains made of several separate 3D meshes. Numerical grids are often made in such a way that farfield mesh is much coarser than the mesh closer to the geometry, or so that separated meshes have completely different topology (hexahedral vs. tetrahedral). Neighbouring boundaries of such meshes are non-conformal and because of that communication between two regions is not directly possible. An impractical solution of the problem would be to adjust meshes so that the neighbouring boundaries completely match each other. Single blade simulations are generally performed using periodic boundaries which can be non-matching. Furthermore, in transient turbomachinery simulations relative rotation appears between the boundaries and produces non-conformal interfaces between stationary and moving parts of the domain. In such cases, due to the relative motion between domains, the mesh adjustment can

not solve the problem. GGI is a coupling interface, which offers the possibility of joining such non-conformal regions so that they are able to communicate without having to adjust their mesh topology. The non-conformal regions are coupled at matrix level into a single contiguous domain.

The basic GGI uses weighted interpolation to calculate flow values on a pair of non-conformal coupled boundaries [3]. When setting up the GGI one has to define one patch on each of two non-overlapping boundaries. In order to compute flow values across the interface, the algorithm evaluates a list of GGI weighting factors and the number of faces from one patch that are overlapping the face of other patch. The GGI weighting factors are basically the percentage of surface intersection between two overlapping faces.

Several GGI versions are usually applied in order to simplify the mesh complexity of many complicated simulations. For the purpose of this thesis `cyclicGGI` in `foam-extend` is applied on the simulation of a single blade passage of a propeller. It is a version of the basic GGI that is used to cope with periodic non-conformal meshes. Figure 1 shows a numerical domain with periodic boundaries.
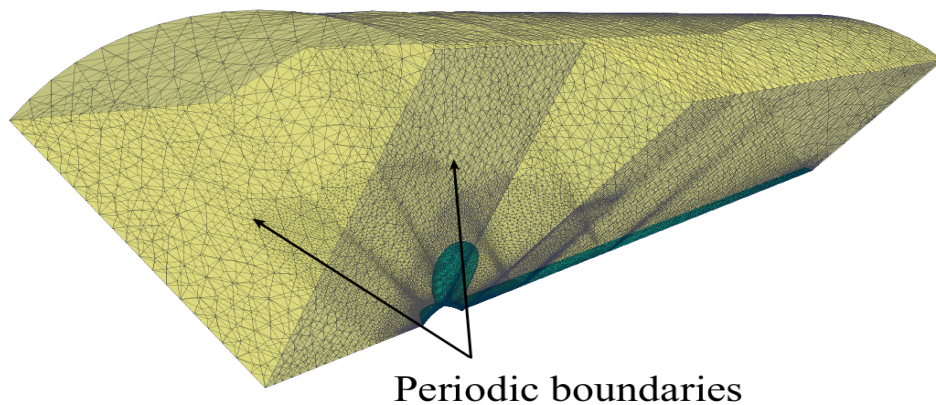


Figure 1: One blade passage domain with periodic boundaries.

The `cyclicGGI` creates a transformed surface of the patch corresponding to one periodic boundary in order to internally superpose its data on top of the other periodic boundary patch data. This step is required so that the patch faces neighbourhood and weighting factors can be found. In the `cyclicGGI` the same internal algorithms are used as in the basic GGI. [3]

## 2.6   Closure

In this section the entire mathematical model applied in this thesis was described. In this thesis several simulation methods are tested, where the mathematical model of each simulation setup is a combination of the aforementioned governing equations, turbulence models, MRF approach and GGI interface model. In each simulation the same turbulence model and governing equations of fluid flow were used: equations for incompressible isothermal fluid flow and $k - \omega SST$ turbulence model. The MRF approach was applied on steady state simulations of one blade passage and complete propeller geometry. In case of a single blade simulation non-overlapping surfaces between periodic boundaries were modelled with GGI. All simulations were performed to obtain open-water characteristics of the JBC propeller. In the next chapter the open-water test setup will be described in detail.

# 3   Propeller Performance Characterisation

Performance characteristics of a propeller can be divided into open water and self propulsion characteristics. Self propulsion characteristics are generated by a propeller when operating behind a body in a mixed wake field. The open water characteristics are related to a propeller working in a steady, undisturbed flow. The open water test of a propeller model is performed to obtain open-water characteristics which specify forces and torques acting on the propeller operating in an undisturbed flow. These characteristics can be used for the estimation of full scale propeller performance. Considering that the subject of this thesis deals with the open water testing, self propulsion measurements are not described. In the first subsection the open water experiment is described, followed by an explanation of the open water characteristics in the second subsection.

## 3.1   The Open Water Test

Open water testing requires an accurately determined setup where the propeller is exposed to an undisturbed flow. There are four types of open water test setup that are often used: a setup for an open propeller, for a ducted propeller, for a pod unit and for a thrusters unit. In this thesis the case of an open propeller is described.

The open water test for an open propeller is carried out on either a stock or an actual model of the propeller to derive its open water characteristics [11]. The experiment can be done by moving the propeller forward through the basin using a towing carriage as shown simplified in Figure 2. The propeller is set on the horizontal driveway shaft which is arranged parallel to the calm water surface and the carriage rails. Typically, the immersion of the shaft axis is equal to the diameter of the propeller.
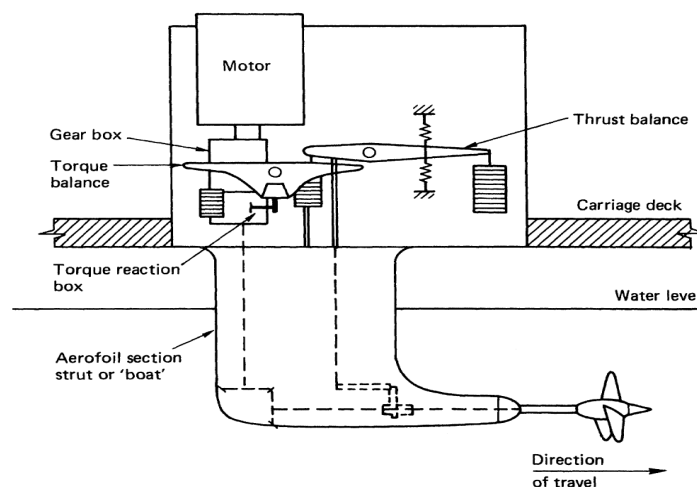


Figure 2: Open water test setup [11].

Traditionally, open water tests of propellers are performed in a steady manner, meaning that, for the specific operating point, the propeller rotates at a constant rate and it is moved forward at fixed velocity. The propeller is driven from the downstream side, because if driven from the upstream side, the drive mechanism creates a flow disturbance, which is not acceptable. Usually the measurements are performed for a series of operating points depending on the different loading of the propeller. The loading is carried out by adjusting the speed of advance ($V_A$) and keeping the propeller revolutions constant [11]. Thrust and torque are measured for each inflow velocity. Several speeds are applied per run and multiple runs are required to obtain the open water diagram. The measured torque and thrust are expressed as non-dimensional coefficients $K_Q$ and $K_T$ which will be described in the following subsection.

## 3.2   Open Water Characteristics

Force and torque produced by the propeller, when performing an open water test, are expressed in terms of a series of non-dimensional characteristics. Non-dimensional terms used to express the general performance characteristics are as follows [11]:

- thrust coefficient:

$$K_T = \frac{T}{\rho n^2 D^4},\tag{29}$$

- torque coefficient:

$$K_Q = \frac{Q}{\rho n^2 D^5},\tag{30}$$

- and advance coefficient:

$$J = \frac{V_a}{nD},\tag{31}$$

where:
$T$ - thrust,
$Q$ - torque,
$D$ - propeller diameter,
$V_a$ - speed of advance,
$n$ - rotational speed,
$\rho$ - fluid density.
The open water propeller efficiency is defined as the ratio of the thrust power to power delivered to the propeller:

$$\eta_0 = \frac{P_T}{P_D}.\tag{32}$$

The above expression can be rearranged so that the efficiency is written as a function of the propellers open water characteristics:

$$\eta_0 = \frac{K_T}{K_Q} \frac{J}{2\pi}. \tag{33}$$

The series of obtained characteristics can be written in a tabular form as shown in Table 2. For a specific propeller, $K_T$, $K_Q$ and $\eta_0$ are functions of the advance coefficient $J$; in an open water diagram they are plotted on the ordinate, while $J$ is plotted on the abscissa. The $K_T$, $K_Q$ versus $J$ curves contain all the information necessary to define the propeller performance at a particular operating condition. An open water diagram for the experimental data listed in Table 2 is shown in Figure 3.

Table 2: JBC propeller characteristics.

| J | $K_T$ | $10K_Q$ | $\eta$ |
|---|---|---|---|
| **0.10** | 0.3267 | 0.3748 | 0.1387 |
| **0.15** | 0.3112 | 0.3629 | 0.2047 |
| **0.20** | 0.2949 | 0.3500 | 0.2681 |
| **0.25** | 0.2777 | 0.3361 | 0.3288 |
| **0.30** | 0.2598 | 0.3210 | 0.3864 |
| **0.35** | 0.2410 | 0.3047 | 0.4406 |
| **0.40** | 0.2214 | 0.2871 | 0.4909 |
| **0.45** | 0.2010 | 0.2682 | 0.5367 |
| **0.50** | 0.1798 | 0.2479 | 0.5771 |
| **0.55** | 0.1577 | 0.2261 | 0.6107 |
| **0.60** | 0.1349 | 0.2027 | 0.6354 |
| **0.65** | 0.1112 | 0.1777 | 0.6475 |
| **0.70** | 0.0867 | 0.1509 | 0.6400 |
| **0.75** | 0.0614 | 0.1224 | 0.5986 |
| **0.80** | 0.0353 | 0.0921 | 0.4879 |
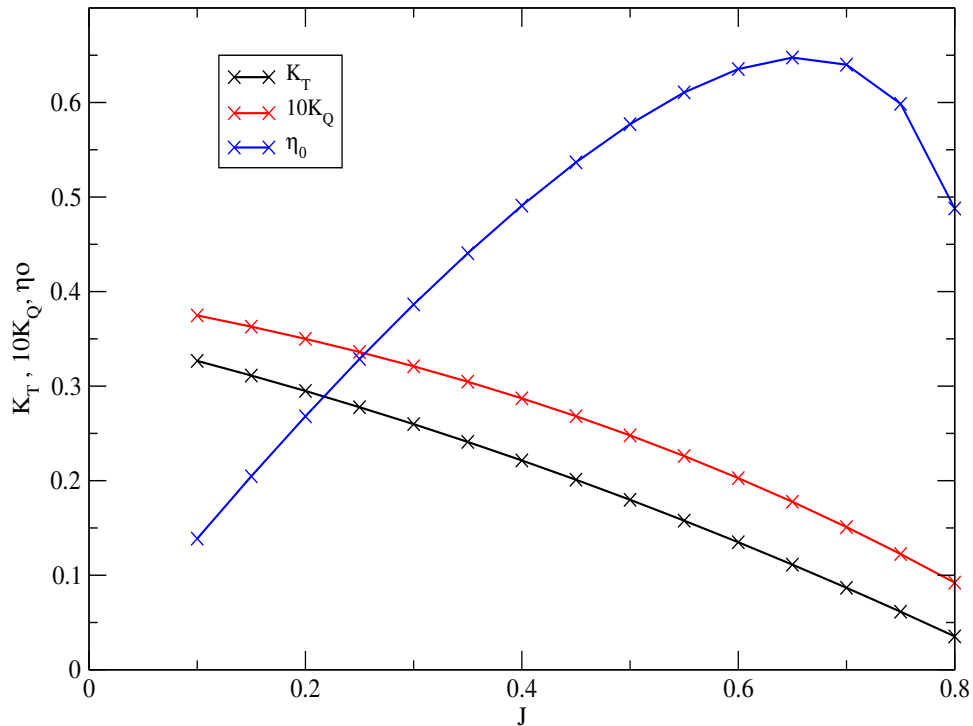
Figure 3: Open water diagram for the JBC propeller model.

The open water experiment is frequently performed on a model of the propeller with a smaller diameter then the actual propeller. From the above expressions it is clear that open water characteristics change depending on the diameter, rotational speed and speed of advance, so the scale effects have to be taken into account when evaluating the full scale propeller characteristics. However, it can be said that, subject to scale effects, the diagram is applicable to any propeller having the same geometric form as the one for which the characteristic curves were derived [11].

## 3.3   Closure

In this section the open water test setup and procedure was described and open water characteristics were explained. For this thesis CFD simulations of an open water test were performed and their results in the form of open water characteristics were compared to actual experimental data to estimate their accuracy. In the next chapter the entire CFD simulation procedure for the JBC propeller model is explained.

# 4 Propeller Simulation

## 4.1 Introduction

This section covers the entire process of CFD simulation of the propeller open water test from mesh generation, to simulation run and postprocessing. Subsection 4.2. gives the geometry parameters of a propeller model. The three following subsections deal with the different simulation approaches in the following order:

- single blade passage simulation, subsection 4.3,

- complete propeller simulation in MRF approach, subsection 4.4,

- transient simulation of a complete propeller, subsection 4.5.

The subsections are organized in such a way that in the first chapter the mesh generation process is explained and substantiated with the description of the obtained mesh. All the meshes are created manually, using commercial mesh generation software *Pointwise* [12]. In the second chapter the respective simulation setup is given. The simulation results are presented in the third chapter .

The efficacy of different approaches is evaluated in subsection 4.6, where the comparison in terms of accuracy and computational time is shown. The accuracy is measured through the comparison of open water characteristics obtained from the CFD simulations against the experimental results.

## 4.2 JBC Propeller Model Geometry

The JBC propeller geometry is provided as a STL file [1]. In Table 3 the propeller characteristics are presented and the propeller geometry is shown in Figure 4.

Table 3: JBC propeller characteristics.

| | |
|---|---:|
| No. of blades | 5 |
| Diameter, $D(m)$ | 0.203 |
| Pitch ratio, $P/D$ | 0.75 |
| Pitch (fixed), $P$ | 0.15225 |
| Expanded area ratio, $A_E/A_0$ | 0.5 |
| Boss ratio, $D_H/D$ | 0.18 |
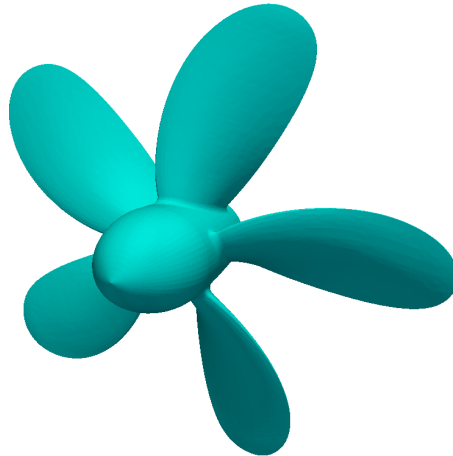
Figure 4: JBC propeller model.

## 4.3   Steady State Simulation for Single Blade Passage

CFD simulations of rotor devices are often run, so that the numerical spatial domain includes only one blade passage. The lateral sides of the domain are modelled with periodic boundary conditions. As stated previously, present periodic boundary conditions allow the data transfer from one side of the domain to the other. The flow values are interpolated between the values on the patches, so that the actual influence of the other blades is simulated. Such simulations are usually less correct, but the computational time is significantly reduced due to the smaller spatial domain.

### 4.3.1   Numerical Spatial Domain

The surface mesh is created manually and it is fully structured, as shown in Figure 5. The volume mesh of a single blade passage of the propeller is made of a single cell zone.
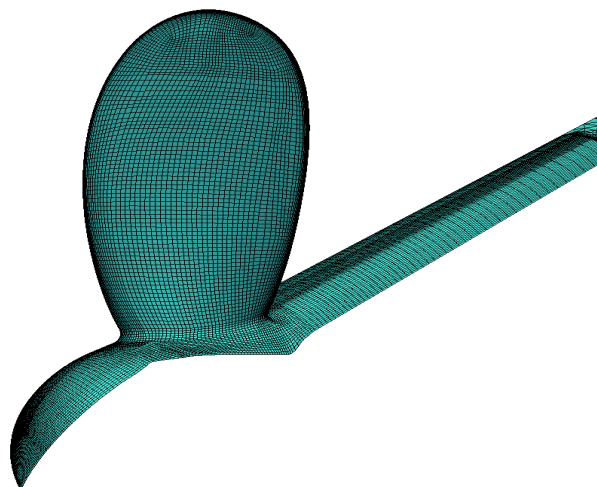


Figure 5: Surface mesh of one propeller blade.

Since the rotor of the propeller consists of five blades, the lateral sides of the domain are created so that they form an angle of 72 ° between them. The domain size is defined so that the disturbance of the flow caused by the geometry does not influence the flow on the boundaries. The following dimensions are expressed relative to the propeller diameter (D): The outlet of the domain is set at a distance of 20D downstream from the mid point of the hub and the inlet is at a distance of approximately 4D upstream. In the radial direction the domain stretches approximately 5D from the propeller axis. In Figure 6 the shape of the spatial domain is shown.
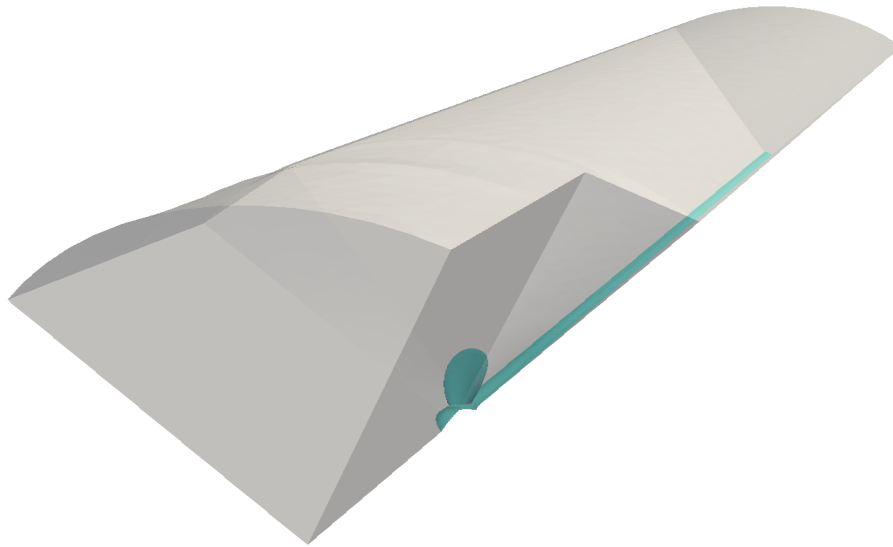


Figure 6: Numerical spatial domain of a single blade passage.

The volume mesh is hybrid, meaning that part of it is structured (made of hexahedral volumes) and the rest is unstructured (made of tetrahedral volumes). It is created using the *T-Rex* mesher in *Pointwise*. The surfaces that form the closed volume need to be selected and a solver is run afterwards to fill the space in-between with cells. It starts building the cells from the structured surface mesh, extruding hexahedra from it. When the prescribed number of structured layers is reached, the domain is further filled with the prisms and tetrahedra. Special attention has to be given to the mesh near the geometry because the proper resolution of the flow in that area determines the quality of the simulation results. In that region, the highest velocity and pressure gradients are expected so it is important to have sufficiently small cells. The majority of the cells are located in the small area just in front and behind the geometry as shown in Figure 7.
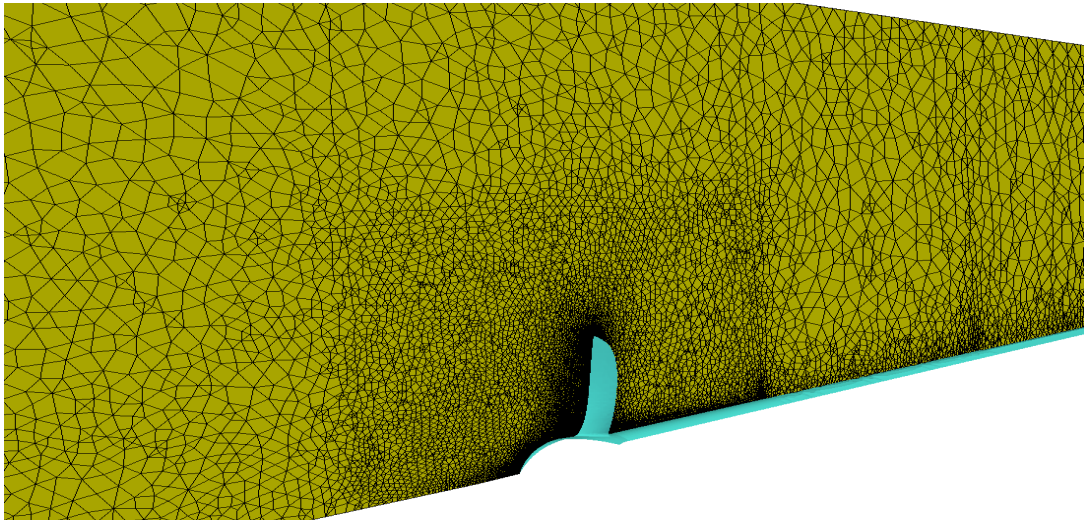
Figure 7: Cross section view of a single blade passage volume mesh.

Figure 8 shows the transition from the structured mesh near the geometry to the further tetrahedral mesh. Note in Figure 8 (Detail 1) that the number of structured layers is not uniform in all areas. In some areas (e.g. close to intersection of the domain boundary and the hub of the propeller shown in Figure 9) it is impossible to make a desired number of structured layers and meet the mesh quality criteria at the same time. Such regions are then filled with tetrahedra, which allows preservation of the cells shape and relations between particular cells according to the criteria.
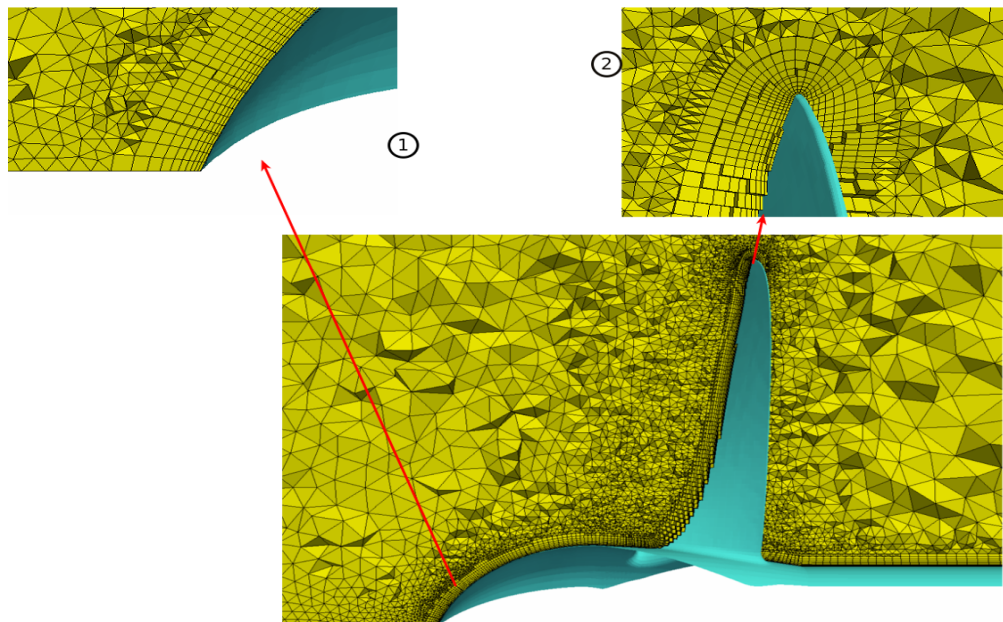


Figure 8: Hybrid mesh transition from the structured to the unstructured cells.
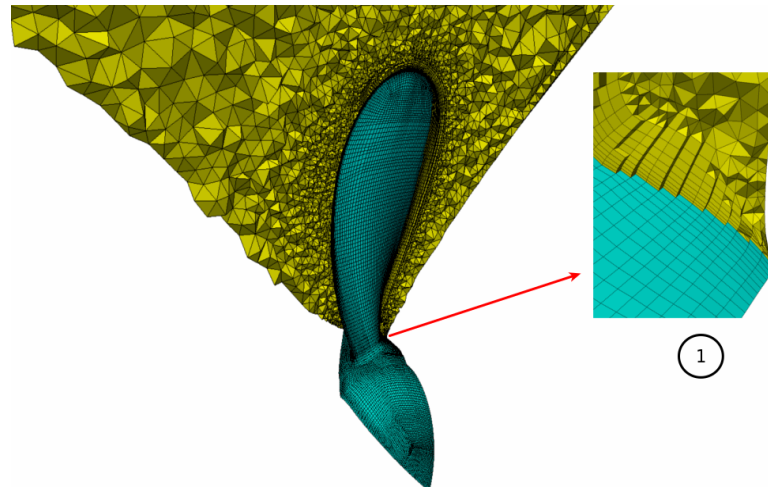
Figure 9: Tetrahedral cells in the boundary layer.

To capture the near wall behaviour of the flow, the centre of the first cell needs to fall in the inner part of the boundary layer which, again, depending on the distance from the wall, can be a laminar, buffer or inertial sublayer. In this case the height of the cells in the first layer from the wall is set so that $y^+$ is less than 1. Defining $y^+$ being less than 1 sets the centre of the first cell in the laminar sublayer and enforces the low Reynolds formulation near the wall.

The mesh is created in an attempt to reach the compromise between the simulation accuracy and computational time. Therefore, the areas which play a big part in the simulation results are made with a higher resolution of cells, while the parts with lower effect on the flow are meshed unstructured and with lower resolution in order to reduce the computational time. The total number of cells is 1 026 930 and their breakdown by topology is given in Table 4.

Table 4: Single blade propeller mesh topology.

|  | Number of cells |
|---|---|
| Hexahedra | 161 266 |
| Prisms | 599 |
| Pyramids | 95 611 |
| Tetrahedra | 769 454 |
| **Total** | 1 026 930 |

Mesh quality is evaluated using the `checkMesh` tool in `foam-extend` and the output is presented in Table 5. Since the tight regions occur in the domain as a consequence of intersection between the cylindrical surface of the hub and the lateral boundaries, the domain is partly filled with badly shaped cells. Therefore, the mesh quality indicators are not ideal. However, there are not too many bad quality cells in the domain (e.g. there are only 4 cells surpassing the skewness threshold) so the simulation runs smoothly.

Table 5: Cell quality of a single blade mesh.

|  | Average | Maximum | Threshold |
|---|---|---|---|
| **Aspect ratio** | - | 813.33 | - |
| **Skewness** | - | 4.966 | 4 |
| **Non-orthogonality** | 21.289 | 89.297 | 70 |

### 4.3.2 Simulation Setup

The steady state MRF approach, also called "Frozen Rotor Approach" is applied for this simulation. The solver used for this simulation is based on a SIMPLE algorithm that is used for steady state analyses. Considering that it is an approximation of the transient phenomena, it is expected to calculate the flow with a specific error due to the fact that the time derivative is neglected in the governing equations of the solver. However, in this case the main goal is to calculate the forces and torques acting on the propeller and not the actual transient behaviour of the flow, so a simplification of this kind is reasonable.

Since the mesh is created as a single cell zone, the entire spatial domain is referred to as a single moving reference frame. On the inlet of the domain the Dirichlet boundary condition defines the constant value of velocity. Since the simulations are run for all operating points for which experimental data are known, the velocity on the inlet boundary is changed for each one of them. The constant velocity boundary condition is also set on the propeller and the shaft, defining them as the stationary parts, which is a typical "Frozen Rotor" setting. The velocity on the outlet is defined with `inletOutlet` boundary condition. It switches between the Neumann boundary condition when the fluid flows out of the domain at the boundary, and the Dirichlet when the fluid is flowing into the domain. Following a common practice for incompressible simulations, the pressure on the outlet is set to a fixed value of 0 Pa. The periodic boundaries (named Periodic1 and Periodic2) are defined with `cyclicGgi` boundary condition. The internal field values are initialized using the `potentialFoam` solver, which solves the equations for the potential flow. It is a good method to speed up the convergence of the simulations that are performed using more complicated solvers. In Table 6 the pressure and velocity boundary conditions are listed.

Table 6: Velocity and pressure boundary conditions for the single blade passage simulation.

| **Boundary** | **Velocity boundary condition** | **Pressure boundary condition** |
|---|---|---|
| Inlet | Dirichlet | Neumann |
| Outlet | `inletOutlet;`<br>`inletValue uniform (0 0 0);`<br>`value uniform (`$U_x$` 0 0);` | Dirichlet |
| Propeller | Dirichlet | Neumann |
| Periodic1 | `cyclicGgi;` | `cyclicGgi;` |
| Periodic2 | `cyclicGgi;` | `cyclicGgi;` |
| Farfield | Neumann | Neumann |
| Shaft | Dirichlet | Neumann |

Initial turbulence values on the inlet, periodic boundaries and the propeller are calculated using empirical expressions based on the turbulence length scale and turbulence intensity. As they depend on the fluid velocity, the values on the inlet are calculated for every operating point. Since the turbulence intensity is approximated as 1% it is expected that the prescribed turbulence values do not have a significant effect on the results of simulations. For the $k - \omega$SST model the turbulence kinetic energy and specific dissipation rate are defined. Turbulence kinetic energy is calculated as a function of the turbulence intensity and the fluid velocity on the inlet of the domain [5]:

$$k = \frac{3}{2}(\mathbf{u}_{inlet}I)^2. \tag{34}$$

The specific dissipation rate is expressed as:

$$\omega = \frac{\varepsilon}{\beta k}, \tag{35}$$

while $\varepsilon$ is calculated as:

$$\varepsilon = \frac{C_\mu^{\frac{3}{4}} k^{\frac{3}{2}}}{l}. \tag{36}$$

Although the values calculated from previous expressions would not be completely correct in most cases, it is important to note that drastic changes of fixed turbulence values do not result in a significantly different solution of the flow.

To simulate the rotation of the domain with the MRF approach the rotating cell zones and their corresponding angular velocities have to be defined. Since the propeller rotation is constant in each operating point of an open water test, the rotation properties of each simulation

are set in the same way.

In Table 7 the linear solver settings for this simulation are shown. An algebraic multigrid solver `amgSolver` is used with the PAMG policy for the pressure, while for the other variables the stabilized biconjugate gradient solver [13] with diagonal incomplete-lower-upper (DILU) preconditioner is used.

Table 7: Linear solver settings for single blade passage simulation.

| Variable | Linear solver | Tolerance | Relative tolerance |
|----------|---------------|-----------|--------------------|
| $p$ | amgSolver (PAMG) | 1e-07 | 0.01 |
| $U$ | BiCGStab (DILU) | 1e-07 | 0.01 |
| $\omega$ | BiCGStab (DILU) | 1e-07 | 0.01 |
| $k$ | BiCGStab (DILU) | 1e-07 | 0.01 |

To improve the stability and convergence of steady state simulations, the relaxation factors need be modified. In that way the variable change from one iteration to the next is limited. The solution under-relaxation is set as shown in Table 8.

Table 8: Solution under-relaxation for a single blade passage simulation.

| Variable | Relaxation factors |
|----------|--------------------|
| p | 0.3 |
| U | 0.5 |
| $\omega$ | 0.5 |
| k | 0.5 |

### 4.3.3   Simulation Results

The flow fields obtained from a single passage simulation are shown in this subsection. All the following representations are made in an open source application for data visualisation called *ParaView*. The postprocessing tools in *ParaView* [14] allow copying of the single blade domain around the propeller axis so that the flow fields can be observed in relation to the complete propeller simulation results.

The following figures show the obtained pressure and velocity fields for the operating point corresponding to maximum efficiency ($J = 0.65$). Incompressible solvers use a kinematic pressure when solving Navier-Stokes equations. It is obtained by dividing the pressure by the fluid density and therefore all the scales relating to pressure are expressed in $m^2/s^2$. In Figure 10 the pressure wake field is shown. In Figure 11 the pressure field is shown in the x=const. plane that intersects the propeller. The propeller rotation can be indicated just by observing the pressure distribution around the propeller blades. Observation of the area

around the tip of the blades in Figure 11 shows that looking in a clockwise direction the areas with higher pressure come first and the areas with lower pressure come afterwards. It means that propeller is rotating counterclockwise. Pressure field values are the main indicator for the assessment of the occurrence of the cavitation phenomena. As mentioned, in the above figures the pressure is expressed as kinematic. For the occurrence of cavitation the negative kinematic pressure should be almost two orders of magnitude larger (around -100 $m^2/s^2$). Since the kinematic pressure drop is not significant at any area on or near the propeller blades, cavitation does not occur in this case and so it is not considered.
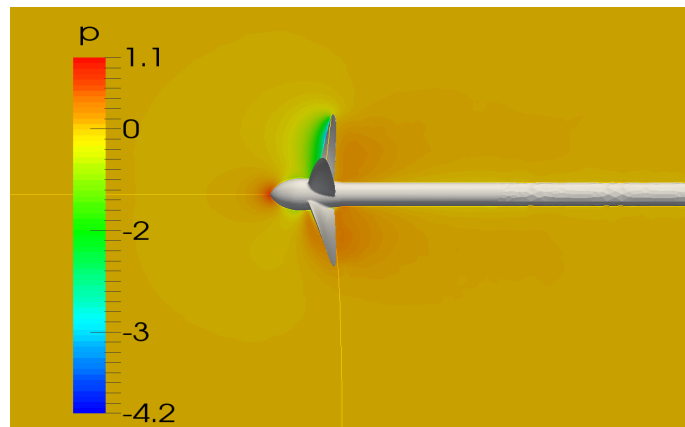


Figure 10: Pressure field obtained with the single blade simulation, $m^2/s^2$.
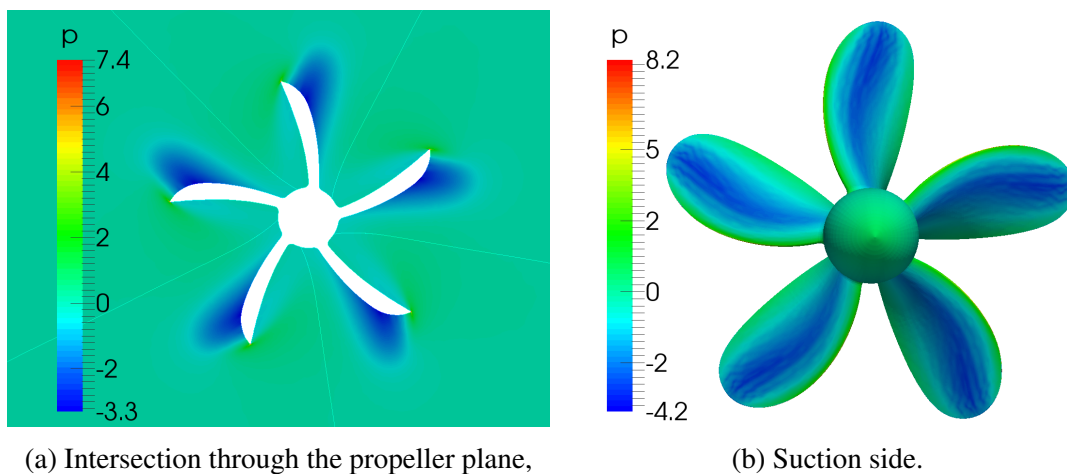


(a) Intersection through the propeller plane,                    (b) Suction side.

Figure 11: Pressure distribution in the propeller plane (single blade simulation), $m^2/s^2$.

In Figure 12 the axial velocity distribution is given. The maximum absolute velocity appears on the tip of the blades due to the highest tangential velocity at this location. In order to present the vortical structures in the flow around and behind the propeller the Q contours are shown in Figures 13 and 14. Q stands for a second invariant of velocity gradient [15] and is calculated as:

$$Q = \frac{1}{2}(|\mathbf{A}|^2 - |\mathbf{S}^2|), \tag{37}$$

where $\mathbf{A}$ represents the rotation rate tensor and $\mathbf{S}$ is the strain rate tensor. The criterion for vortex occurrence is a positive value of Q. For a greater value of Q only vortices with a higher energy rate appear in the area. When the Q value is lower, more vortices that match the criterion appear in the area that is observed. Figure 13 shows the Q-contour for Q values of 3000. In Figure 14 more vortical structures can be seen as the value of the Q-contour is set to 100.
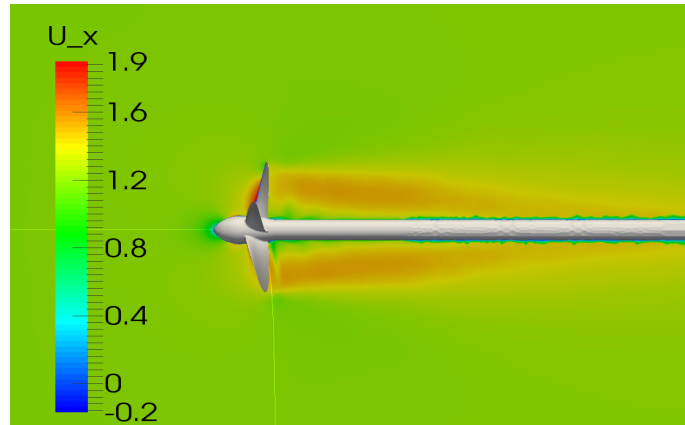


Figure 12: Velocity field obtained with the single blade simulation, m/s.
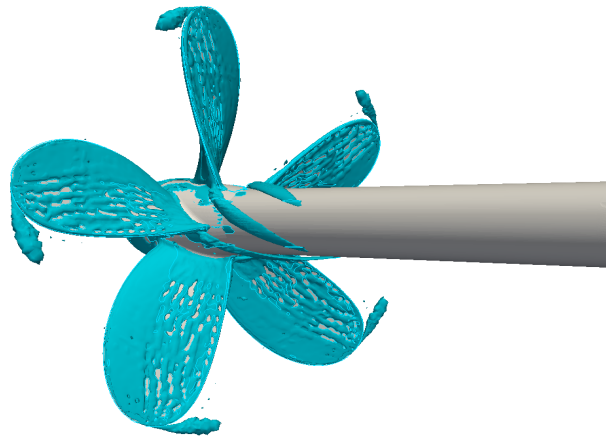


Figure 13: Vortices matching Q = 3000 criterion in single blade simulation.
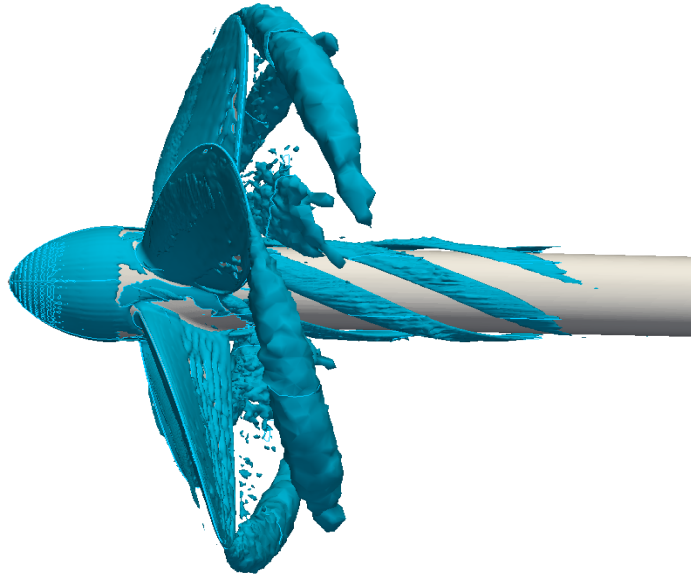
Figure 14: Vortices matching Q = 100 criterion in single blade simulation.

The turbulent kinetic energy distribution is shown in Figure 15. The turbulent kinetic energy has a value that is multiple times lower on the leading edge region than on the trailing edge. The reason for this can be interpreted from Figure 11b. There it can be seen how adverse pressure gradients appear just behind the middle of the blade surface. Specific turbulent dissipation is shown in Figure 16. In Detail 1 the large values of turbulent dissipation can be seen in the proximity of the blade surface.
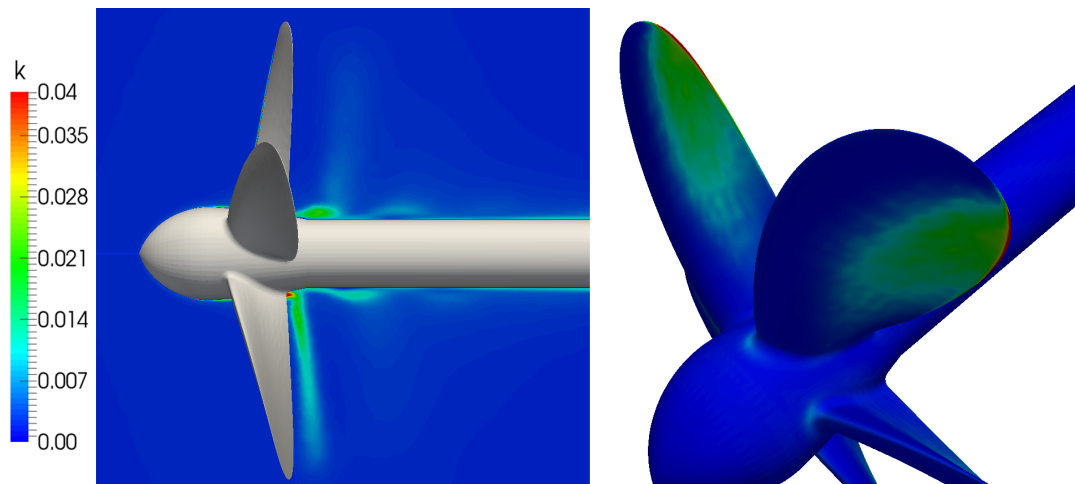


Figure 15: Turbulence kinetic energy (single blade passage), $m^2/s^2$.
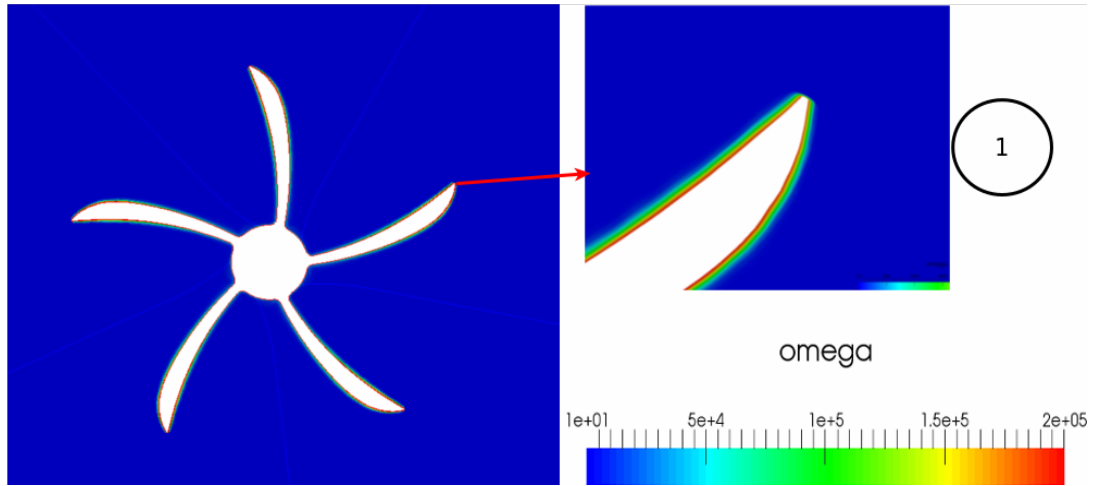
Figure 16: Specific turbulence dissipation rate in the propeller plane, $s^{-1}$.

## Open water characteristics

The single blade passage simulations are run for every operating point from Table 2. The forces and moments acting on the propeller are obtained by integrating the pressure and skin-friction forces over the defined patches. The obtained data are then transformed into non-dimensional coefficients through expressions Eq. (29), Eq. (30) and Eq. (31) and shown in Table 9.

Table 9: Open water characteristics for single blade simulation.

| J | $K_T$ | $10K_Q$ | $\eta_0$, % |
|------|--------|---------|-------|
| **0.10** | 0.3443 | 0.4119 | 13.30 |
| **0.15** | 0.3317 | 0.4012 | 19.74 |
| **0.20** | 0.3175 | 0.3892 | 25.96 |
| **0.25** | 0.2943 | 0.3708 | 31.58 |
| **0.30** | 0.2835 | 0.3607 | 37.53 |
| **0.35** | 0.2638 | 0.3437 | 42.76 |
| **0.40** | 0.2451 | 0.3252 | 47.98 |
| **0.45** | 0.2262 | 0.3057 | 52.99 |
| **0.50** | 0.1965 | 0.2834 | 55.19 |
| **0.55** | 0.1717 | 0.2592 | 57.98 |
| **0.60** | 0.1460 | 0.2334 | 59.74 |
| **0.65** | 0.1190 | 0.2063 | 59.71 |
| **0.70** | 0.0905 | 0.1746 | 57.77 |
| **0.75** | 0.0623 | 0.1432 | 51.95 |
| **0.80** | 0.0325 | 0.1090 | 37.98 |

By observing the diagram in Figure 17 it is noticeable that the torque and efficiency curves are not as smooth as in the experimental diagram. This is most obvious on the $\eta_0$-curve in the area between $J = 0.3$ and $J = 0.4$. Points on the diagram marked with the "x" symbol present the experimental results. Note that, due to the solution error, the maximum efficiency point of the simulation and the experimental data do not correspond to the same advance coefficient. Unlike the experimental data, where the efficiency curve has its peak (64.75%) at $J = 0.65$, the simulation results show the maximum efficiency for $J = 0.60$ (59.75%). Efficiency at $J = 0.65$ is slightly lower at 59.70%.
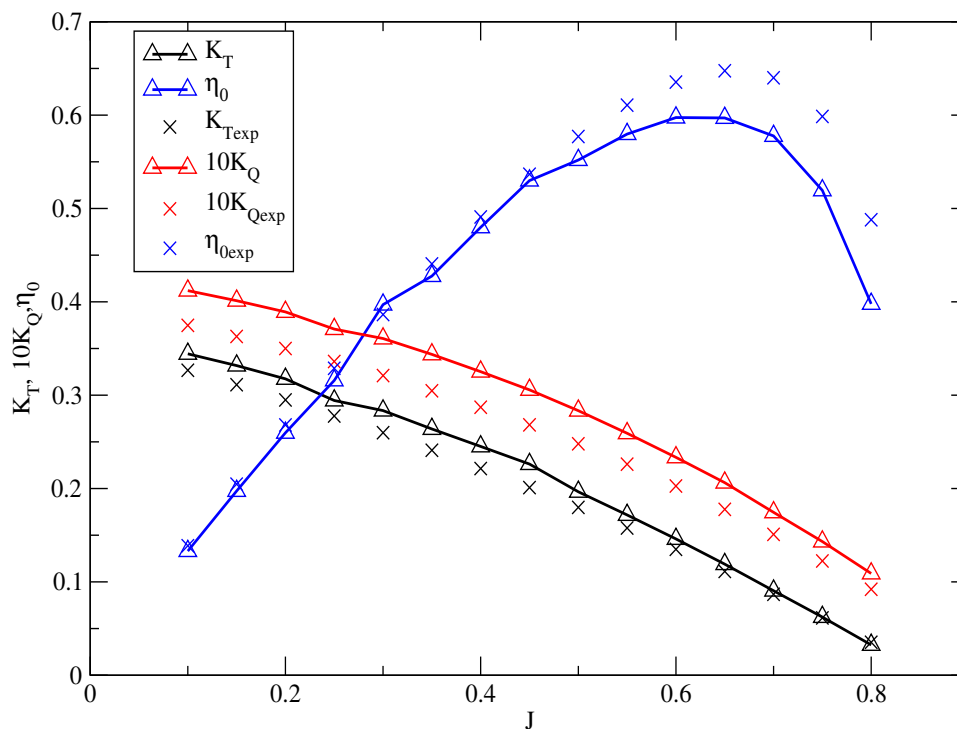


Figure 17: Open water diagram for single blade simulation.

## Convergence curves

The forces and torques are calculated and written for each iteration. They are transformed into the thrust and torque coefficient so that the solution of the coefficient, and not the force is tracked. The diagram in Figure 18 shows the convergence of the open water characteristics solution obtained with the single blade passage simulation for $J = 0.65$. The simulation is run for 2500 iterations. From Figure 19 it can be seen that the solution of $K_\mathrm{T}$ has changed very little (approximately 0.015 %) in the last 500 iterations so it is considered that the solution has converged. The same applies for the torque coefficient solution.
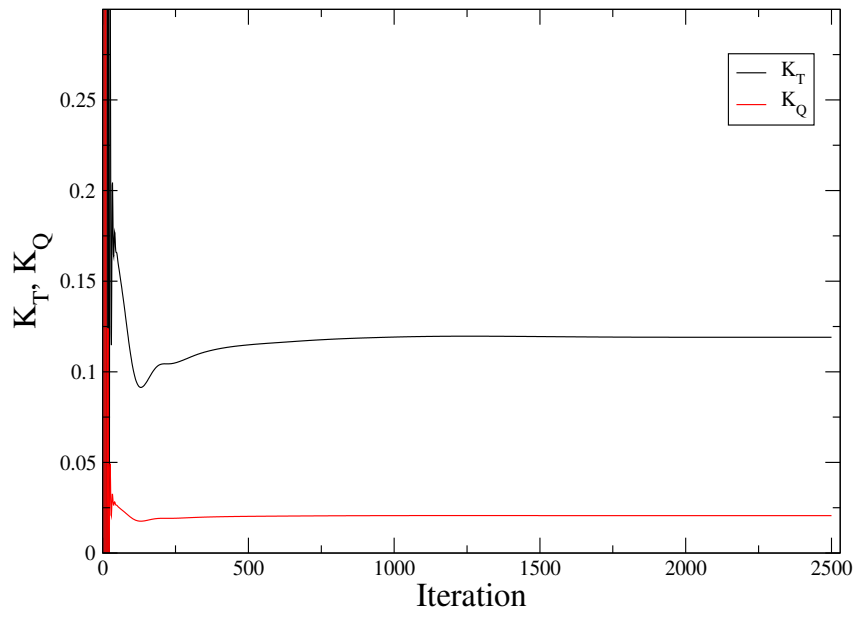
Figure 18: Open water coefficients convergence.
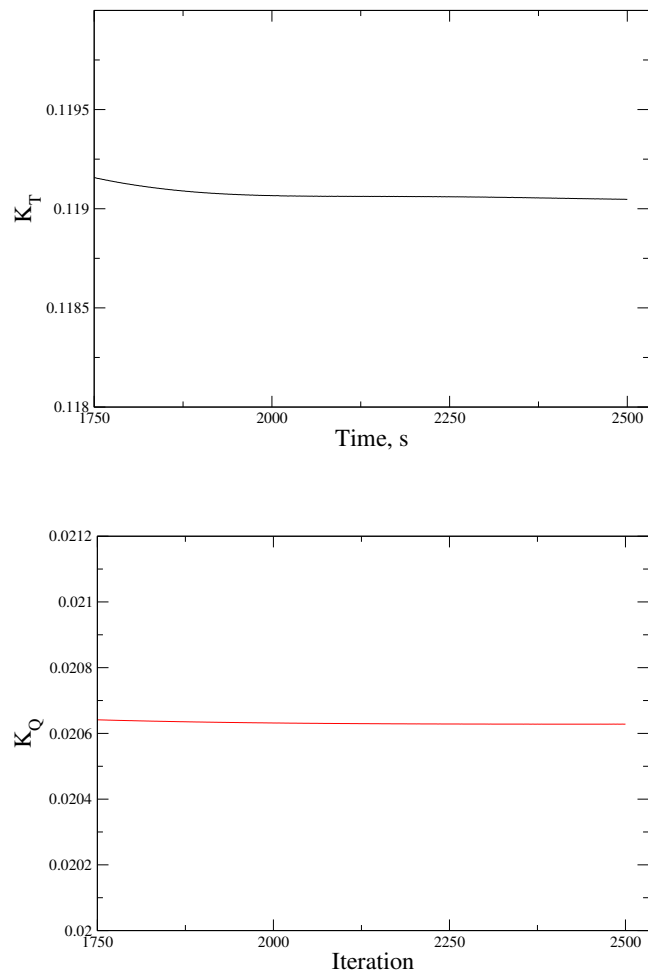


Figure 19: $K_T$ and $K_Q$ convergence for a single blade passage.

## 4.4   Steady State Simulation for Complete Propeller Mesh

The simulation of the complete propeller mesh is performed in MRF approach without any interface modelling. Since the whole propeller geometry is simulated, the numerical spatial domain is much larger than in the single blade simulation.

### 4.4.1   Numerical Spatial Domain

The surface mesh of the complete propeller geometry is obtained by copying and merging the single blade surface mesh around the propeller axis. Figure 20 shows the complete propeller surface mesh. A more detailed representation of surface mesh is given in Figure 21.
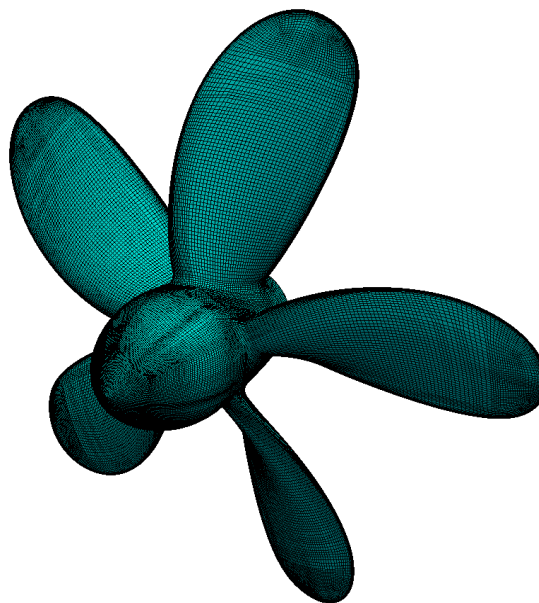


Figure 20: Complete geometry surface mesh.
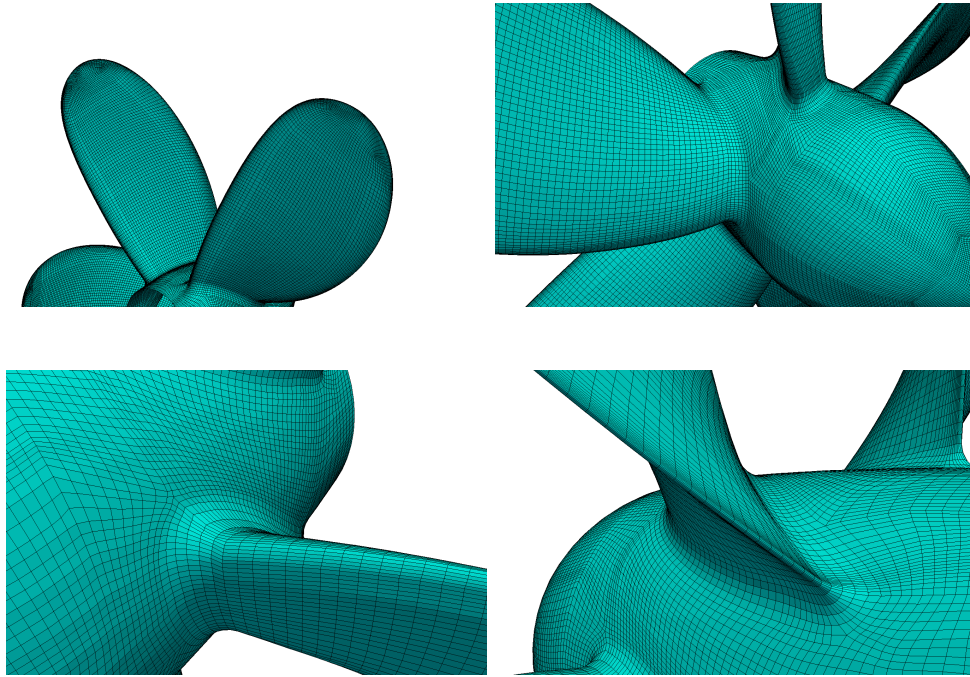
Figure 21: Details of surface mesh of complete propeller geometry.

The dimensions of the single blade passage domain proved to be sufficient, so the outlet and inlet distances from the propeller are the same. The outer frame of the spatial domain is made by rotating the frame of a single blade passage domain around the propeller axis. The spatial domain of complete propeller simulation is shown in Figure 22.
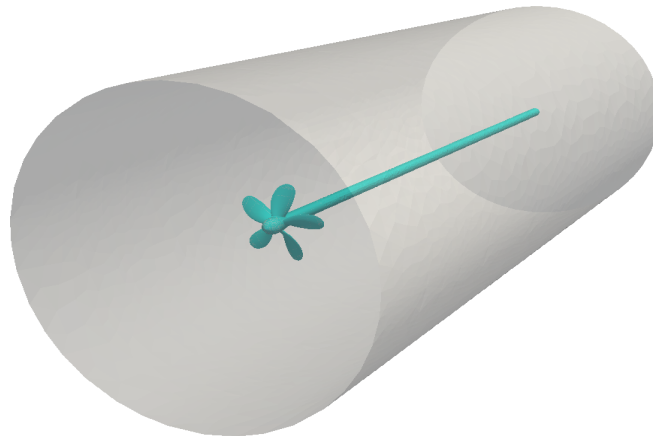


Figure 22: Numerical spatial domain of JBC propeller model.

The volume mesh is also hybrid, created in the same way as for the single blade passage. The boundary layer and the area near to the geometry is again structured, while the further regions are unstructured. An unstructured mesh on the surface of the outer boundaries of the domain is shown in Figure 23, while in Figure 24 the transition from finer hexahedral to coarse tetrahedral mesh is presented. Since there are no acute angles between the domain boundaries and the geometry, the grid criteria are a lot easier to satisfy and therefore mesh generation is less demanding than for the single blade.
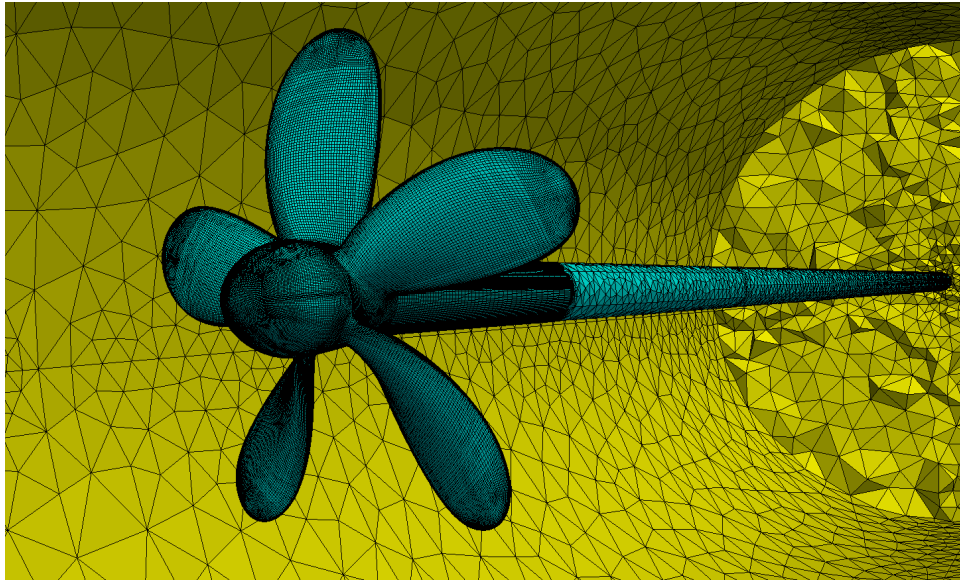


Figure 23: Unstructured farfield mesh.
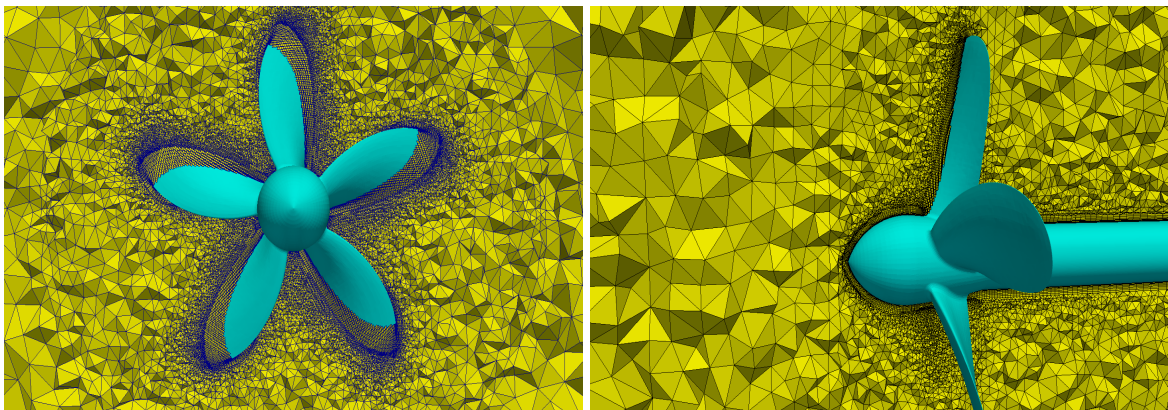


Figure 24: Cross section view of the volume mesh.

The height of cells in the first layer from the wall is determined by the $y^+ = 1$ criterion, the same as in the one blade mesh. The lack of contact between the geometry and the domain boundaries allow the creation of a somewhat coarser grid in the vicinity of the geometry, while keeping the mesh quality criteria matched. Furthermore, the hexahedra to total number of cells ratio is increased due to the same reason because the solver does not need to fill so many tricky

parts of the domain with the tetrahedra. The complete propeller mesh counts 3 913 882 cells as shown sorted by topology in Table 10. Table 11 gives the information about the numerical grid quality.

Table 10: Complete propeller mesh topology.

|  | Number of cells |
|---|---|
| Hexahedra | 1 023 745 |
| Prisms | 20 |
| Pyramids | 468 506 |
| Tetrahedra | 2 421 611 |
| **Total** | 3 913 882 |

Table 11: Cell quality of complete propeller mesh.

|  | Average | Maximum | Threshold |
|---|---|---|---|
| **Aspect ratio** | - | 75.934 | - |
| **Skewness** | - | 1.787 | 4 |
| **Non-orthogonality** | 20.05 | 86.138 | 70 |

### 4.4.2 Simulation Setup

The steady state simulation of complete propeller geometry is performed using the same approach as the steady state single blade simulation. The difference is that there are no periodic boundaries in this spatial domain. The boundary conditions are presented in Table 12.

Table 12: Velocity and pressure boundary conditions for steady propeller simulation.

| Boundary | Velocity boundary condition | Pressure boundary condition |
|---|---|---|
| Inlet | Dirichlet | Neumann |
| Outlet | `inletOutlet;`<br>`inletValue uniform (0 0 0);`<br>`value uniform (`$U_x$` 0 0);` | Dirichlet |
| Propeller | Dirichlet | Neumann |
| Farfield | Neumann | Neumann |
| Shaft | Dirichlet | Neumann |

    The turbulence properties are the same as for the single blade simulation. The only difference is that in this case the numerical domain is divided into two cell zones and the one containing the propeller geometry is set as rotating in the MRF dictionary. As there is no

actual rotation in the MRF approach, there is no relative motion between the two zones, so there is no need to model the interface between them.

Regarding the linear solver control, the same solvers with the same preconditioners as in the single blade passage simulation were chosen. Under-relaxation settings are also the same as the ones listed in Table 8.

### 4.4.3   Simulation Results

To compare the approaches, the results of complete propeller simulation are presented in a form similar to the results from the single blade passage simulation. Resulting flow fields are related to the $J = 0.65$ operating point. In Figure 25 the pressure distribution over y=const. and x=const. planes is shown (see Figures 10 and 11 for comparison).



(a) Plane y=const.,                                 (b) Plane x=const.,
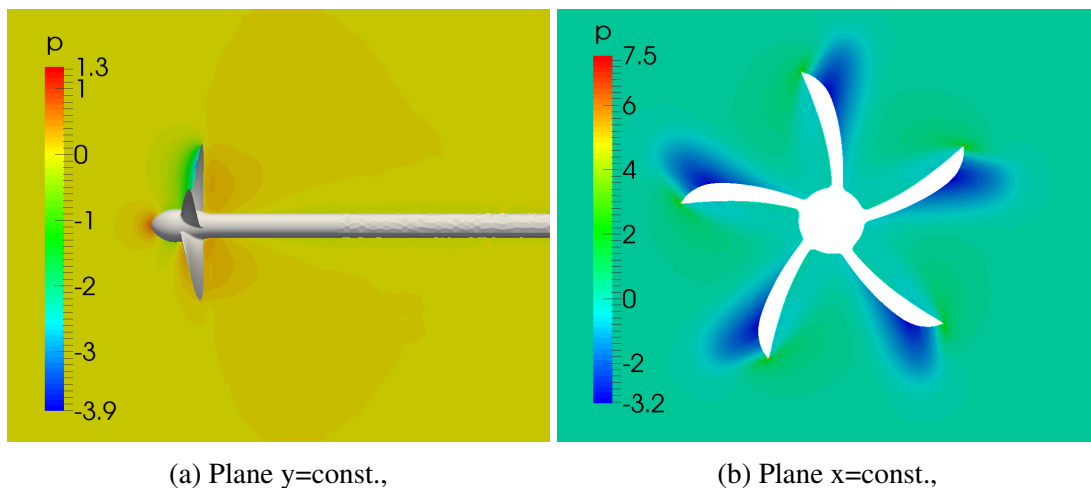
Figure 25: The pressure field obtained with the MRF simulation of complete propeller, $m^2/s^2$.

The pressure distribution over the pressure and suction side of the propeller blades is given in Figure 26. The Detail 1 shows the area of the highest pressure on the leading edge of the blade.

(a) Suction side,                                    (b) Pressure side,
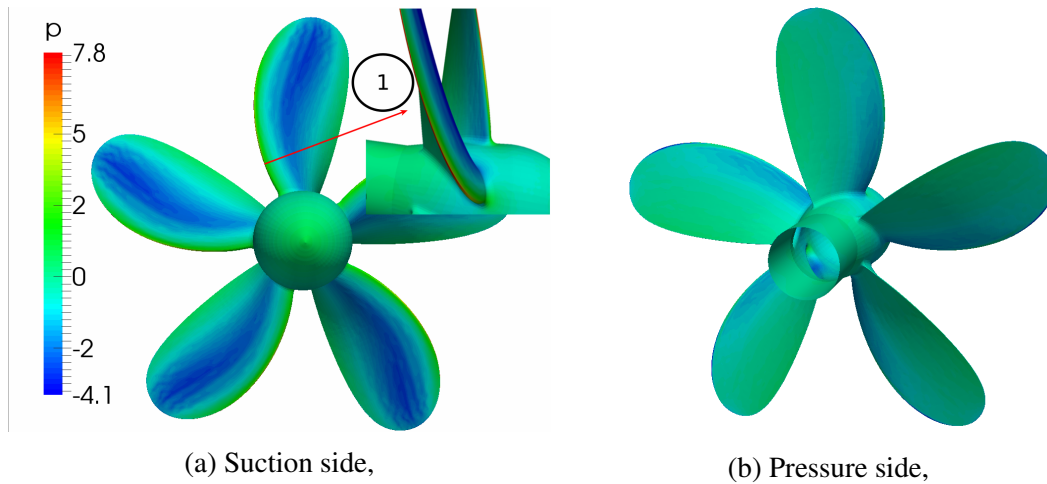
Figure 26: Pressure distribution over the blades (complete propeller simulation), $m^2/s^2$.

Axial velocity distribution in relation to inlet velocity is given in Figure 27. In Figure 27b the velocity streamlines are shown. It can be seen how the modelling of domain rotation with the addition of the forces effects the streamlines passing the propeller plane, causing the swirl in the flow. The streamlines are coloured accordingly to velocity magnitude. The highest velocity (approximately 5.6m/s) occurs on the tip of the propeller blades. Since the velocity behind the propeller is the object of the observation and not the velocity on the blades, the maximum on the scale is set to a lower value so that it is easier to distinguish between the area with the different magnitude.



(a) Axial velocity in the plane x = const.,        (b) Velocity streamlines in the wake,
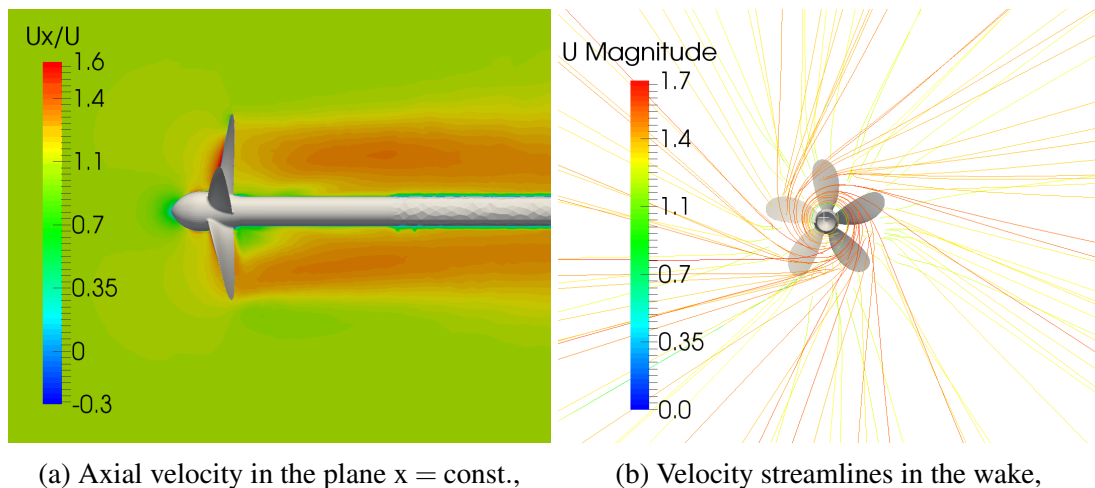
Figure 27: Velocity fields (complete propeller simulation), m/s.

The Q-contours are shown in Figure 28. Note that the vortices do not stretch as far as the vortices from a single blade simulation. As already stated the numerical domain in this case is divided into two zones. The cylindrical zone around the propeller is defined as the MRF zone with rotation components and its boundary in the downstream direction is close to the propeller blades. Since the other zone is stationary, the vortices disappear at the boundary

between them. Figure 29 shows the turbulence kinetic energy which has the same distribution as in the simulation where periodic boundaries are used.



(a) Q = 3000,           (b) Q = 100,
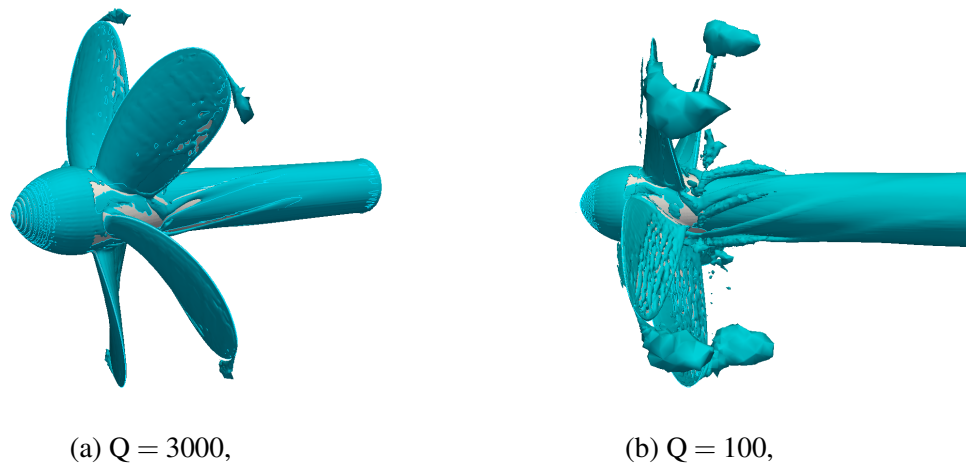
Figure 28: Q-contour for complete propeller simulation in MRF approach.
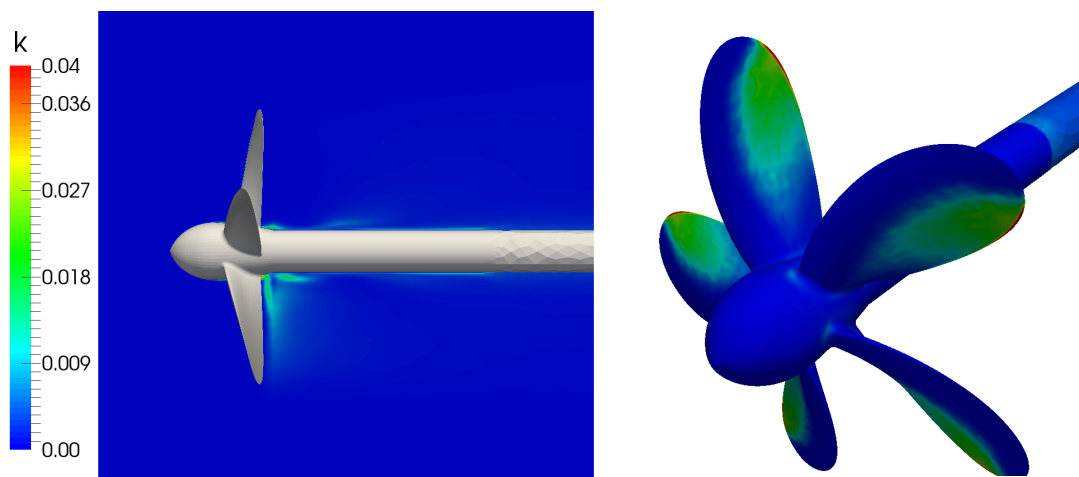


Figure 29: Turbulence kinetic energy (complete propeller simulation), $m^2/s^2$.

## Open water characteristics

Table 13 contains a list of the obtained open water characteristics. The open water diagram for complete propeller simulation is shown in Figure 30. The open water curves are relatively smooth in the whole range, in contrast to the diagram obtained from the single blade simulation.

Table 13: Open water characteristics for complete propeller simulation.

| J | $K_T$ | $10K_Q$ | $\eta_0$, % |
|---|---|---|---|
| **0.10** | 0.3415 | 0.4074 | 13.34 |
| **0.15** | 0.3273 | 0.3957 | 19.75 |
| **0.20** | 0.3111 | 0.3824 | 25.90 |
| **0.25** | 0.2937 | 0.3679 | 31.76 |
| **0.30** | 0.2748 | 0.3521 | 37.27 |
| **0.35** | 0.2550 | 0.3354 | 42.36 |
| **0.40** | 0.2344 | 0.3176 | 46.98 |
| **0.45** | 0.2130 | 0.2992 | 50.98 |
| **0.50** | 0.1907 | 0.2787 | 54.46 |
| **0.55** | 0.1674 | 0.2565 | 57.12 |
| **0.60** | 0.1433 | 0.2326 | 58.82 |
| **0.65** | 0.1179 | 0.2065 | 59.09 |
| **0.70** | 0.0926 | 0.1796 | 57.45 |
| **0.75** | 0.0669 | 0.1514 | 52.72 |
| **0.80** | 0.0393 | 0.1203 | 41.65 |
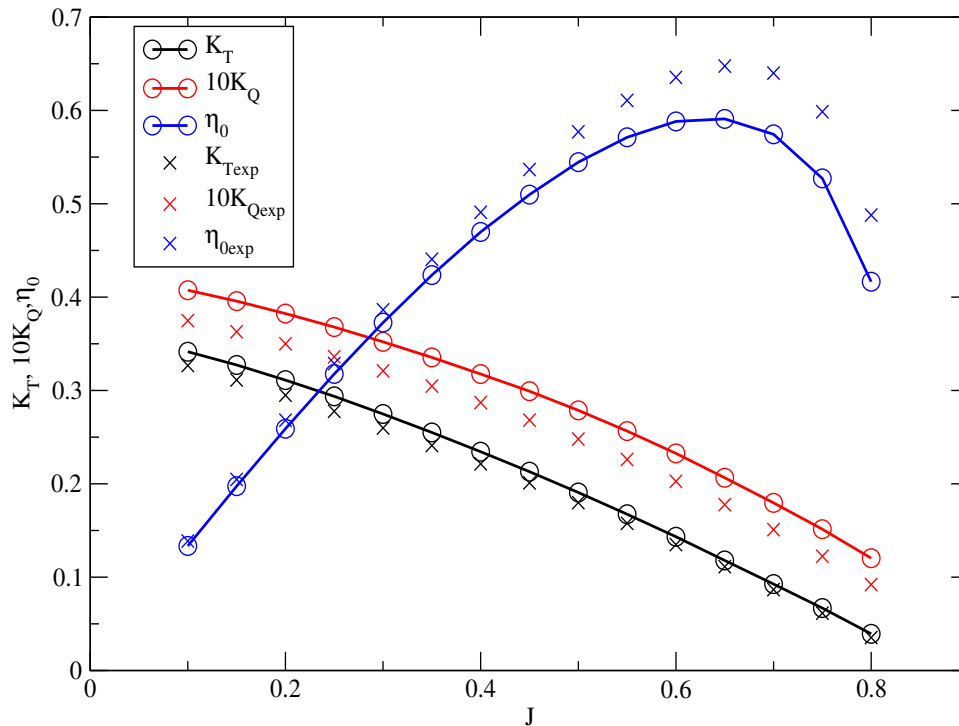
Figure 30: Open water diagram for complete propeller simulation.

From the diagram it is obvious that the error between the simulation results and the experimental data is quite consistent for every operating condition. Although this cannot be seen from the diagram, the thrust and torque coefficients for $J = 0.75$ and $J = 0.80$ have the biggest relative error compared to the experimental results. Since the coefficients values are very low for these operating points, their solution accuracy is very sensitive.

## Convergence curves

In Figure 31 the convergence history of open water coefficients is given. The simulation is run for 2000 iterations after which the convergence is achieved. Observing Figure 32 it can be seen that the same pattern of solution was followed for the last 300 iterations. In contrast to the single blade simulation, in this case the relative deviation of the solution is negligible.
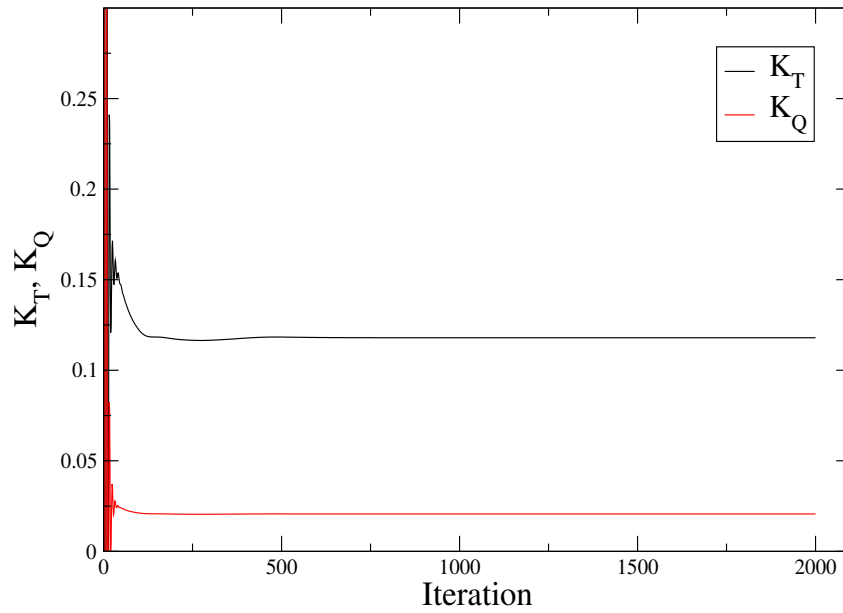
Figure 31: Solution convergence history for propeller simulation in MRF approach.
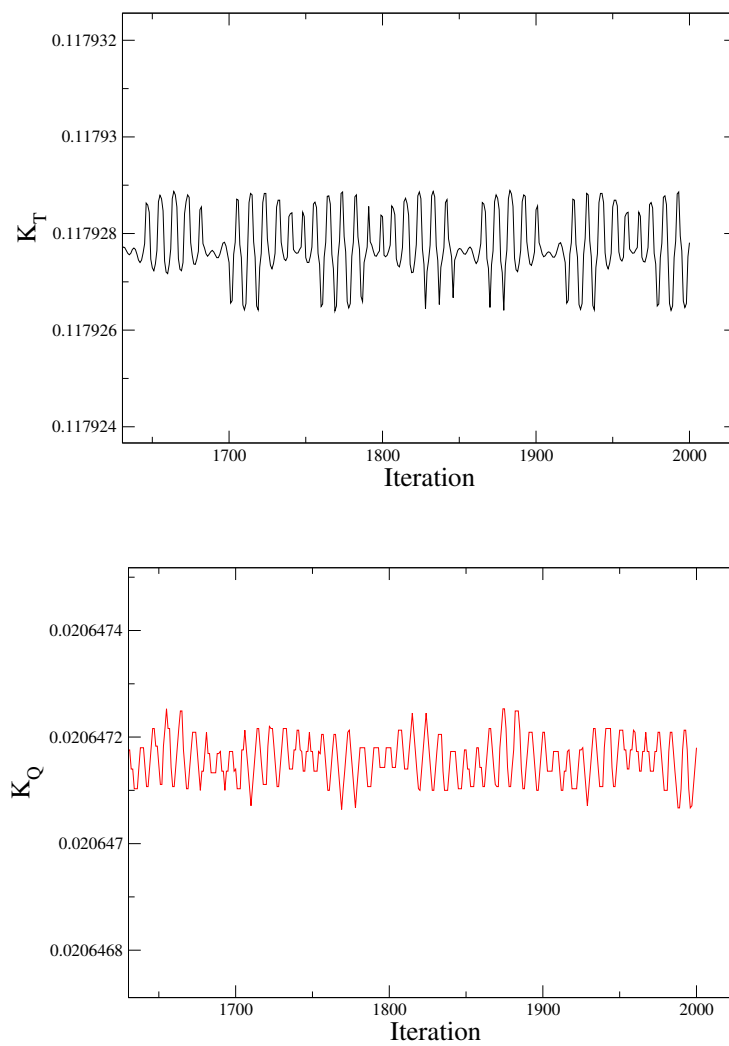


Figure 32: $K_T$ and $K_Q$ convergence curves for propeller simulation in MRF approach.

## 4.5   Transient Simulation for Complete Propeller Mesh

In this subsection the open water test is simulated using the unsteady solver `pimpleDyMFoam` from `foam-extend-3.2`. The solver is based on the `PIMPLE` algorithm which is one of the most used when it comes to solving transient problems. The algorithm first searches for a steady state solution with under-relaxation. After the solution is found, it proceeds in time. To do this, it needs the outer correction loops to ensure the convergence of the explicit parts of the equations. After a defined tolerance criterion within the steady state calculation is achieved, it leaves the outer correction loop and moves on in time. The procedure is done until the end time of simulation is reached [16]. This method is certainly the most accurate of the three approaches, since it solves the governing equations in their standard form without approximations. Because the temporal derivative is included in the equations, this approach is the most demanding in terms of computational resources.

### 4.5.1   Numerical Spatial Domain

The numerical spatial domain used in this simulation is the same one described in subsection 4.4.

### 4.5.2   Simulation Setup

The boundary condition setup for transient simulation is pretty much the same as for the steady state simulation for complete propeller mesh with the exception of the wall boundary conditions on the propeller and the shaft, as shown in Table 14.

Table 14: Velocity and pressure boundary conditions for the transient propeller simulation.

| **Boundary** | **Velocity boundary condition** | **Pressure boundary condition** |
|---|---|---|
| Inlet | Dirichlet | Neumann |
| Outlet | `inletOutlet;`<br>`inletValue uniform (0 0 0);`<br>`value uniform (`$U_x$` 0 0);` | Dirichlet |
| Propeller | `movingWallVelocity;`<br>`uniform (0 0 0);` | Neumann |
| Farfield | Neumann | Dirichlet |
| Shaft | `movingWallVelocity;`<br>`uniform (0 0 0);` | Neumann |

In this simulation turbulence initial values and boundary conditions are specified in the same way as in the two previously explained simulation setups.

To solve the flow in the right way using this transient solver it is necessary to accurately define the rotation properties. The mesh is rotated around the defined axis at the prescribed rotation rate. The entire computational domain is defined as a one rotating cell zone. There are no parts of the domain that are moved relatively with respect to the other, so there is no need to perform any kind of interface modelling.

The Courant number (Co) [16] gives information about how a fluid particles move through the cells and is defined with computational cell size, fluid velocity and the simulation time-step. If Co > 1 the particle move through one or more cells in each time-step, if Co < 1 the particles move only from one cell to another in each time-step. So, when running transient simulations it is desirable to keep the Courant number as low as possible (ideally around Co = 1). The conflicting criterion is the computational time, since the Courant number increases with an increasing time-step. This is why the time-step should be defined so that the simulation can be performed correctly within a reasonable time. Using a solver based on a previously explained `PIMPLE` algorithm allows larger Courant numbers in simulations, which means that the time step can be increased [16]. The time step in this simulation is defined to be equal to the time in which the propeller makes a 1° revolution. It means that $\Delta t$ is expressed as:

$$\Delta t = \frac{1}{360\,n} \approx 0.0003101 \text{ s},\qquad(38)$$

where $n$ represents the propeller revolutions per second.

In the transient simulation the same linear solvers are used as in the MRF simulations. The linear solver setup is given in Table 15. The pressure and velocity labeled with pFinal and UFinal correspond to the solution in the outer correction loop of the PIMPLE algorithm. The only difference regarding the solution control are the under-relaxation factors, the values of which are listed in Table 16.

Table 15: Linear solver settings for the transient simulation.

| Variable | Linear solver | Tolerance | Relative tolerance |
|---|---|---|---|
| p | `amgSolver (PAMG)` | 1e-07 | 0.01 |
| pFinal | `amgSolver (PAMG)` | 1e-07 | 0 |
| U | `BiCGStab (DILU)` | 1e-07 | 0 |
| $\omega$ | `BiCGStab (DILU)` | 1e-07 | 0 |
| k | `BiCGStab (DILU)` | 1e-07 | 0 |

Table 16: Solution under-relaxation for the transient simulation.

| Variable | Relaxation factors |
|:--------:|:------------------:|
| p | 1 |
| pFinal | 1 |
| U | 1 |
| UFinal | 1 |
| $\omega$ | 0.5 |
| k | 0.5 |

### 4.5.3 Simulation Results

The entire range of operating conditions is simulated with the two foregoing methods. The transient simulation is much more time consuming and so it is run only for $J= 0.65$ operating point. Since the actual propeller rotation is performed in the simulation, the obtained results are assumed to be the most accurate. Therefore, the following representations of flow fields are considered as more relevant than the ones obtained with steady state simulations. In subfigure 33a the pressure field around the propeller is shown. Arrows in subfigure 33b show how the fluid attacks the boss cap and blades of the propeller. The arrows are coloured by the axial velocity to inlet velocity ratio (Ux/Ui). The green colour of the arrows attacking the boss cap indicates that the fluid velocity in this area is lower than in the mean flow.



(a) Pressure distribution,        (b) Velocity vectors in the pressure field,
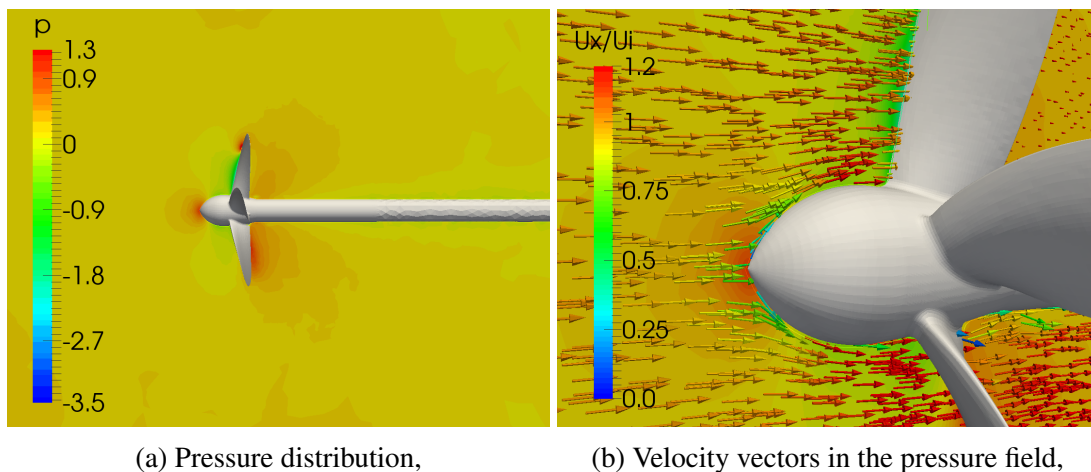
Figure 33: Pressure field (transient simulation), $\text{m}^2/\text{s}^2$.

The pressure distribution over the suction and the pressure side of the propeller is presented in Figure 34. The leading edge of the suction side area has the same pressure distribution as in the Detail 1 of Figure 26a. The leading edge area of the suction side has the highest pressure value, while on the leading edge area of the pressure side the pressure is much lower. The difference between the pressure values causes the highest acceleration in that area and accordingly the highest fluid velocity.

(a) Suction side,                                        (b) Pressure side,
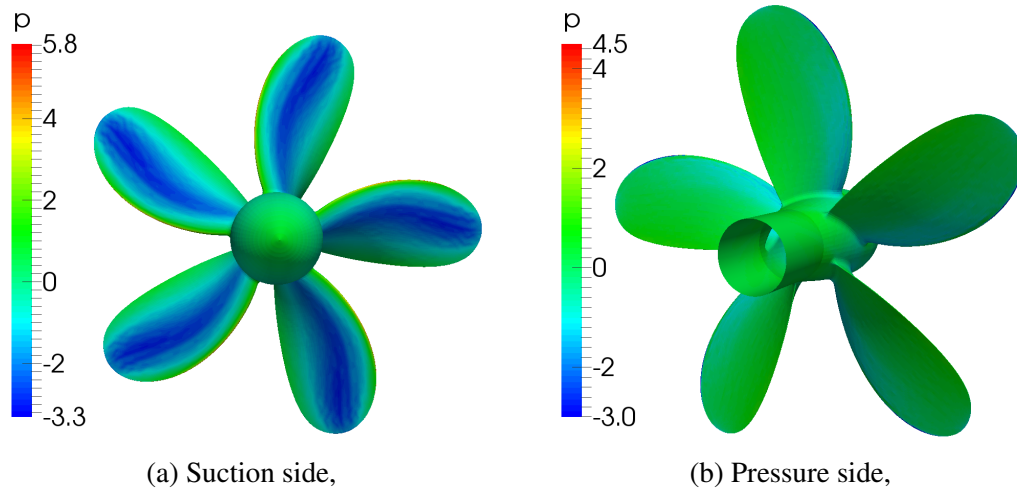
Figure 34: Pressure distribution over the blades for transient simulation, $m^2/s^2$.

Figure 35 presents the axial velocity distribution over the y=const. plane coloured by the ratio of the axial and the inlet velocity ($U_x/U_i$). The colouring indicates higher axial velocity values in the propeller wake.
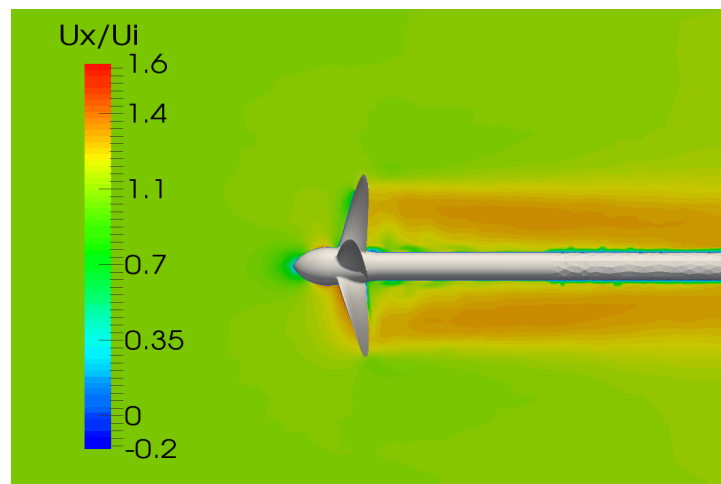


Figure 35: Axial velocity for transient simulation.

Figure 36 shows the projection of velocity vectors in the plane $x = 0.2R_P$ behind the propeller coloured by the magnitude of the velocity components in the y and z direction. $R_P$ represents the propeller radius.
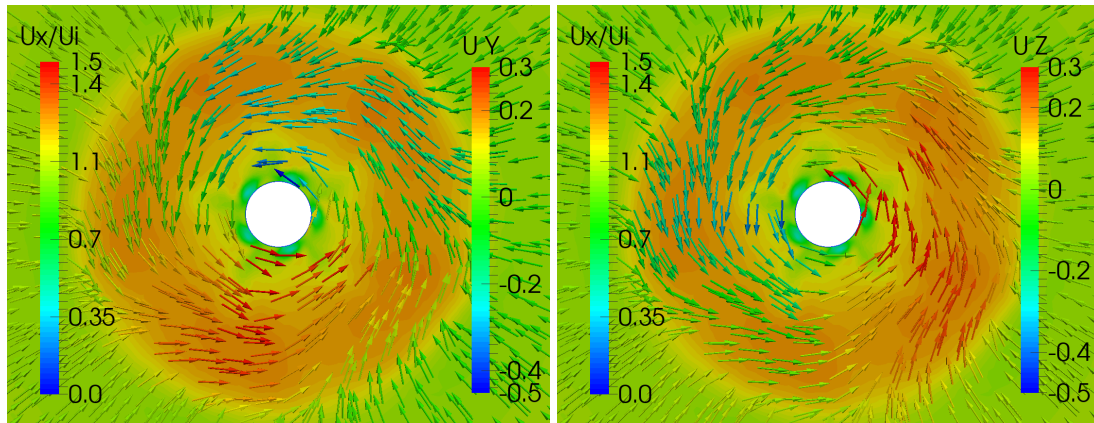
(a) Coloured by $U_y$,                                      (b) Coloured by $U_z$,

Figure 36: Velocity vectors projected on the x $= 0.2R_P$ plane.

Figure 36 also shows the area of propeller induced axial velocity. In the region of higher axial velocity the projection of the velocity vectors indicates the swirling motion of the fluid.

The vorticity in the propeller area for transient simulation is examined by the Q-criterion and introduced by Figure 37 and Figure 38. Q is set to the same values as in the previous representations. The structure of vortices is almost identical to those shown in the above sections. This comparison also adds to the significance of the simulation of unsteady flows with the application of steady state approximations.
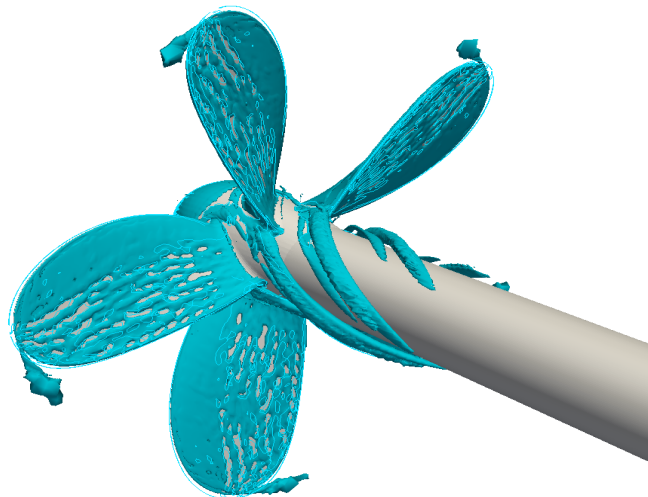


Figure 37: Vortices matching Q $= 3000$ criterion for the transient simulation.
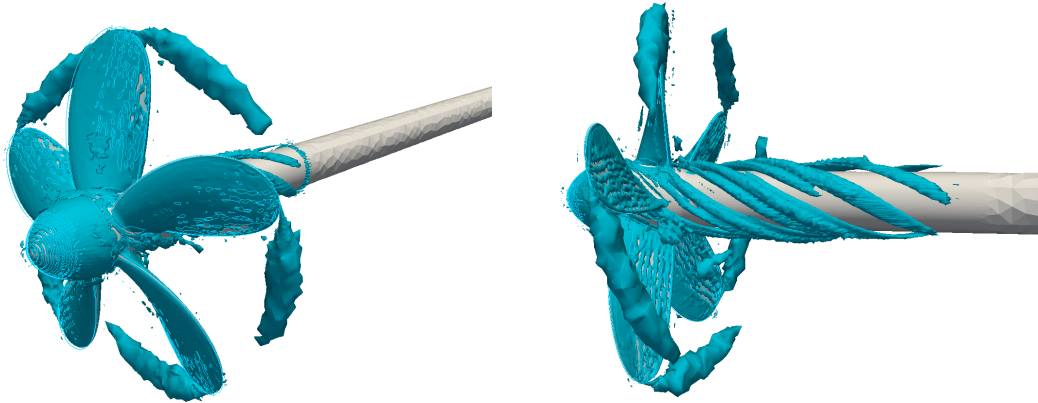
Figure 38: Vortices matching Q = 100 criterion for the transient simulation.

Figure 39 shows the turbulence kinetic energy. Higher turbulence occurs in the trailing edge area and in the upstream direction just behind the root of the blades. These are the regions where the velocity component with the direction of mean flow is not dominant, as is shown in the details of Figure 39. The vectors are coloured by the $U_x/U_i$ ratio. Hence, it can be seen that in high turbulence areas there are vectors with diverse directions and lower $U_x/U_i$ ratio than in the mean flow. Comparison of the representation of turbulence kinetic energy and the structure of vortices presented in Figure 37 points out the matching between the locations with high turbulence and areas in which vortices with higher energy occur. This is particularly apparent on the part of the shaft near the propeller.
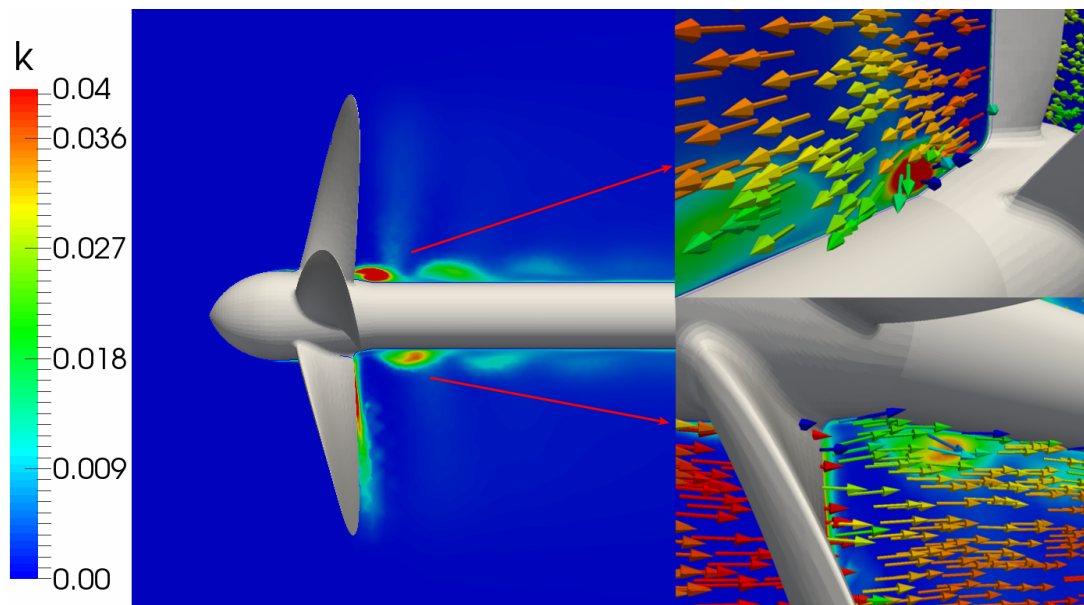


Figure 39: Turbulent kinetic energy for the transient simulation, $m^2/s^2$.

## Open water characteristics

As mentioned previously the transient simulation is performed only for $J = 0.65$ operating point. The obtained open water characteristics have the following values:

- $K_T = 0.11247$,

- $K_Q = 0.18891$,

- $\eta_0 = 61.59$ %.

## Convergence curves

In the transient simulation, 1 second of real time (8.935 propeller revolutions) is simulated. The time step of the simulation is calculated with the expression in Eq.38., meaning that the simulation is run for approximately 3200 iterations. The average Courant number in the 3200th iteration is Co $\approx 0.2$, while its maximum value is Co $\approx 26.5$. The maximum is located at the tip of the blades because in that area the mesh is the most refined, while the velocity has the highest value. Considering the values of obtained open water coefficients it can be concluded that the high Courant numbers did not significantly affect the simulation accuracy. Figure 40 shows a graph of open water characteristics as a function of time for the $J = 0.65$ operating point. Closer observation of Figure 41 reveals seemingly rough convergence. The maximum relative deviation of $K_T$ is 0.6% and for $K_Q$ it is 0.2%. Considering that for the last 0.2s ( 600 iterations) the solution does not change significantly, it can be concluded that convergence is achieved.
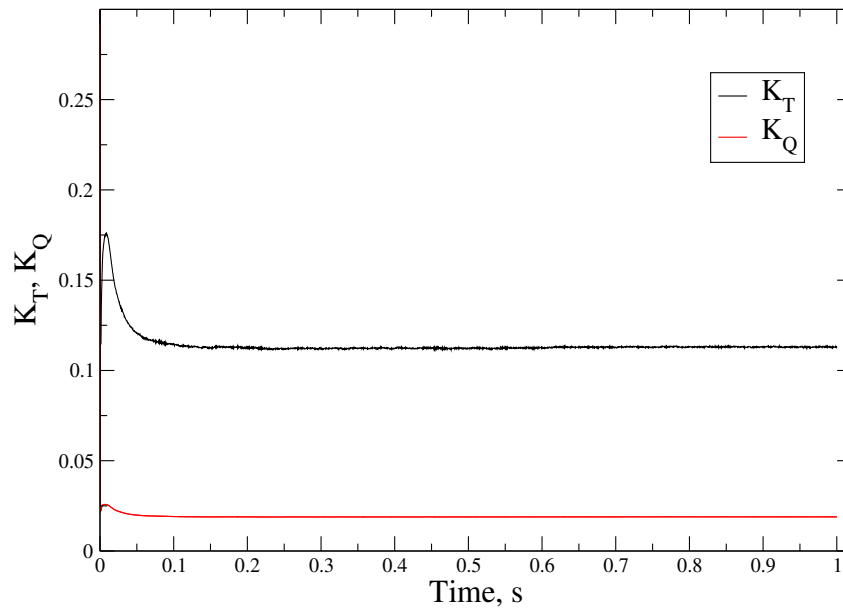
Figure 40: Solution convergence history for the transient simulation.
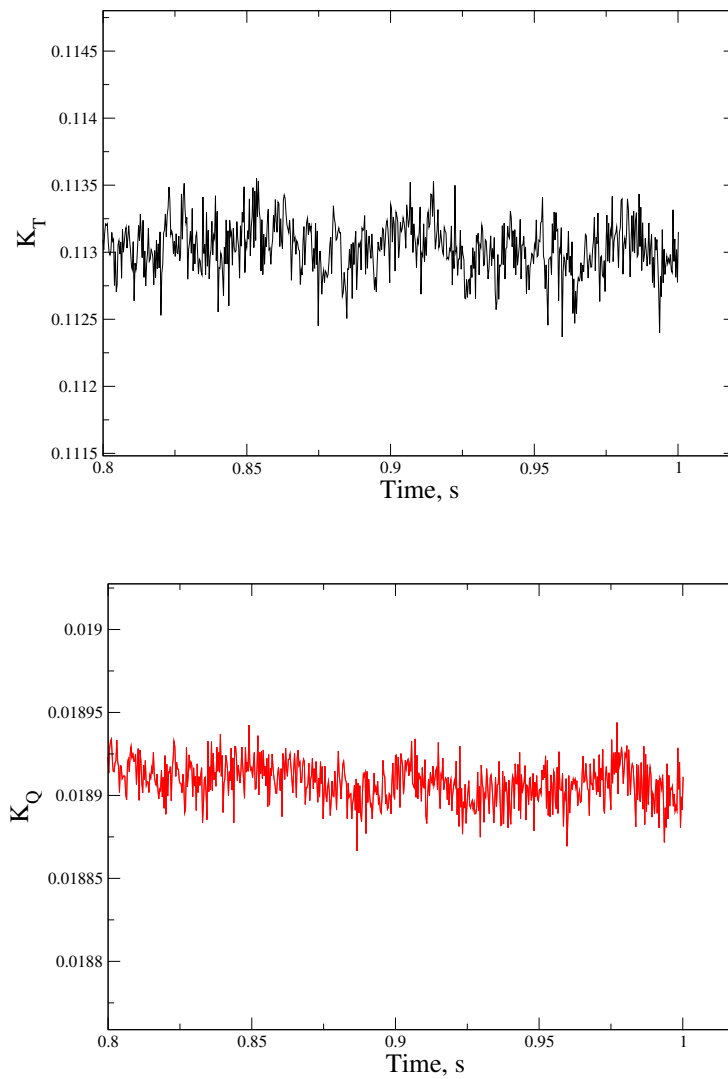


Figure 41: $K_T$ and $K_Q$ convergence curves for the transient simulation.

## 4.6 Comparison of Results of Applied Approaches

### 4.6.1 Accuracy Comparison

The accuracy of the three approaches is evaluated by comparison of the open water characteristics obtained by simulation and the results of the experiment. For both of the steady state approaches the accuracy is analyzed on the entire open water diagram, while the transient simulation is evaluated only for $J = 0.65$. The characteristics obtained with complete propeller simulations are labeled with $C$ in the subscript, and coefficients obtained with single blade simulation are labeled with $S$.
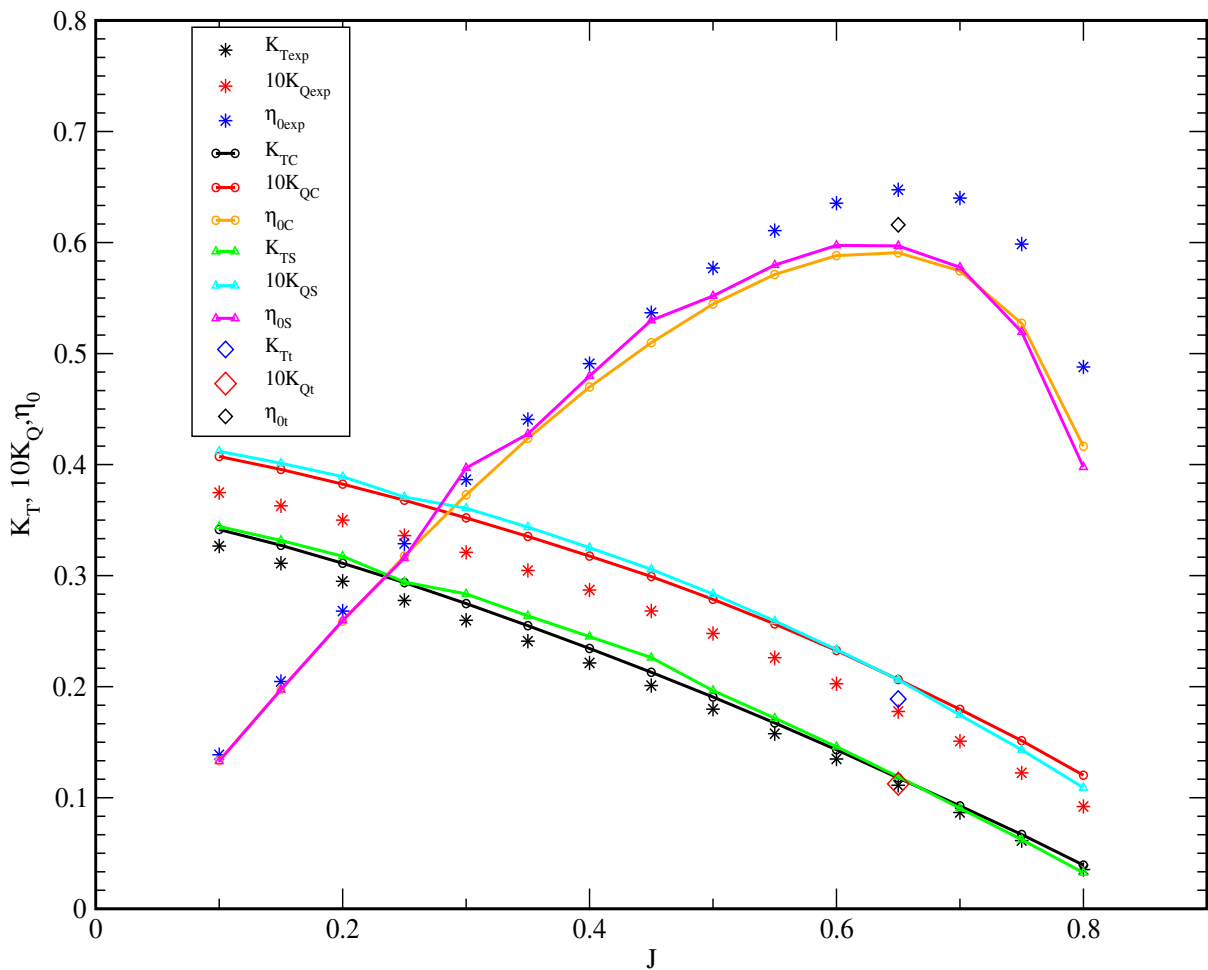


Figure 42: Open water characteristics comparison.

The open water curves obtained by the complete propeller simulation with MRF show consistent error in the whole range. The exceptions are the last three operating points, where the gap between the experimental data and simulation results increases. From the diagram it can be seen how for $J = 0.65$ the transient simulation gives the most accurate results for both, thrust and torque coefficients.

To better present the differences between the simulation results, a diagram with errors for every

operating point is shown in Figure 43. The error is calculated with the expression:

$$Err = \frac{K_{simulation} - K_{experiment}}{K_{simulation}} \times 100\%,$$ (39)

where K is either the thrust or the torque coefficient, while the subscript indicates how the coefficient is obtained (*S* is for one blade simulation, *C* is for complete propeller simulation). A negative value of error indicates that the coefficient value obtained from the simulation is lower than the coefficient value calculated from the experimental data. A positive error indicates the opposite.
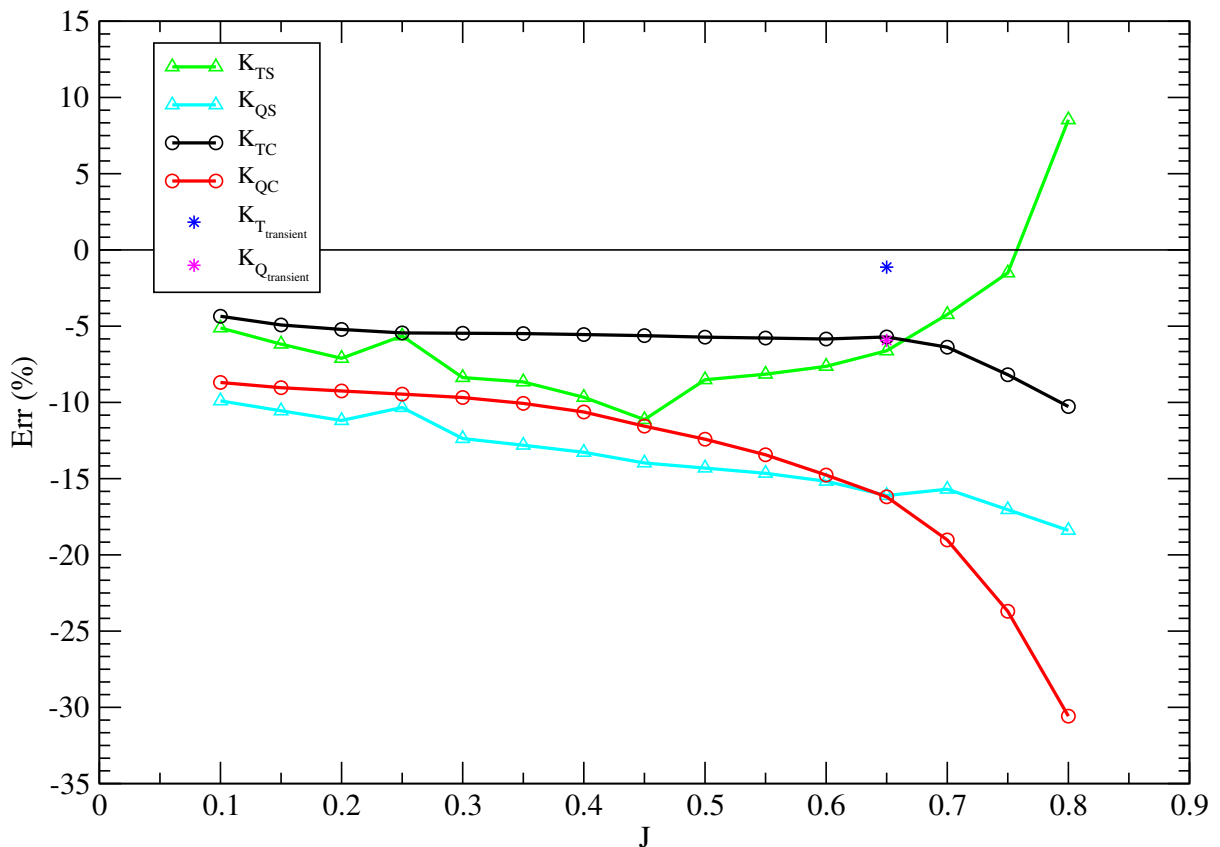


Figure 43: Error comparison.

The error of thrust and torque coefficients calculated with complete propeller simulations are slightly changing until the $J = 0.70$ operating point. This is particularly true for the thrust coefficient. $K_T$ error is approximately 5% for all testing points in the range $J = 0.1 - 0.65$ and then increases to the maximum value of 10.27% for $J = 0.80$. The errors of torque coefficients obtained from the complete propeller simulations are relatively large for the whole range of advance coefficients. The error increases slightly from 8.69% for $J = 0.1$ to 16.19% for $J = 0.65$. After that point there is a significant increase in error up until the unacceptable 30.57% for $J = 0.80$. The open water characteristics obtained with the single blade passage simulation are less accurate for the majority of operating points. Interestingly, for advance

coefficients greater than $J = 0.65$ the trend of an error of the single blade passage simulation is changed and so the results are more accurate than the results from complete propeller simulation. The transient simulation proved to be most accurate with the errors of $K_T$ and $K_Q$ being 1.13% and 5.93% for $J = 0.65$.

### 4.6.2 Computational Costs Comparison

The computational costs comparison between approaches is evaluated for $J = 0.65$ operating point and shown in Table 17, where *CPU* denotes the computational resources, $i$ is the number of iterations in simulation and $t$ is the computational time. All the simulations were run on the same computer so the results can be consistently compared. The computational time of each simulation is reduced to the average time required to perform one iteration and shown in the last column.

Table 17: Computational cost comparison.

| Approach | CPU | i | t, min | t/i, s |
|----------|-----|---|--------|--------|
| **Single blade** | i5, 3.20GHz, 4 cores | 2500 | 201 | 4.82 |
| **Full propeller with MRF** | i5, 3.20GHz, 4 cores | 2000 | 513 | 15.415 |
| **Transient** | i5, 3.20GHz, 4 cores | 3200 | 2498 | 46.85 |

It can be seen that for the same numerical grid the solving of one iteration of transient simulation lasts approximately three times longer than solving it in the MRF simulation. The solution history of applied steady state simulations is shown in Figure 44. The solution is given as a function of a computational time. The convergence curves of a complete propeller simulation are labeled with the addition of $C$ in the subscript, and the ones from a single blade simulation are labeled with $S$. It can be seen that the solution convergence of both simulations occurs in a close time points. As mentioned previously, the single blade simulation solves with a greater error.
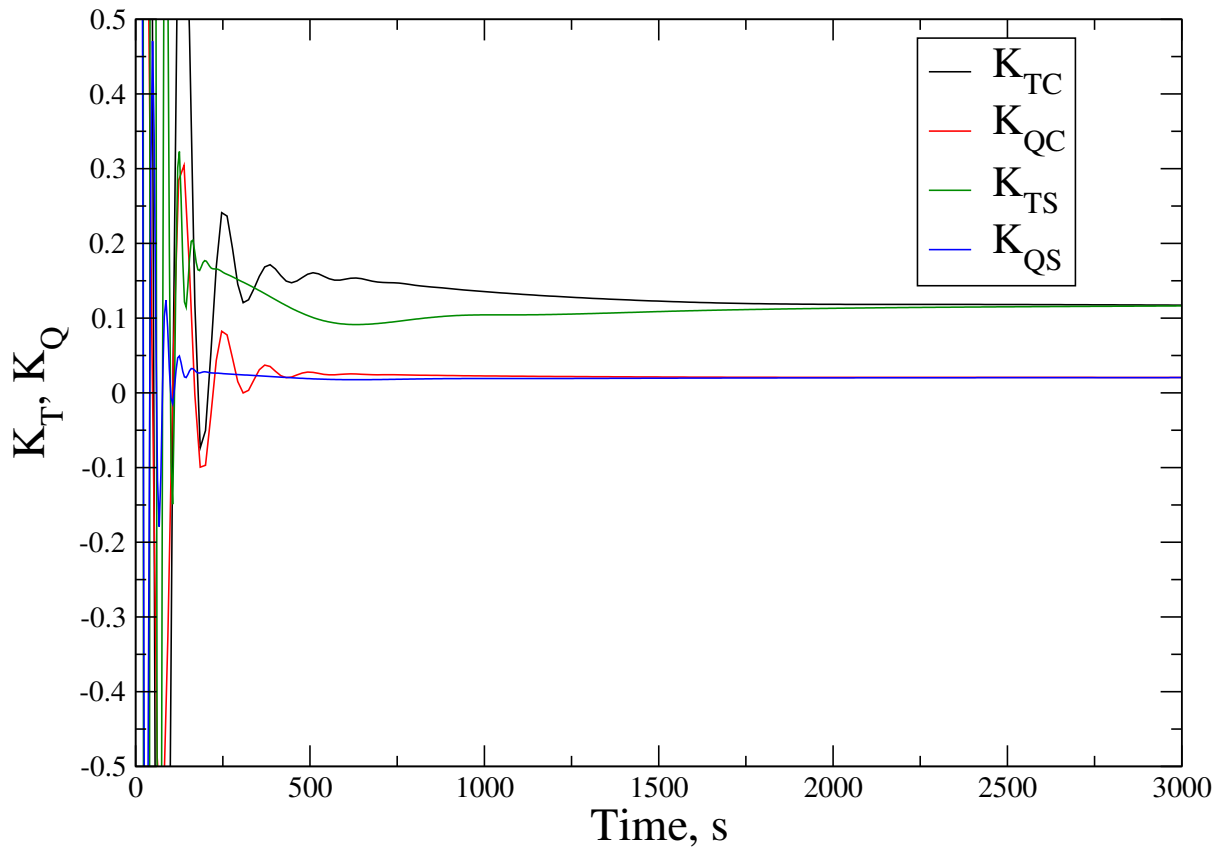
Figure 44: Solution/Computational time graph.

Single blade simulation significantly reduces computational time, but at the same time it is the least reliable method when it comes to accuracy. Although less accurate, the setup with periodic boundaries still provides a physical solution. If the error is in an acceptable range, it can serve as a rough approximation when computational resources are limited. Transient simulation is, however, the most demanding with reference to computational time, but produces the most accurate results.

## 4.7   Closure

The results of open water test simulations can further be used to model the propeller using an actuator disc. Since the information about the propeller influence on the flow is known from simulations, the actuator disc model can be tuned so that the flow behaves similarly to the flow around the actual propeller. In the next section the actuator disc model is explained and the performed simulation results are shown.

# 5  Propeller Modelling

For some purposes in naval hydrodynamics CFD it is more important to account for the force which the propeller exerts on the naval object, while the details of the wake are not as important. In these cases a model of the propeller can be used to save computational time, where the propeller characteristics have to be known in advance. It is desirable that the wake pattern is as similar as possible to the wake of the actual propeller, in order to correctly account for the wake-ship interaction.

This section represents propeller modelling using a simplified actuator disc instead of actual geometry. The presented method is used to lower the computational costs of transient simulations in which the interaction between the propeller and the hull is of interest. In the first subsection the theoretical background and geometrical definition of an actuator disc is given. The second one describes the whole simulation procedure, from mesh generation to simulation setup and postprocessing. In the third subsection a comparison of results with actual geometry simulation results is given.

## 5.1  Actuator Disc Model

### 5.1.1  Actuator Disc Theory

As already stated, solving the flow around the exact propeller geometry and its interaction with a ship hull can be expensive in terms of computational time. As an alternative it is preferred to define an actuator disc region at the location of the propeller at which the momentum transferred from the exact propeller to the fluid is modelled. There is no propeller geometry in the numerical spatial domain when performing a simulation using this method. Thus, there is no fine spatial discretisation of the domain due to the intricate propeller geometry, and simpler meshes can be used. Also, temporal resolution can be considerably coarser. As a consequence mesh generation time and simulation time are lowered, while acceptable result accuracy is achieved.

In this approach at the location of the propeller the disc is modelled to simulate the propeller behaviour. The model is based on the assumption of a thin infinite-bladed propeller model. The disc is actually a cylindrical interface with the same diameter as the modelled propeller [17]. To mimic thrust and torque induced by the propeller, specific boundary conditions for pressure and velocity are written. The pressure boundary condition is defined to produce the desired pressure jump, while the boundary condition of velocity is set to add a swirl. Besides meeting the integral values of thrust and torque, the distribution of pressure and tangential velocity over the disc has to be appropriately specified in order to accurately match the behaviour of the flow behind the propeller. The derivation of the expressions for the pressure and tangential velocity

jump is based on the volume force model given in [18]. Total thrust is expressed as an integral of the pressure jump $\Delta p$ over the disc surface:

$$T = \int_S \Delta p \, dS, \tag{40}$$

where S is the surface of the disc. The disc is geometrically defined with its inner and outer radius. If $R_H$ is the inner radius (also the radius of the hub) and $R_p$ is the outer radius of the disc the above expression takes the following form:

$$T = \int_{R_H}^{R_P} \int_0^{2\pi} \Delta p \, d\theta \, r \, dr = \int_{R_H}^{R_P} \Delta p \, 2\pi \, r dr. \tag{41}$$

Taking into account the Goldstein distribution [19], the pressure jump can be expressed as:

$$\Delta p = A_x r^* \sqrt{1 - r^*}, \tag{42}$$

where $r^*$ is a normalized disc radius defined as:

$$r^* = \frac{r' - r'_h}{1 - r'_h}, \tag{43}$$

where $r' = \frac{r}{R_P}$ and $r'_h = \frac{R_h}{R_P}$. Derivation of $r^*$ over $r$ reads:

$$\frac{dr^*}{dr} = \frac{1}{R_P - R_H} \Rightarrow dr = (R_P - R_H)dr^* \Rightarrow r = R_H + r^*(R_P - R_H). \tag{44}$$

By substituting $\Delta p$ from Eq. (41). with Eq. (42). and changing the variable of integration from $r$ to $r^*$ the following expression for thrust is derived:

$$\begin{aligned}
T &= \int_{r=R_H}^{r=Rp} A_x r^* \sqrt{1 - r^*} \, 2\pi r \, dr = \int_{r=R_H}^{r=Rp} A_x r^* \sqrt{1 - r^*} \, 2\pi r (R_P - R_H) \, dr^* \\
&\{r = R_P \Rightarrow r^* = 1, r = R_H \Rightarrow r^* = 0\} = \\
&= 2\pi(R_P - R_H) \int_0^1 A_x \, r^* \sqrt{1 - r^*} (R_H + r^*(R_P - R_H)) \, dr^* = \\
&= 2\pi(R_P - R_H)A_x \left[ R_H \int_0^1 r^* \sqrt{1 - r^*} dr^* + (R_P - R_H) \int_0^1 r^{*2} \sqrt{1 - r^*} dr^* \right].
\end{aligned} \tag{45}$$

The integrals in square brackets can be evaluated as:

$$\int_0^1 r^* \sqrt{1 - r^*} dr^* = \frac{4}{15}, \tag{46}$$

$$\int_0^1 r^{*2}\sqrt{1-r^*}\,dr^* = \frac{16}{105}, \tag{47}$$

and their values can be inserted into Eq. (45). to derive the final expression for thrust:

$$T = 2\pi(R_P - R_H)\,A_x\frac{4}{105}\,(3R_H + 4R_P). \tag{48}$$

Constant $A_x$ then reads:

$$A_x = \frac{105}{8}\frac{T}{\pi(R_P - R_H)(3R_H + 4R_P)}. \tag{49}$$

The total torque is expressed by the following form:

$$Q = \int_V r\frac{\Delta u_t}{\Delta t}\rho\,dV, \tag{50}$$

where $u_t$ is the tangential velocity and $V$ is the volume on which the torque is acting. Rearranging Eq. (50). to be expressed with the integral over surface the torque can be written as:

$$Q = \int_S r\frac{\Delta u_t}{\Delta t}\rho\,u_x\,\Delta t\,dS = \int_{r=R_H}^{r=R_P} r\,du_t\rho\,u_x\,2\pi r dr, \tag{51}$$

where $u_x$ is the axial velocity. Following the Goldstein distribution the change of tangential velocity can be written as:

$$\Delta u_t = A_\theta \frac{r^*\sqrt{1-r^*}}{r^*(1-r^*)+r'_h}. \tag{52}$$

By inserting $\Delta u_t$ from Eq. (52). into Eq. (51). and changing the variable of integration the torque is expressed as:

$$\begin{aligned}
Q &= \int_{r=R_H}^{r=R_P} r\,A_\theta\frac{r^*\sqrt{1-r^*}}{r^*(1-r^*)+r'_h}\rho\,u_x\,2\pi r dr = \\
&= A_\theta 2\pi\,u_x\,\rho\int_0^1 (R_H + r^*\,(R_P - R_H))^2\frac{r^*\sqrt{1-r^*}}{r^*(1-r'_h)+r'_h}(R_P - R_H)\,dr^* = \\
&= A_\theta 2\pi\,u_x\,\rho\int_0^1 \left[R_P\,(r'_h + r^*\,(1-r'_h))\right]^2\frac{r^*\sqrt{1-r^*}}{r^*(1-r'_h)+r'_h}R_P\,(1-r'_h)dr^* = \\
&= A_\theta 2\pi\,u_x\,\rho\,R_P^3\int_0^1 (r'_h + r^*\,(1-r'_h))\,r^*\sqrt{1-r^*}\,(1-r'_h)\,dr^* = \\
&= A_\theta 2\pi\,u_x\,\rho\,R_P^3\,(1-r'_h)\left[r'_h\int_0^1 r^*\sqrt{1-r^*}\,dr^* + (1-r'_h)\int_0^1 r^{*2}\sqrt{1-r^*}\,dr^*\right].
\end{aligned} \tag{53}$$

Inserting the values of integrals from Eq. (46). and Eq. (47). the torque is written as:

$$Q = A_\theta 2\pi \, u_x \, \rho \, R_P (R_P - R_H) \, \frac{4}{105} \, (3R_H + 4R_P). \tag{54}$$

$A_\theta$ is now:

$$A_\theta = \frac{105}{8} \frac{1}{\rho} \frac{Q}{\pi \, u_x \, R_P (R_P - R_H)(3R_H + 4R_P)}. \tag{55}$$

With $A_x$ and $A_\theta$ being derived, the form in which pressure jump and tangential velocity are implemented in the boundary conditions code is fully defined.

The derivation of pressure jump and the tangential velocity expressions is performed similarly as the derivation of the volume force model introduced in [18]. By implementing the boundary conditions with derived distributions the pressure and the tangential velocity over the actuator disc have the same distributions as the volume forces. Figure 45 shows the axial and radial force distribution as a function of normalized radius.



(a) Axial force,          (b) Radial force,
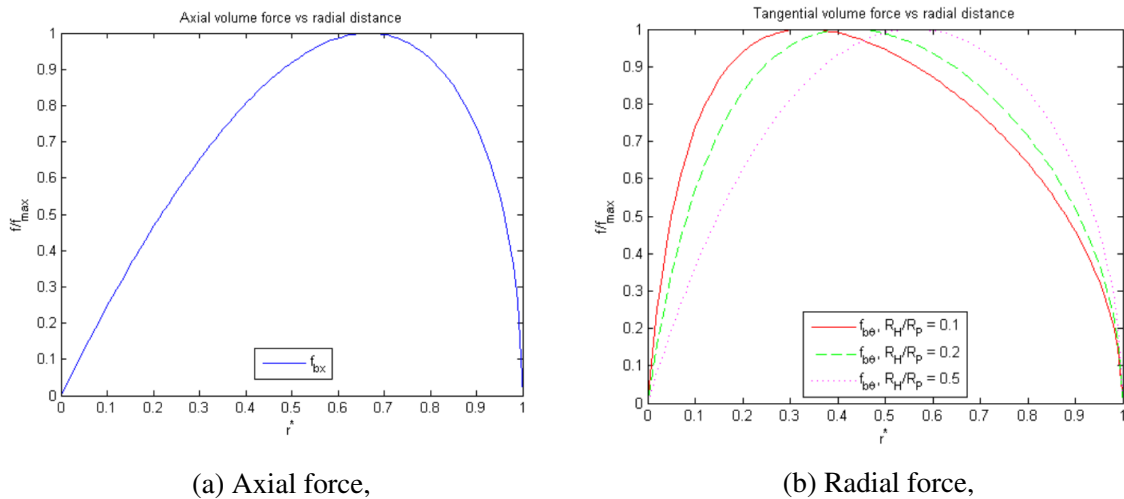
Figure 45: Normalized forces versus normalized radius [18].

## 5.2   Actuator Disc Simulation

### 5.2.1   Numerical Spatial Domain

The main obstacle when computing the flow around the ship propeller is the complexity of the mesh generation process due to the intricate propeller blades. A big advantage of using the propeller model over the actual geometry is the fact that the mesh generation is incomparably easier because the complicated meshing near geometry is avoided. For this model a domain of the same size as for actual geometry simulation is used, meaning that the outlet of the domain is at a distance 20D downstream of the actuator disc, the inlet is at 4D upstream and the radius of the domain is approximately 5D. The spatial domain with the actuator disc at the location of the propeller is shown in Figure 46. The grid used for the model is fully structured.
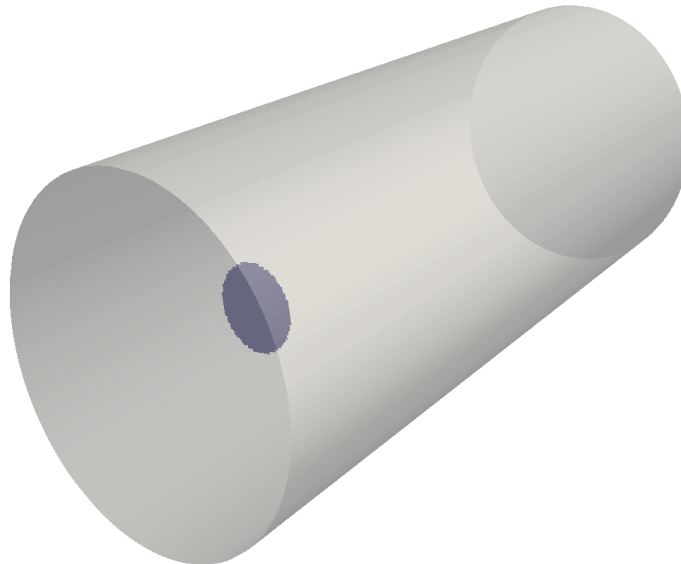
Figure 46: Numerical spatial domain of the actuator disc simulation.

By using `foam-extend` tools the desired cell faces are collected from the mesh to form the actuator disc region. Collected internal faces are afterwards transformed into boundary faces so that the boundary conditions on the disc can be applied.

The mesh consists of 866 970 hexahedral cells. The quality indicator values are listed in Table 18. Just by looking at the quality parameters it is obvious how the generation of the appropriate grid does not represent a major problem.

Table 18: Cell quality of an actuator disc mesh.

|                      | Average | Maximum | Threshold |
|----------------------|---------|---------|-----------|
| **Aspect ratio**     | -       | 9.551   | -         |
| **Skewness**         | -       | 0.3733  | 4         |
| **Non-orthogonality**| 5.898   | 26.218  | 70        |

### 5.2.2  Simulation Setup

Since the unsteady flow with the rotation is simulated, the simulation is performed with a transient solver. The difference between this solver and the solver from the transient propeller simulation is that in this case the rotating parts of the domain are not defined. The rotation in the flow is simulated just by using the boundary conditions described above.

The boundary condition setup is very similar to the setups of actual geometry simulations. The pressure on the outlet is defined with the `outletInlet` boundary condition. It switches between Neumann and Dirichlet boundary conditions depending on the flux value on the boundary. If the flux is positive, meaning that its direction points out of the domain, the Dirichlet boundary condition is applied. If opposite, the Neumann boundary condition is used. A remarkable difference in comparison to previous simulations is the definition of new boundary conditions on the internal boundary (actuator disc area) in the mesh. The boundary condition setup of pressure and velocity is presented in Table 19.

Table 19: Velocity and pressure boundary conditions for the actuator disc simulation.

| **Boundary**   | **Velocity boundary condition**                                                                 | **Pressure boundary condition**                                                                 |
|----------------|-------------------------------------------------------------------------------------------------|-------------------------------------------------------------------------------------------------|
| Inlet          | Dirichlet                                                                                       | Neumann                                                                                          |
| Outlet         | `inletOutlet;` <br> `inletValue uniform (0 0 0);` <br> `value uniform ($U_x$ 0 0);`             | `outletInlet;` <br> `outletValue uniform (0 0 0);` <br> `value uniform ($U_x$ 0 0);`            |
| Actuatordisc   | `propellerVelocity;`                                                                            | `propellerPressure;`                                                                            |
| Farfield       | Neumann                                                                                         | Neumann                                                                                          |

As explained, the purpose of the pressure boundary condition is to cause the desired distribution of pressure jump over the disc and at the same time to match the total thrust of the propeller. The velocity boundary condition is defined in order to give the distribution of tangential velocity, while satisfying the total torque. In that way the swirling motion of the fluid behind the propeller is modelled. The pressure boundary condition is defined in a source code to carry out the following actions:

1. Read the inflow velocity on the disc and calculate the advance coefficient J,

2. Based on calculated J find the corresponding thrust coefficient $K_T$,

3. Calculate the thrust value which is to be added over the disc by using Eq. (29).,

4. Calculate the related pressure jump using Eq. (42).

Since the expressions for the theoretical pressure distribution are derived as dependant on a normalized radius it is necessary to define the particular hub ($R_H$) and disc propeller radius ($R_P$) for the pressure boundary condition.

The velocity boundary condition is implemented following a similar procedure. As in the pressure boundary condition, $R_H$ and $R_P$ need to be defined for the velocity boundary condition as well. The distribution of tangential velocity is calculated performing the steps as follows:

1. Read the inflow velocity on the disc and calculate J,

2. For calculated J find the related torque coefficient $K_q$,

3. Calculate the torque using Eq. (30).,

4. Calculate the distribution using the obtained torque in Eq. (55).,

5. Calculate the tangential vectors of velocity,

6. Set the vectors of tangential velocity over the disc to follow the computed distribution.

The turbulence values on the boundaries are defined in the same way as in the actual geometry simulation with the exception that in this case there is no near wall treatment. The turbulence properties are defined only on the outer boundaries of the domain, while the `cyclic` boundary condition is set at the disc.

The solution and algorithm control differs in comparison to previous simulations. The pressure linear solver is changed from `amgSolver` (PAMG) to `BiCGStab` with DILU preconditioner and different tolerance values are set. Table 20. shows the linear solvers setup for this case. The under-relaxation is set with the same factors as in the transient simulation of propeller geometry as shown in Table 21.

Table 20: Linear solver settings for propeller model simulation.

| Variable | Linear solver | Tolerance | Relative tolerance |
|----------|---------------|-----------|--------------------|
| p | BiCGStab (DILU) | 1e-08 | 0 |
| pFinal | BiCGStab (DILU) | 1e-09 | 0 |
| U | BiCGStab (DILU) | 1e-08 | 0.01 |
| UFinal | BiCGStab (DILU) | 1e-09 | 0 |
| $\omega$ | BiCGStab (DILU) | 1e-07 | 0 |
| k | BiCGStab (DILU) | 1e-07 | 0 |

Table 21: Solution under-relaxation for propeller model simulation.

| Variable | Relaxation factors |
|----------|--------------------|
| p | 1 |
| pFinal | 1 |
| U | 1 |
| UFinal | 1 |
| $\omega$ | 0.5 |
| k | 0.5 |

### 5.2.3 Simulation Results

In this subsection the actuator disc influence on the fluid flow is shown. As the behaviour of the fluid behind the actuator disc is of interest, the results are represented in the form of the axial and tangential velocities over and behind the actuator disc. Running the simulation with the boundary conditions described above, the axial and tangential velocity over the actuator disc assume the following distributions.



(a) Axial velocity over the actuator disc,

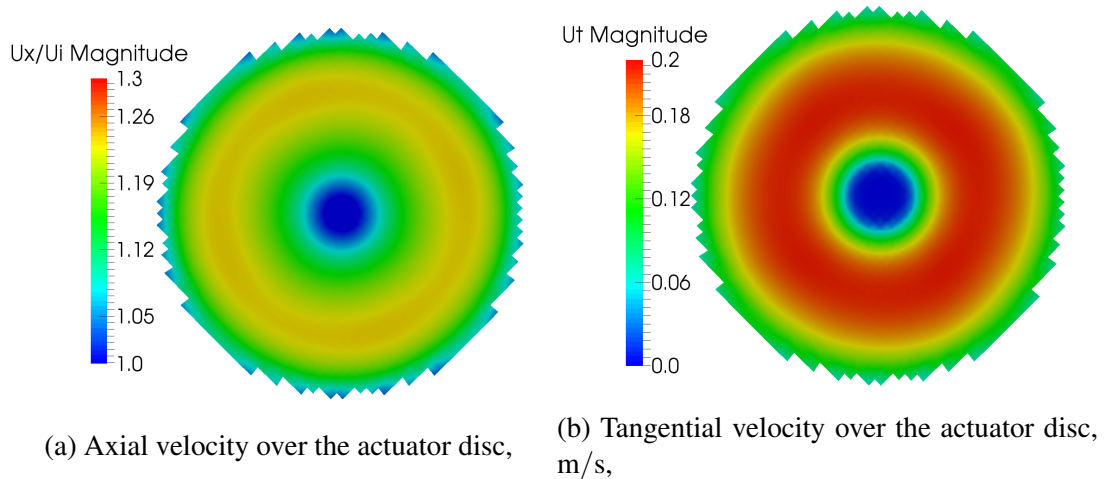(b) Tangential velocity over the actuator disc, m/s,

Figure 47: Velocity components over the actuator disc.

From Figure 47a it is obvious that the pressure jump causes the desired distribution over the disc. The axial velocity jump tends to zero at the area where the hub should be. It rises smoothly following the prescribed distribution as the relative radius ($r/R_P$) increases. After the peak is reached, the pressure jump decreases so that at the tip of the patch it falls to zero again. Accordingly, the axial and the mean flow velocity have the same value in that area. Observation of Figure 47b. shows the distribution of the tangential velocity over the actuator disc. Note that the function in Eq. (52). gives a non-physical solution for radii smaller than $R_H$. Because of that, the jump in tangential velocity is set to zero in that area. In the area of radii larger than $R_H$ the velocity is distributed as shown in Figure 45b.

In Figure 48 the wake behind the actuator disc is coloured with the axial velocity to inlet velocity ratio. The pressure jump distribution from Eq. (42). causes the variability of the axial velocity profile in the radial direction in an actuator disc wake.
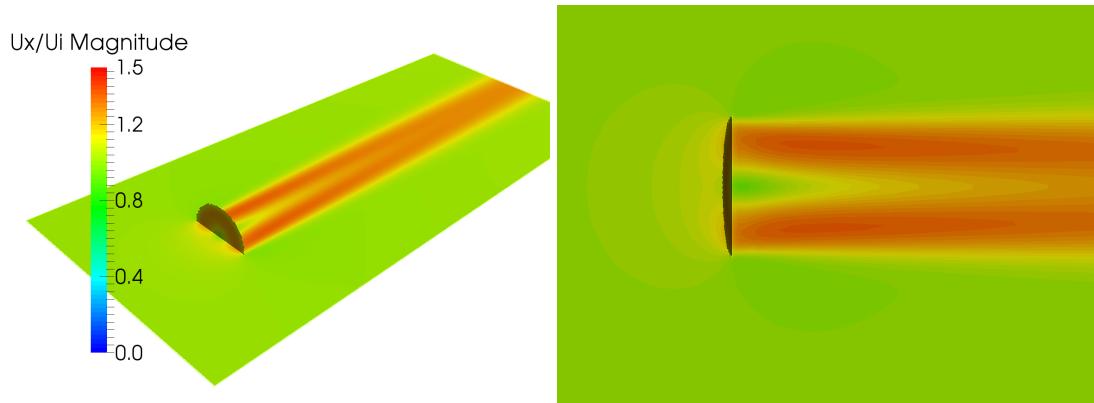
Figure 48: Axial velocity field in the actuator disc wake.

Figure 49 represents the velocity streamlines coloured with the axial velocity to inlet velocity ratio. The acceleration of the fluid in an actuator disc wake can be indicated by the transition from blue to red coloured streamlines. Besides that, the swirling motion of the fluid as a consequence of the applied velocity boundary condition can be seen.
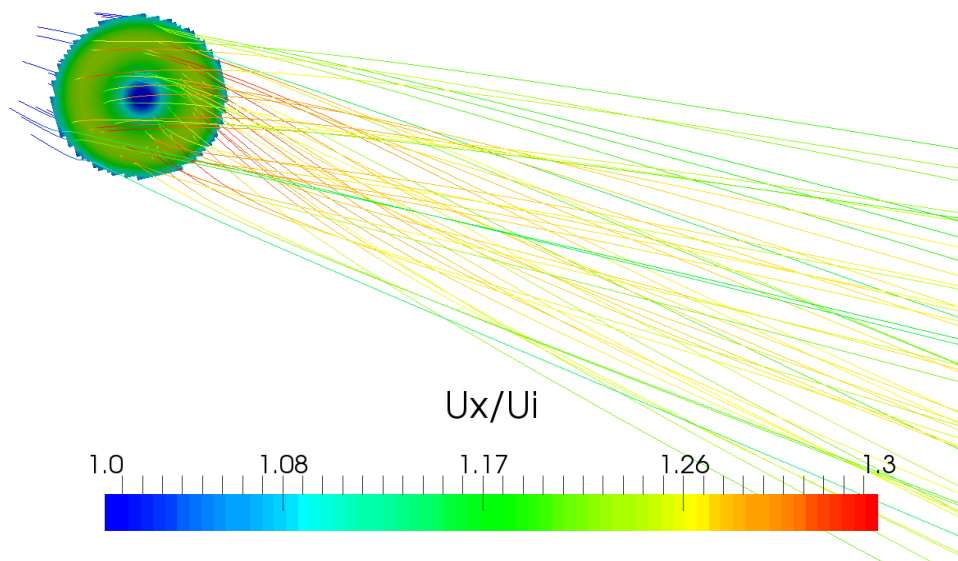


Figure 49: Streamlines behind an actuator disc.

## 5.3    Comparison with Results for the Resolved Propeller Geometry

It takes some time for stabilization of swirling flow so the simulation of three seconds of real time was performed. Regarding the Courant number, the much coarser numerical grid allows a larger time step to be used in this simulation. Unlike the actual propeller geometry simulation for which the time-step is limited to a value of $\approx 0.0003101 \ s$, in the actuator disc simulation

the time-step is set to $\Delta t_{ad} = 0.01\ s$, meaning that the simulation is run for 300 iterations. It is clear that the time scale of the simulation of fluid flow behind the propeller is increased by two orders of magnitude. The simulation was performed in 233 min, meaning that solution of one iteration lasts approximately 46.6 s in average.

The comparison of wake fields obtained with the MRF simulation of full propeller geometry and actuator disc is shown in Figures 50 and 51.
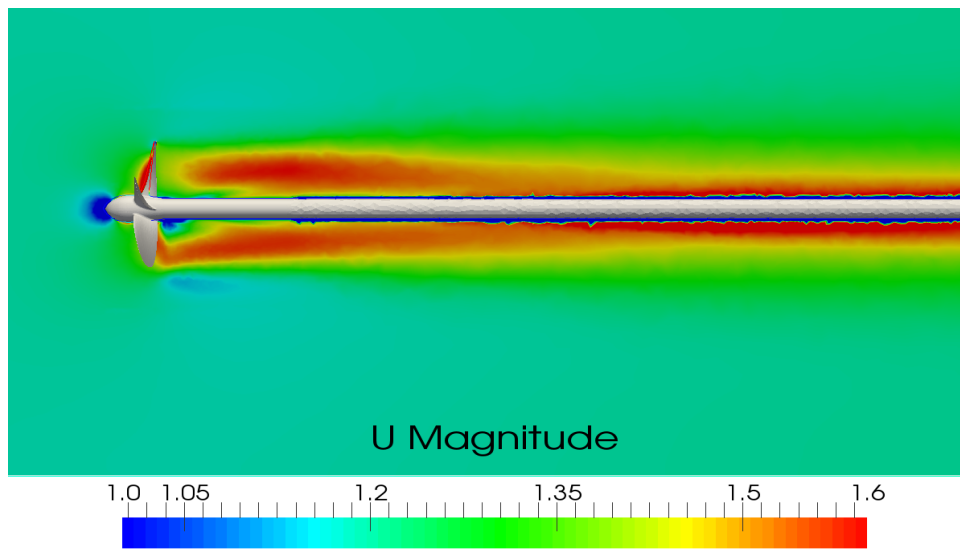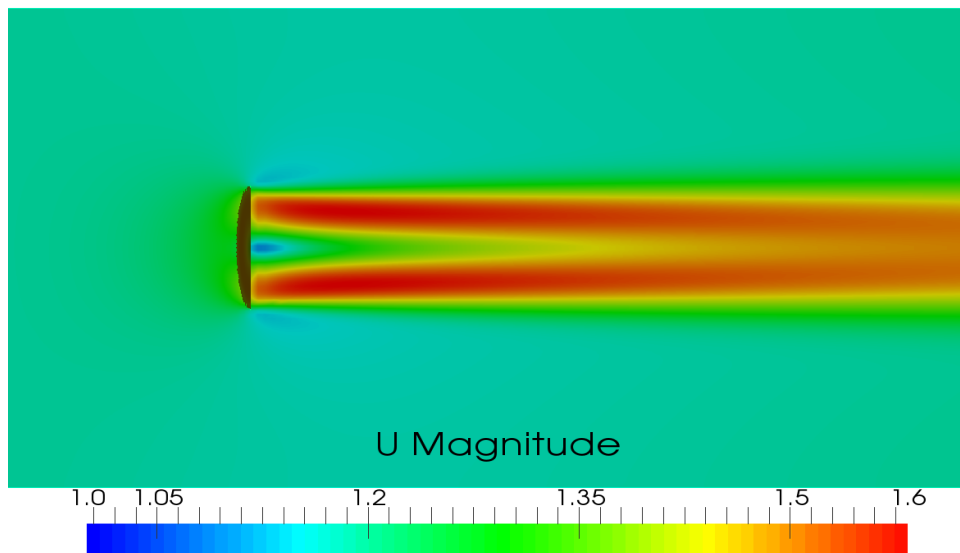


Figure 50: Propeller wake field.



Figure 51: Actuator disc wake field.

From Figures 50 and 51 the similarities between the wake fields are obvious. In the actuator disc simulation the flow is not influenced by the geometry so there is no additional disturbance as in the actual geometry simulation. Due to the lack of geometry in the actuator disc simulation

there is no point in evaluating the modelling based on the flow fields in the propeller plane. Moreover, the subject of observation is the wake behind the propeller so it is more relevant to compare the results of the simulations at the equally defined planes behind the propeller geometry or the actuator disc. The following flow fields results refer to a plane that is at a distance x $= 0.2R_P$ downstream the propeller or an actuator disc, where $R_P$ stands for the propeller radius. Figure 52 represents the pressure fields in the plane x $= 0.2R_P$.
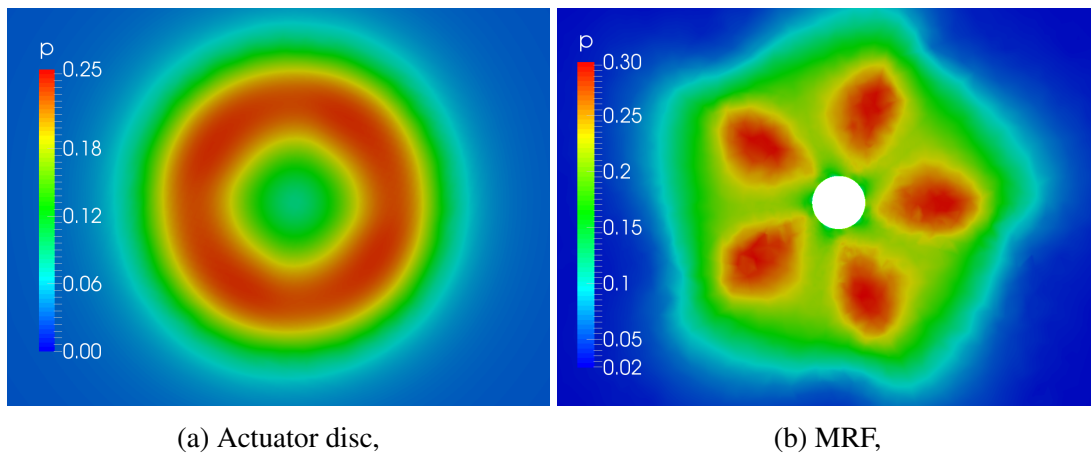


(a) Actuator disc,                                          (b) MRF,

Figure 52: The pressure field comparison in the plane x $= 0.2R_P$.



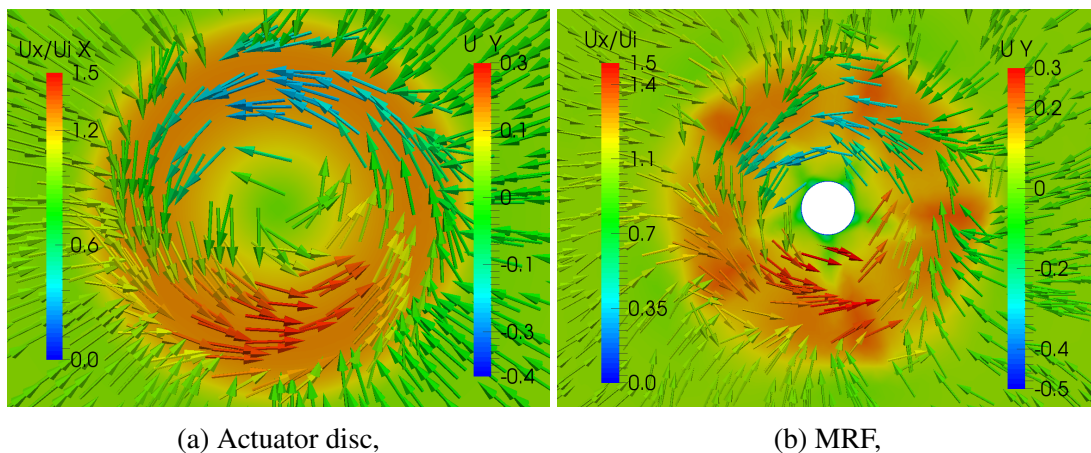(a) Actuator disc,                                          (b) MRF,

Figure 53: Velocity vectors projected on the plane x $= 0.2R_P$ coloured by $U_y$.

In Figure 53 the velocity vectors projected into the x $= 0.2R_P$ plane are shown. The plane is coloured with the axial velocity, while the projected vectors are coloured according to the magnitude of the y-component of the velocity. It can be seen that the distributions of the projected vectors with the similar magnitude correspond to each other in the MRF and the actuator disc simulation. In the actuator disc simulation projected vectors follow a uniform circular distribution, while in the MRF simulation the uniformity is disrupted because of the influence of the finite number of blades. The same applies to the vectors coloured by the

magnitude of the z-component of velocity shown in Figure 54. Figure 55 shows the tangential velocity comparison in the plane x $= 0.2R_P$.
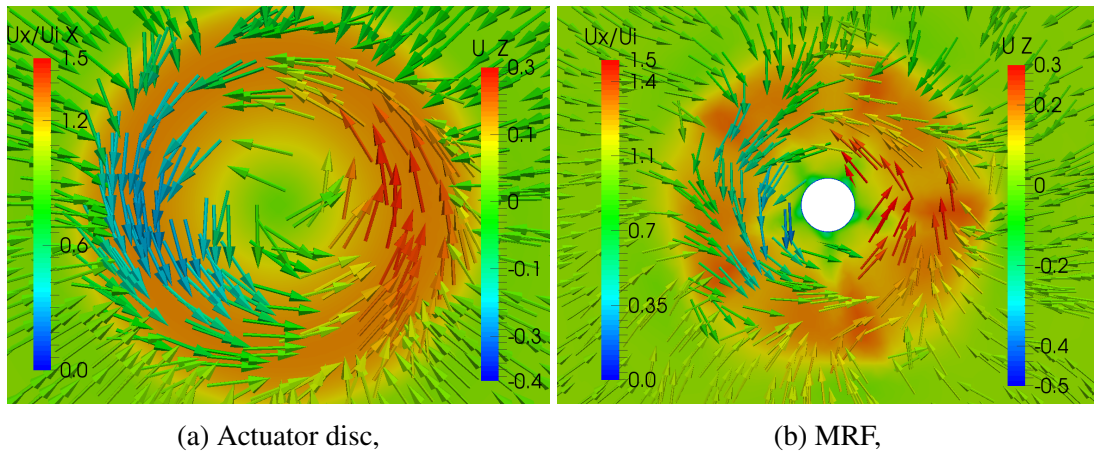


(a) Actuator disc,                                              (b) MRF,

Figure 54: Velocity vectors projected on the plane x $= 0.2R_P$ coloured by $U_z$.



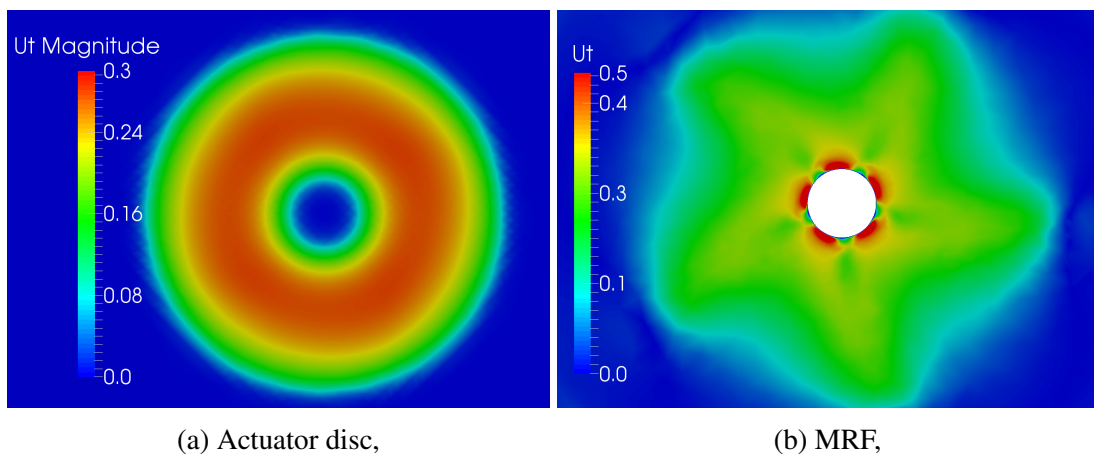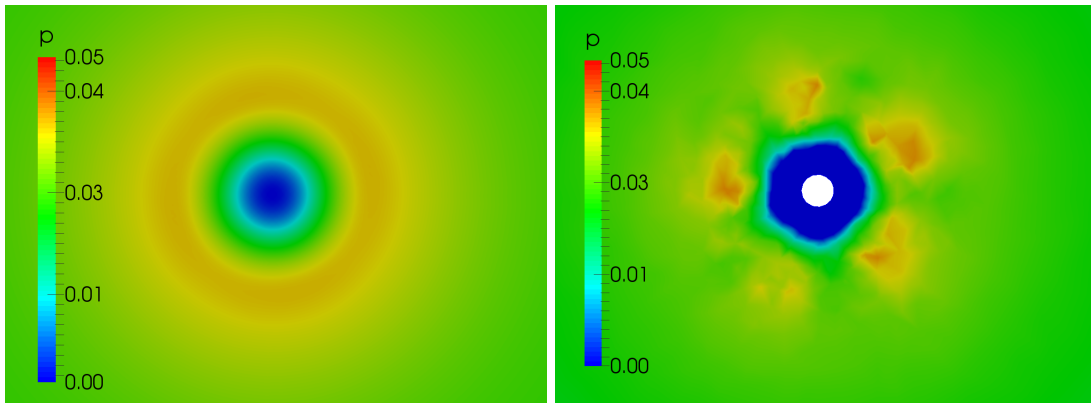(a) Actuator disc,                                              (b) MRF,

Figure 55: Tangential velocity comparison in the plane x $= 0.2R_P$.

To better evaluate the wake field obtained with the actuator disc simulation, a comparison of pressure and velocity fields is also made in the plane x $= 2R_p$. The comparison of pressure fields is given in Figure 56. Note that in the actuator disc simulation the pressure in the plane x $= 2R_p$ is uniform for a specific radius, which is not the case with the MRF simulation. Figures 57 and 58 show the projection of the velocity vectors on the same plane. Observation of the projected velocity vectors indicates that their distribution is more similar in the plane located further in the wake than in the plane right behind the actuator disc or propeller geometry (see Figures 53 and 54).

(a) Actuator disc,                          (b) MRF,

Figure 56: Pressure field comparison in the plane x $= 2R_P$.
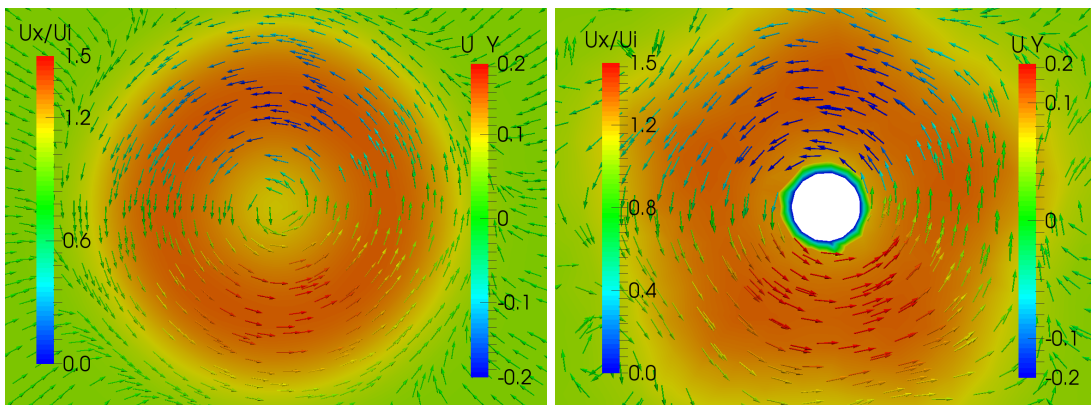


(a) Actuator disc,                          (b) MRF,

Figure 57: Velocity vectors projected on the plane x $= 2R_P$ coloured by $U_y$.

In Figures 57 and 58 the background is coloured with the axial velocity to the inlet velocity ratio. It can be seen that in comparison with Figure 53, the axial velocity has more a uniform distribution if observed on the specific radius. The tangential velocities in the x $= 2R_p$ plane obtained with the actuator disc and MRF simulation are given in Figure 59.
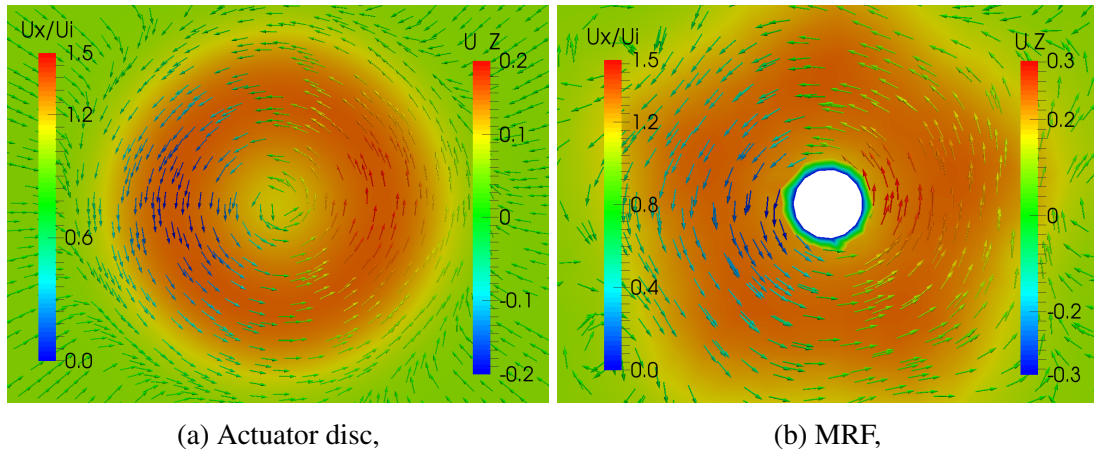
(a) Actuator disc, (b) MRF,

Figure 58: Velocity vectors projected on the plane x $= 2R_P$ coloured by $U_z$.



(a) Actuator disc, (b) MRF,
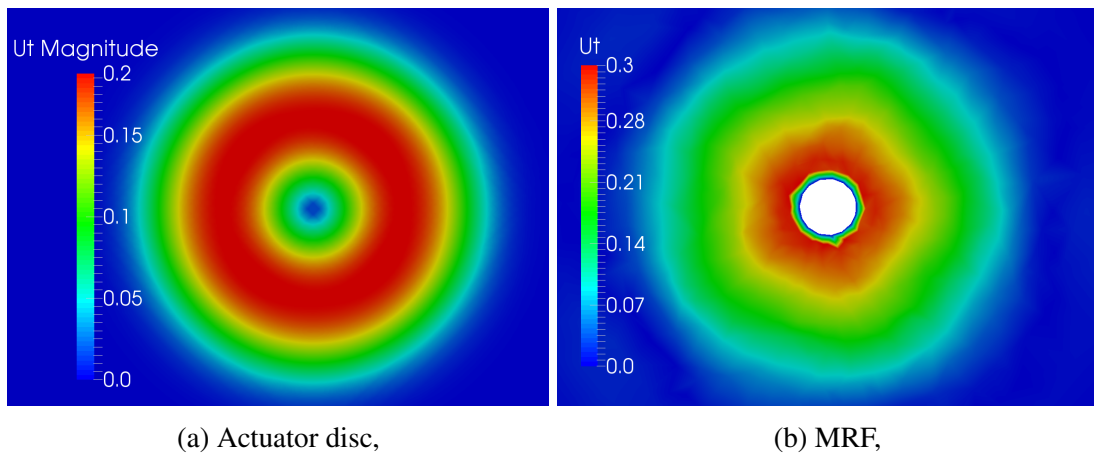
Figure 59: Tangential velocity comparison in the plane x $= 2R_P$.

A comparison of graphical representations of obtained flow fields shows that there is a consistency between the results of simulation with actual geometry and the simulation where the propeller effects on the flow were modelled.

To give a better insight into the differences between the results of the propeller simulation and propeller modelling it is beneficial to analyze the flow field velocity further. Its components (axial and tangential) can be compared at specific radii in the same plane for which the graphical results were given. In Figures 60 and 61 the comparison between the axial and tangential velocity is given for $R/R_p$=0.3 and $R/R_p$=0.5.
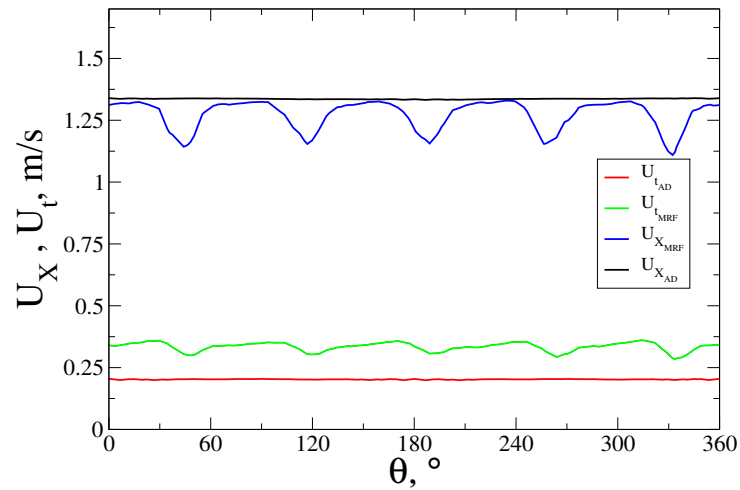
Figure 60: Velocity components in x $= 0.2R_P$ at $R/R_P = 0.3$.
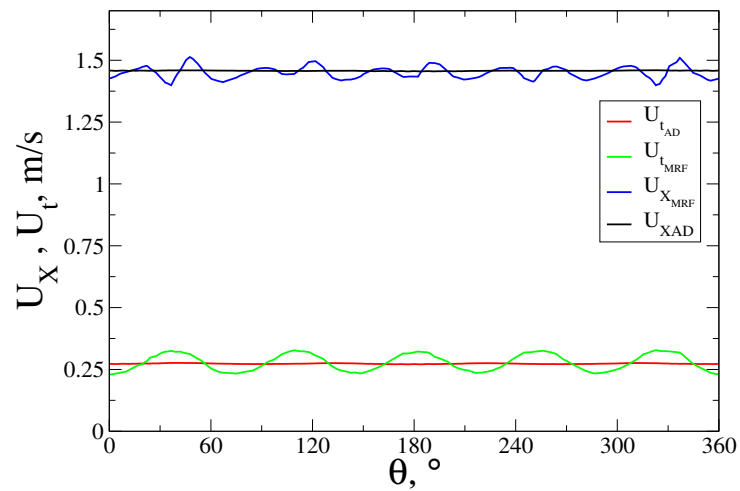


Figure 61: Velocity components in x $= 0.2R_P$ at $R/R_P = 0.5$.

The average values of axial and tangential components correspond well between the actual geometry simulation and actuator disc simulation. It is important to note that, due to the propeller blades, the velocity component curves obtained from the propeller simulation have positive and negative peaks that are periodically repeated five times. As the actuator disc is modelled as an infinite-bladed propeller, the velocity curves on a specific radius are constant, without obvious maximum and minimum values. Note in Figure 60 that for $R/R_P = 0.3$ the tangential velocity from an actuator disc simulation is slightly lower than the tangential velocity from the propeller simulation. It means that in the propeller simulation the fluid flow on this radius is still influenced by the viscous forces that are significant due to the vicinity of root of the propeller blades. In an actuator disc model, besides the boundary conditions there are no other influences on the mean flow. Therefore the velocity is only defined with the given distributions, which are defined for this radius with a lower value. For visualization of the values given in the diagram it is helpful to look at Figure 55b. If the average values of velocity

components are considered for $R/R_P = 0.5$, it can be said that the actuator disc simulation matches the actual geometry results relatively well. This applies to both the axial and the tangential component. In Figures 62 and 63 the distributions are given for $R/R_P = 0.7$ and $R/R_P = 0.9$.
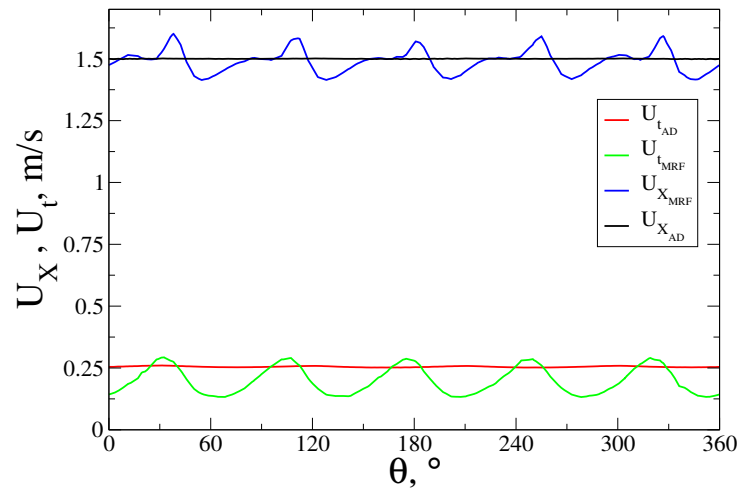


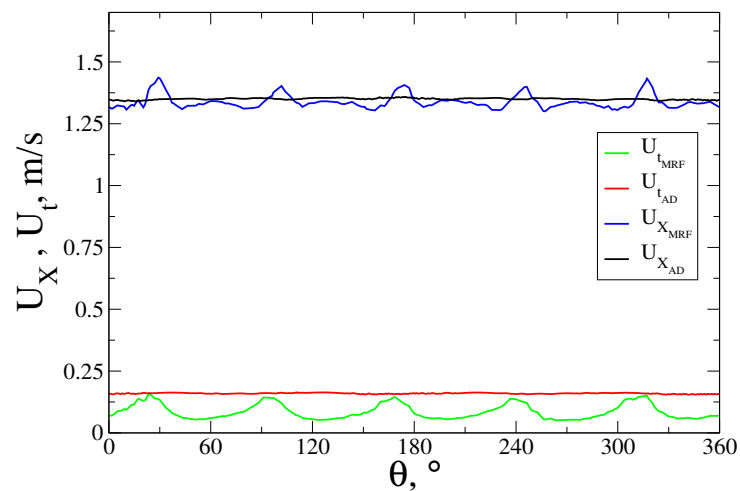Figure 62: Velocity components in x $= 0.2R_P$ at $R/R_P = 0.7$.



Figure 63: Velocity components in x $= 0.2R_P$ at $R/R_P = 0.9$.

Regarding the velocity components on $R/R_P = 0.7$ the same can be stated as for $R/R_P = 0.5$. The mean values of the axial and tangential velocity from an actuator disc simulation correspond well to the mean values of propeller simulation velocities. For $R/R_P = 0.9$ the tangential velocity obtained from actuator disc simulation is slightly higher, while the axial velocities are well matching.

The results analysis on plane x $= 0.2R_P$ shows that the theoretical distribution provides accurate results for the axial velocity. It indicates that for this specific propeller the thrust can be sufficiently modelled using the Goldstein optimum distribution to define the pressure

jump on an actuator disc. The diagrams of the tangential velocity, in the other hand, show the greatest deviation at the smallest radius. In propeller simulation that area is influenced by the boundary layer, which is not present in an actuator disc simulation. For the greatest radius in consideration, there is also a gap between the calculated tangential velocity values. In the other two cases ($R/R_P = 0.5$ and $R/R_P = 0.7$) the mean values of tangential velocity obtained from an actuator disc model and actual propeller simulation correspond relatively well.

To give a better insight into differences between the flow influenced by the actuator disk and the actual geometry the diagrams with velocity components in function of normalized radius ($R/R_P$) are shown in Figures 64 and 65. The diagrams refer to velocity components on the x $= 0.2R_P$ plane. It can be seen that velocity curves corresponding to actuator disc simulation follow the prescribed theoretical distribution as shown in Figure 45a and 45b. Due to the finite number of blades the flow field values behind the propeller geometry do not follow uniform distribution (see Figure 55). Depending on the position of the blades the areas with the higher and lower velocity values alternate in the propeller wake. Therefore, the values of flow fields in function of normalized radius depend largely on the location at which they are collected. In this case the velocity components are plotted over two lines that connect the centre of the x $= 0.2R_P$ plane and two different points of the plane on the radius $R_P$. The average values of velocity components are calculated between the points of the specified lines that are located on the same normalized radius.
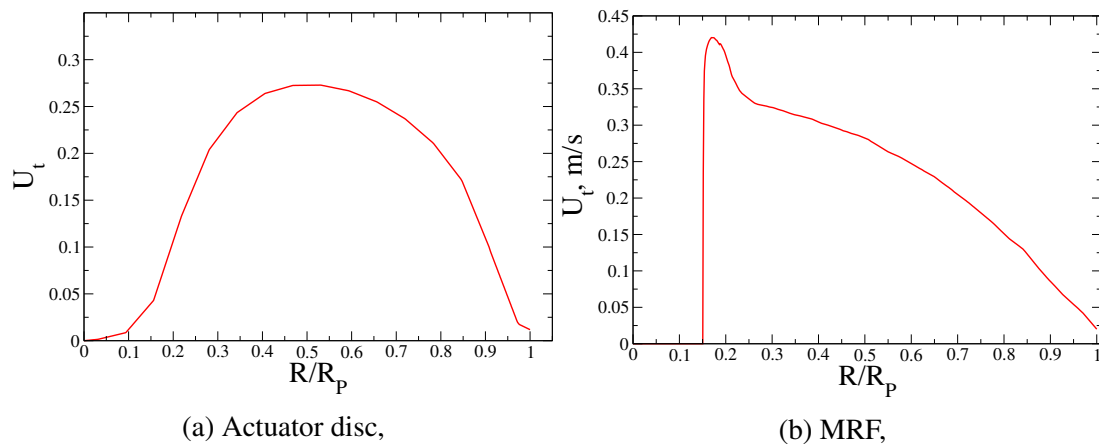


(a) Actuator disc,                                    (b) MRF,

Figure 64: Tangential velocity distributions in function of normalized radius on x $= 0.2R_P$ plane.

(a) Actuator disc,          (b) MRF,
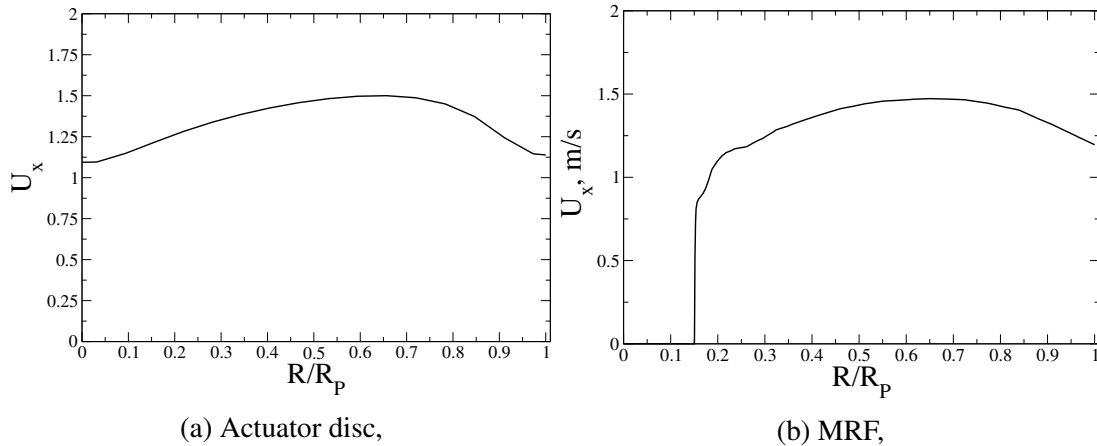
Figure 65: Axial velocity distributions in function of normalized radius on x $= 0.2R_P$ plane.

In the propeller simulation diagram, the area where the velocity is zero can be noticed. This is the area where the propeller shaft is placed so there is no fluid in that region ($R < R_H$). The remarkable difference between the results of the actuator disc and propeller simulation is that in the actuator disc simulation the fluid motion is present in the that area. The other eye-catching difference is a peak in the diagram in Figure 64b. Such a notable peak is a consequence of taking into account only two positions on the plane behind the propeller when calculating an averaged velocity distribution. In order to get a more reliable comparison with the actuator disc results, the circumferential average of velocity components values behind the propeller needs to be taken into account. By calculating a circumferential average the peak of the diagram is assumed to diminish. In that way the velocity components distribution over the normalized radius is assumed to get closer to the theoretical distribution.

To get more information about the actuator disc impact on the flow, the velocity components obtained from the actuator disc and complete propeller simulation are compared on a plane located further in the wake field. In Figures 66 and 67 the axial and tangential velocity components comparison in plane x $= 2R_P$ is given. The velocities are analyzed on the same radii as in plane x $= 0.2R_P$. It can be noticed that the velocity components have a more similar value when observed at a further distance in the wake where the influence of the propeller blades is weakened.
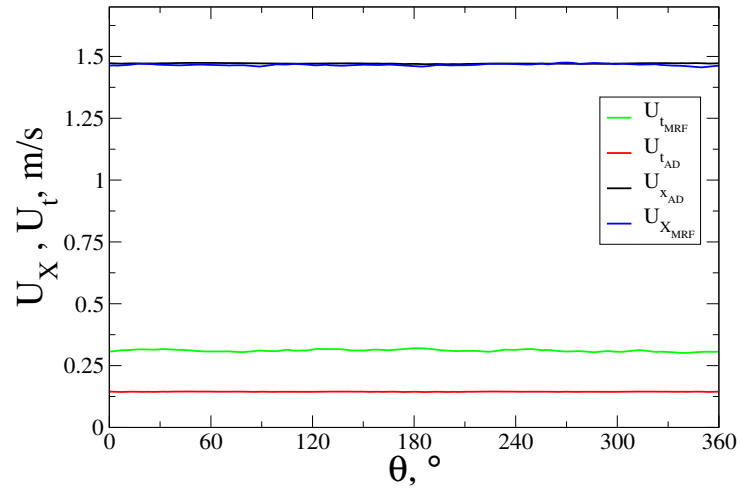
Figure 66: Velocity components in x $= 2R_P$ at $R/R_P = 0.3$.
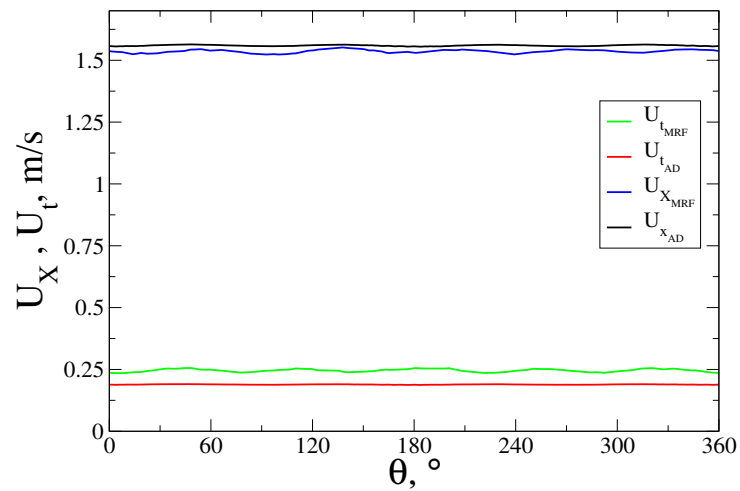


Figure 67: Velocity components in x $= 2R_P$ at $R/R_P = 0.5$.

The only significant difference between the velocity values further in the wake relates to the tangential component on the smallest radius considered ($R/R_P = 0.3$). The tangential velocity obtained from the propeller simulation is in that case slightly greater than the tangential velocity from the actuator disc model. The comparison between the velocity components is also given at $R/R_P = 0.7$ and $R/R_P = 0.9$. Observation of Figures 68 and 69 indicates that axial and tangential velocities at the larger radii are well modelled using the theoretical distributions from Eq. (42). and Eq. (52).
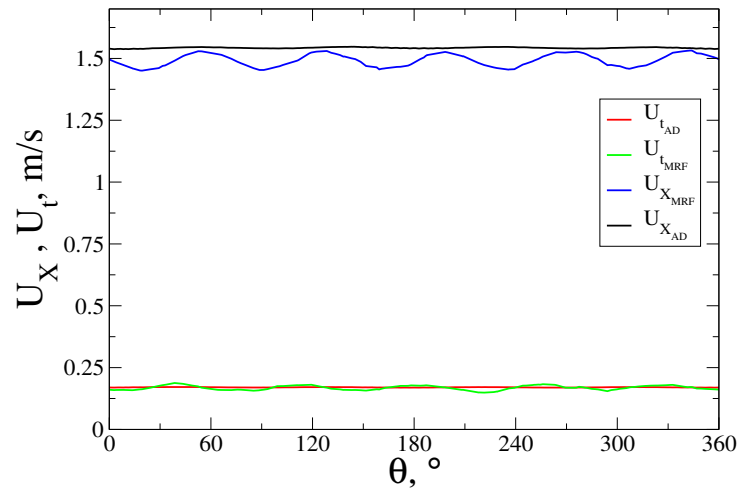
Figure 68: Velocity components in x $= 2R_P$ at $R/R_P = 0.7$.
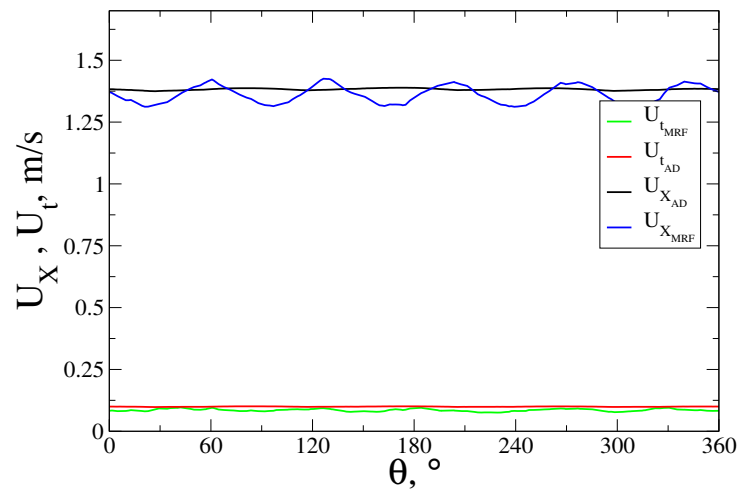


Figure 69: Velocity components in x $= 2R_P$ at $R/R_P = 0.9$.

Although the fluctuations of the velocity values are present in the results of the MRF simulation of propeller geometry (Figures 68 and 69), the average values of velocity components are almost identical.

The velocity fields in the wake of propeller and actuator disc are examined further by following the same pattern as explained for plane x $= 0.2R_P$, where the observation is made in regard to the normalized radius. The distributions of velocity components in function of the normalized radius are given in Figures 70 and 71. As explained previously the area with the greatest difference in velocity is the area in which the shaft is present in the propeller simulation. Although there is a significant difference between the trends of the curves obtained from an actuator disc and a propeller simulation for smaller radii, the values on the greater radii are well approximated using the Goldstein distribution. It can be noticed that the peak of the tangential velocity curve obtained from the propeller simulation is not as sharp as that in the plane closer to the geometry.
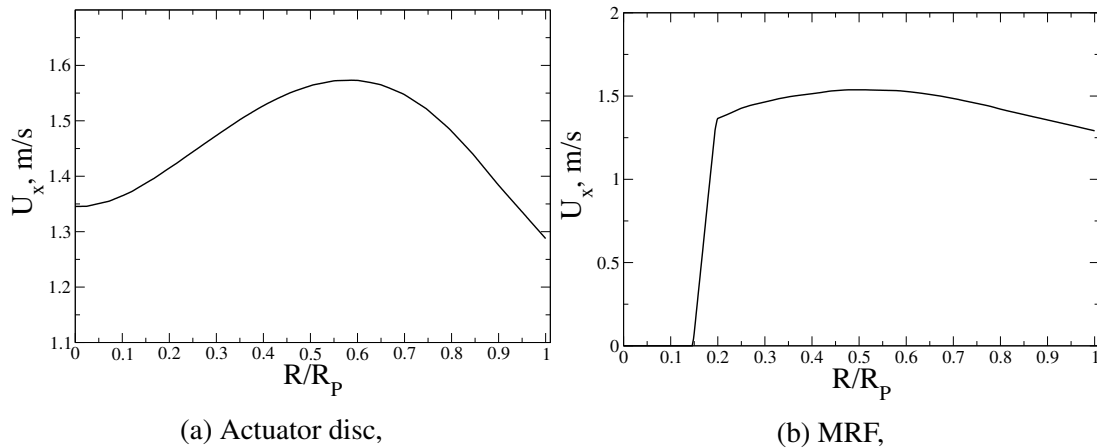
(a) Actuator disc,        (b) MRF,

Figure 70: Axial velocity distributions in function of normalized radius on x $= 2R_P$ plane.
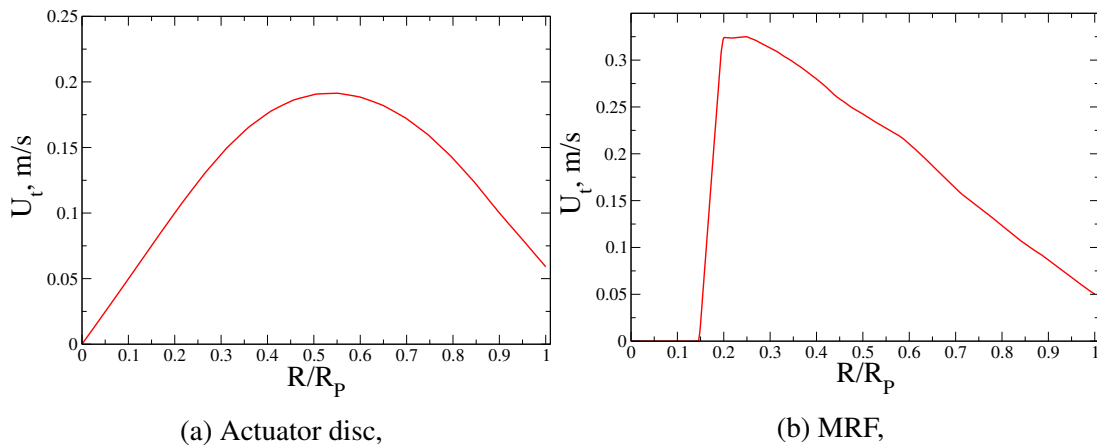


(a) Actuator disc,        (b) MRF,

Figure 71: Tangential velocity distributions in function of normalized radius on x $= 2R_P$ plane.

It can be stated that performing the simulation using the described functions definitely gives an acceptable wake field. The problem is that, due to the theoretical forces distribution, the wake is slightly different from the one in the CFD simulation of the propeller geometry. Since performing an actuator disc simulation is in fact a step towards the self-propulsion test simulation, it is important to account for the real distributions of field values, so the propeller-hull interaction can be determined correctly. To get closer to the actual wake, it would be beneficial to map the distribution of pressure and velocity from the actual propeller simulation and to implement it in form of boundary conditions. There is also a possibility to use a numerical grid where the shaft is included. In that way low computational time could be maintained, while the wake solution from the propeller simulation could be better approximated using the actuator disc model.

## 5.4   Closure

In this section the actuator disc model is presented. The theory behind the model is explained and substantiated with the derivation of formulas used to define the boundary conditions on the actuator disc. The actuator disc model is evaluated against the actual propeller simulation results. The comparison is made in form of graphical representations of flow fields, as well as diagrams showing the velocity distributions that describe the wake motion. Overall, the results from the simplified actuator disc model are considered to give an acceptable approximation of the full propeller model.

# 6   Conclusion

This thesis covers the process of CFD simulation of the open water test for a ship propeller. Three different approaches were applied, the results of which are compared with experimental data in order to evaluate their accuracy. The one blade passage of the propeller blade is simulated using the numerical grid with periodic boundaries, while the MRF and transient simulations are performed using the complete propeller mesh. The approaches based on the steady-state approximation provided slightly less accurate (but acceptable) results in comparison to the fully transient simulation. However, at the same time the utilization of CPU resources is notably reduced. The open water diagrams obtained from the steady state simulations show a more consistent error for the complete propeller than for the one blade passage mesh.

If the open water characteristics are known in advance, the propeller can be modelled in a self propulsion simulation with a simplified actuator disc in order to reduce the CPU requirements. In the course of this thesis the actuator disc model is applied using the previously obtained solution of complete propeller simulation in the MRF approach. The model is based on the pressure and velocity boundary conditions applied on the internal boundary presenting the disc. The pressure boundary condition defines the pressure jump distribution in order to produce the desired acceleration of the fluid in the axial direction, while the velocity boundary condition defines the distribution of tangential velocity jump causing the swirling motion. The distributions are prescribed using the theoretical Goldstein optimum. The simulation is performed using a fully structured numerical grid which is much coarser than the one used in the full propeller geometry simulation. In order to evaluate the of accuracy of the actuator disc model the wake fields obtained from the two modelling approaches are compared. The comparison of velocity components obtained with the actuator disc and full propeller geometry simulation is performed on two planes located at different distances. The axial velocity is well matched on both planes, which indicates that the theoretical distribution of pressure jump can be used for this purpose. The tangential velocity showed good agreement on average, however details of the wake are not captured. The comparison of the tangential velocities from the actuator disc simulation and propeller geometry simulation in the closer plane showed the deviation at the smallest and the largest radius considered, while for the area in between the results are acceptable. The differences on smaller radii are expected since the shaft is included in the full propeller geometry simulations. It can be stated that, considering the theoretical distributions being used for the pressure and velocity jump over the disc, the solution of the wake field is acceptable. Further work should be based on improving the model so that the swirl behind the propeller could be better matched. Since the greatest deviation is related to the tangential velocity examined on

the smallest radius, it would be interesting to perform the actuator disc simulation using the numerical grid with the shaft included. It is assumed that by using such a grid the differences between the actuator disc and the propeller geometry simulation in that area will be reduced.

The biggest obstacle in performing the self-propulsion test simulation are extremely high computational costs due to the large difference between the time-scales of the hull and propeller flow. Considering the acceptable wake field obtained with the actuator disc model and the savings in terms of CPU time, the model proves to be an attractive alternative to the fully resolved propeller simulation.

Due to the simulation start unsteadiness the transient simulations of periodic flows (e.g. flow around the propeller) have to be run for a number of periods in order to obtain the periodic steady state which increases the CPU time. The harmonic balance method introduced by Cvijetić [20] showed a good agreement with the conventional transient simulations, while reducing the simulation time. Using this method to simulate the flow around the propeller geometry should be considered, since it may provide even better solution accuracy than the methods used in this thesis.

# References

[1] "A Workshop on CFD in Ship Hydrodynamics," `http://www.t2015.nmri.go.jp/`, last access 17.3.2017.

[2] "foam-extend project," `https://sourceforge.net/projects/foam-extend/`, last access 24.2.2017.

[3] Beaudoin, M. and Jasak, H., *Development of a Generalized Grid Interface for Turbomachinery simulations with OpenFOAM*, Open Source CFD International Conference, Berlin, Germany, 2008.

[4] Jasak, H., *Numeričke metode u mehanici kontinuuma (Numerical Methods in Continuum Mechanics)*, Material for lectures, SIAM, 2006.

[5] Vukčević, V., *Application of computational fluid dynamics in the motion analysis of ships and offshore platforms*, Master's Thesis, Faculty of Mechanical Engineering and Naval Architecture, University of Zagreb, 2013.

[6] Wilcox, D., *Turbulence Modeling for CFD*, DCW Industries, Inc., California, 1993.

[7] Menter, F., *Two-equation eddy-viscosity turbulence models for engineering applications*, AIAA Journal, Vol 32., pp.1598-1605, 1993.

[8] "CFD Online," `https://www.cfd-online.com/`, last access 11.2.2017.

[9] Cvijetić, G., *Steady State Methods for Turbomachinery*, Zagreb, 2014.

[10] "See the MRF development," `http://openfoamwiki.net/index.php/See_the_MRF_development`, 2009., last access 11.2.2017.

[11] Carlton, J., *Marine Propellers and Propulsion (Third Edition)*, Elsevier Ltd., 2012.

[12] "Pointwise Release Notes," `http://www.pointwise.com/support/release-notes-V18R1.shtml`, last access 13.3.2017.

[13] Saad, Y., *Iterative Methods for Sparse Linear Systems (2nd Edition)*, Society for Industrial and Applied Mathematics Philadelphia, SIAM, 2003.

[14] Ahrens, James, Gaveci, Berk, Law, and Charles, *ParaView: An End-User Tool for Large Data Visualization*, Visualization Handbook, Elsevier, ISBN-13:978-0123875822, 2005.

[15] Kolář, V., *Vortex identification: New requirements and limitations*, International Journal of Heat and Fluid Flow, Vol. 28, pp. 638-652, 2007.

[16] Holzmann, T., *Mathematics, Numerics, Derivations and OpenFOAM(R)*, Holzmann CFD, Leoben, fourth edition, 2016.

[17] Krasilnikov, V. I., *Self-Propulsion RANS Computations with a Single-Screw Container Ship*, Third International Symposium on Marine Propulsors SMP'13, Launceston, Australia, 2013.

[18] Svenning, E., *Implementation of an actuator disk in OpenFOAM*, Chalmers University of Technology, 2010.

[19] Goldstein, S., *On the Vortex Theory of Screw Propellers*, Proceedings of the Royal Society of London. Series A, Containing Papers of a Mathematical and Physical Character, Volume 123, Issue 792, pp. 440-465.

[20] Cvijetić, G. and Gatin, I., *Applications of Harmonic Balance Method in Periodic Flows*, Student Submission for the 4th OpenFOAM User Conference, Cologne-Germany, 2016.